DEGREE PROJECT IN CHEMICAL SCIENCE AND ENGINEERING,
SECOND CYCLE, 30 CREDITS
STOCKHOLM, SWEDEN, 2017

Development of U_3Si_2 pellets for LWR applications

Synthesis, characterization and degradation performance

Anna Benarosch

Supervisor:
Dr. Denise Adorno Lopes

Head of Reactor Physics:
Dr. Pär Olsson

Examiner:
Pr. Mats Jonsson

”Nothing in life is to be feared, it is only to be understood.
Now is the time to understand more, so that we may fear less.”

Marie Curie

ABSTRACT

After the Fukushima Daichii nuclear accidents, the use of UO_2 as a fuel and zircaloy as cladding material has been challenged. U_3Si_2, combined to SiC or a FeCrAl steel for cladding, has been studied as a possible candidate to replace the current system used in Light Water Reactors (LWR).

However, difficulties have been encountered to produce pellets suitable for LWR applications with low sintering temperatures, low sintering times and without the use of additives which favour the formation of open pores. In addition to this, little data is available on how the U_3Si_2 matrix will accommodate to the fission product production during irradiation. In literature, only data resulting from liquid-liquid interactions are available, while in an irradiated fuel, solid-solid interactions are expected. To be approved as a fuel, U_3Si_2 needs to show an increased oxidation resistance in case of accident compared to UO_2, which has been only partially covered in literature. Finally, the question of how to handle the spent fuel in the back-end still needs to be answered. If it is to be stored in a geological repository like UO_2, the resistance of U_3Si_2 to dissolution in case it is in contact with groundwater is a crucial data to get.

In this work, the production of highly dense pellets (>96%TD), suitable for LWR applications, is described. The alloys were first produced by arc melting, milled into powder and sintered by Spark Plasma Sintering (SPS). It produced pellets without U_3Si and with a unique microstructure made with nano-metric closed pores. This unexpected microstructure could be explained by the heterogeneous particles size distribution, or could be explained as being a feature of the material itself.

A fission product production due to burn-up was experimentally simulated by sintering milled molybdenum with milled U_3Si_2 by SPS. It showed the absence of solubility of molybdenum in the matrix, as well as the formation of two U-Si-Mo ternary phases, $U_2Mo_3Si_4$ and $U_4Mo(Mo_xSi_{1-x})Si_2$, and some γ(U,Mo) inclusions. This methodology permitted the study of the phases resulting from the solid-solid interaction and showed which phases formed at the initial stages.

The oxidation resistance in air of U_3Si_2 was studied by running TG and DSC at 1000°C to collect data on the mass increase and on the mass enthalpy. It showed a reaction twelve times more exothermic than the oxidation of UO_2. The formation of U_3O_8 was demonstrated by XRD and the formation of an oxide of silicon could be identified by FTIR. The results showed that silicon most likely does not completely oxidize, meaning that its oxidation may be more difficult than the oxidation of uranium.

The oxidation resistance of U_3Si_2 in presence of hydrogen peroxide, in an inert atmosphere, was evaluated to both understand the dissolution in case the fuel is in contact with the reactor coolant in accident conditions and in case the fuel is in contact with the groundwater. It proved to have a lower yield than similar dissolution with UO_2, meaning that more hydrogen peroxide is required to dissolve the same amount of uranium. It can be explained by the fact that uranium most probably has a lower oxidation state in U_3Si_2 than in UO_2, and as well because most likely both uranium and silicon get oxidized. An unexpected consumption of dissolved uranium could be put in evidence, probably the result of a reaction of the dissolved uranium with U_3Si_2. U_3Si_2 was exposed as well to gamma radiation and the dissolution of uranium was followed, to use closer conditions to the ones expected in a reactor or in a geological storage. The dissolution showed a higher yield than for the experiments realized with hydrogen peroxide, probably meaning that the species dissolved here have a lower oxidation state than the ones dissolved in the previous experiments and that the catalytic decomposition of hydrogen peroxide is reduced.

ACKNOWLEDGEMENTS

First, I wish to acknowledge Dr. Claire Kerboul, Cabinet Director of CEA, and Mr Claes Thegerström, former CEO of SKB, who helped me to find the right place to do my master thesis about nuclear fuels. Without their help, I would not have been able to get in contact with Pr. Waclaw Gudowski, Professor in the Reactor Physics Department, nor with Dr. Pär Olsson, Head of Reactor Physics.

I thank Pr. Waclaw Gudowski for introducing me to the Department and for checking from time to time that everything was going on well.

I would like to express my deepest gratitude to Dr. Pär Olsson for welcoming me in his team and for giving me the chance to research on such an exciting topic.

I am also grateful to Pr. Mats Jonsson, Vice Dean of the School of Chemical Science and Engineering, who I collaborated with for this project. He helped me with the dissolution experiments of this project and his advice and ideas were essential.

I would also like to warmly thank Annika Maier and Ghada El Jamal, both PhD students in Pr. Mats Jonsson's laboratory, who were my partners and guides in the lab during the dissolution experiments. It has been a pleasure working with them.

This project would not have been possible either without the help and the precious guidance of Dr. Kyle Johnson who was as much as a second supervisor to me. He has been present for a great part of this project, helping with his expertise and helping to reflect on the results.

I would like to particularly thank Dr. Denise Adorno Lopes, my supervisor, who has been present at every step of this project. I have learned and discovered a lot by her side. We shared a lot of exciting and joyful moments. This project would not be what it is today without her precious guidance.

Finally, I would like to thank Westinghouse for financial support, as well as Dr. Simon Middleburgh, Senior Engineer at Westinghouse, who has been following the course of this project from the beginning to the end.

TABLE OF CONTENTS

LIST OF FIGURES

LIST OF TABLES

1. INTRODUCTION

In Light Water Reactors (LWR), the fuel is designed in UO_2 pellets contained in a Zircaloy cladding, and the entire system is cooled by light water. After the Fukushima Daiichi nuclear accidents in 2011, the use of such a system was questioned. During the accident, the rapid and highly exothermic oxidation of the Zircaloy cladding led to the production of H_2, responsible for explosions, and the large heat production enhanced the degradation of the core[1]. New cladding and fuel combinations are being developed for greater resistance towards accident conditions.

Some of the characteristics of an accident tolerant fuel, as defined by the IAEA are[2]:

- High melting temperature;
- Improved oxidation resistance with high-temperature steam;
- Increased thermal conductivity of the fuel;
- Enhanced retention of fission products.

A more accident tolerant fuel goes along with an enhanced accident tolerant cladding, which together must exhibit good chemical and mechanical compatibility. Various cladding solutions have been considered, such as a cladding made with SiC fiber/SiC matrix ceramic matrix composite[3], among others. For electricity production, increasing the U loading in a more accident tolerant fuel, while respecting the enrichment limit, presents an economic advantage due to the potential for longer residence times in core and higher burn-up. Westinghouse calculations indicate that the replacement of the current Zr/UO_2 fuel system with a SiC ceramic matrix composite cladding and high-density fuel would result in up to 8.8% fuel cycle cost savings[3].

2. LITERATURE REVIEW

2.1 U-Si

The National Reduced Enrichment Research and Test Reactor Program (RETR), created in 1979, aimed at reducing the ^{235}U enrichment from above 90% to below 20%, in order to lessen the risk of diversion for nonpeaceful activities[4]. Uranium silicides have been studied due to their higher fuel loading compared to UAl_x or U_3O_8, used at the time[5]. First used in research reactors, they are now being considered for adaptation to Light Water Reactors. Silicon has the advantage of being one of the most abundant elements on earth, being the second most abundant element in the Earth crust, after oxygen.[6]

2.2 U_3Si_2

To understand why U_3Si_2 was chosen, it is important to have a look at the phase diagram presented in Figure 1 [7].

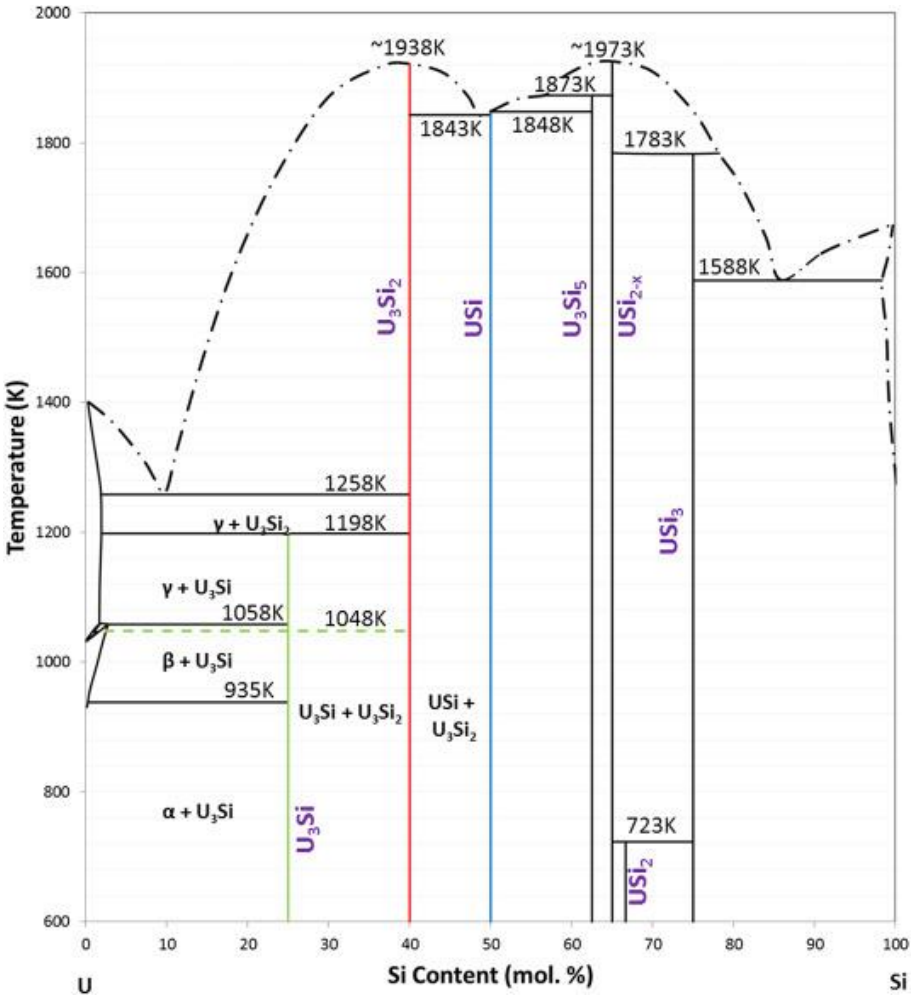

Figure 1: Phase diagram of U-Si

According to the phase diagram visible in Figure 1, U_3Si is the most U-enriched U-Si phase. However, the material has demonstrated poor behaviour under irradiation while U_3Si_2 seems more promising[8].

Table 1 shows a comparison of the characteristics of U_3Si_2 and UO_2. U_3Si_2 has a 17% higher U-loading than UO_2, which means that there are 17% more uranium atoms per cm^3 in U_3Si_2 than there are in UO_2. This enables either less enrichment or longer cycles, which are both economically beneficial[8]. U_3Si_2 melts at a temperature about 1000°C lower than UO_2, but it is off-set by a higher thermal conductivity and, of special importance for accident scenarios, a thermal conductivity which increases with temperature. This enables the centreline temperature in a fuel pin to be drastically dropped compared to UO_2 fuel pins. For example, for a peak linear power of 49.9 kW/m, the maximum fuel centreline of UO_2 is 2058°C, against 1066°C for U_3Si_2 [9]. This gives the fuel a greater ability to reject heat in the case of fuel overheating under accident conditions. However, U_3Si_2 swelling makes it worse than UO_2 in case of clad design stress and strain, or clad fatigue[9].

Table 1: Characteristics of U_3Si_2 and UO_2[8]

Compound	**UO_2**	**U_3Si_2**
Melting Temperature (°C)	2847	1665
Thermal conductivity (W/mK) 400-1200°C	2.5-6	21-38
Theoretical uranium number density ($atom/cm^3$)	2.44×10^{22}	2.86×10^{22}
Theoretical density (g/cm^3)	10.96	12.2

Modern LWR UO_2 fuel pellets are made to 95-97%TD, with a diameter that can range from 8.1mm to 10.6mm, depending on whether it is made for a BWR or a PWR[10]. In this respect, a fully dense pellet is not interesting for reactor applications. As the fuel is irradiated, fission products are produced, of which some, such as Xenon, Krypton, among others, are gaseous. These fission gases tend to diffuse and to agglomerate in pores, hence the preference to retain some residual pellet porosity. The pore distribution and structure in the as-fabricated conditions should be homogenous, with the ideal mono-modal pore size between 1 and 10 µm. Larger grain sizes are preferred, as they are thought to have a positive impact on the in-reactor behaviour, through improved fission gas retention[11].

With burn-up however, the fuel does not retain its original structure. The thermal stresses induced by temperature gradients cause macroscopic cracking, while microstructural defects are created by radiation damage. The chemistry of the fuel is changed as well with the production of the fission products, as well as with the absorption of neutrons in uranium nuclei, leading to the formation of transuranium elements[12].

Over operation, the fuel undergoes grain subdivision and extended defects appear. For spent UO_2 pellets, the formation of a "rim zone", different from the core of the pellet, can be observed, close to the pellet surface (see Figure 2)[13]. It is characterized by fine recrystallised grain size, an

increase in porosity compared to the rest of the pellet, and depletion of fission gas from the UO_2 matrix[14].

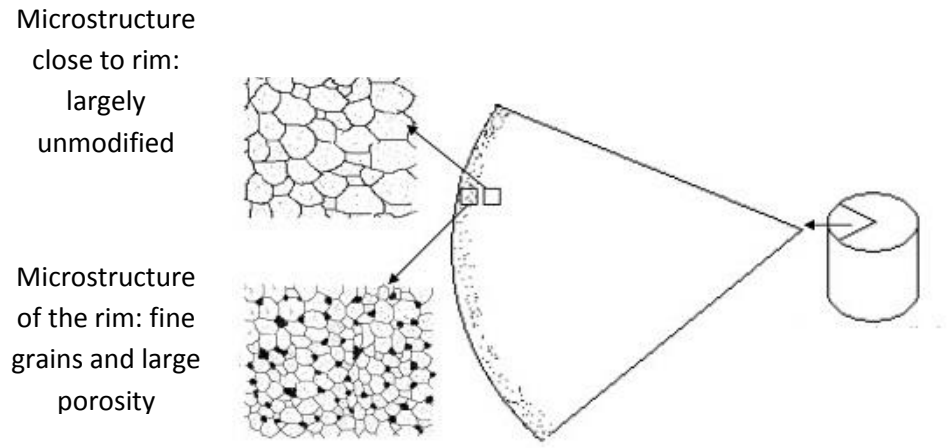

Figure 2: Schematics of a UO_2 pellet after irradiation and illustration of the rim zone

2.3 FABRICATION OF U_3Si_2 THROUGH CONVENTIONAL SINTERING ROUTE

U_3Si_2 has already been produced in pellets through a metallurgy route, as reported by Nelson *et al*[15]. They produced high-density pellets, superior to 96%. They arc melted depleted uranium metal with an excess of silicon to account for the volatilization in the molten state. The alloy was arc melted multiple times to maximize homogenization. It was then heated for a very long time to form an homogenized solid solution: at 80% of the melting temperature of U_3Si_2 (around 1500°C), for 50 to 80 hours in gettered argon atmosphere ($P_{O2}<10^{-16}$ atm). The alloy was then milled into powder and pressed into a pellet shape. The sintering was done in gettered argon atmosphere and required 24 to 48 hour isothermal holds at temperatures similar to those employed in the heat treatment steps. The pellet proved to be substantially free of second phases.

Idaho National Laboratory also produced U_3Si_2 pellets by conventional powder metallurgy route[8]. The bulk uranium was first hydrided/dehydrided, i.e. transformed to UH_3 and then reduced, in an inert atmosphere. The stress induced in the change in lattice parameter broke the metal into a fine powder. The uranium was mixed with hammer-milled silicon powder and compressed at 225MPa, agglomerated by quickly heating up to 1450°C, held for 30min. The raw material was then arc melted. The silicon was added in a slight excess to prevent the formation of U_3Si or U-solid solution phases. The excess of silicon also accounts for observed silicon loss during the arc melting. After arc melting, the ingot was annealed for 72h at 800°C to ensure that U-solid solution would have completely reacted. The ingot presented some U_3Si inclusions.

The arc melted ingot was milled with PEG milling aid, to reach a desired particle size distribution, ranging from 1µm to 10µm. The pellets were pressed in a die lubricated with zinc stearate. The pellets which achieved a density superior to 95.5% - the density required for fuel pellets - were prepared by burning off the PEG milling aid and adding a poly(ethylene oxide) resin in a tantalum

crucible. The pellets were sintered in a vacuum furnace at pressure in the 10^{-3} to 10^{-4} mbar range. The temperature was ramped up to 600°C at a rate of 2.5°C/min and held for 2h, then ramped at 30°C/min up to 1500°C and held for 4h. The pellets were naturally cooled and proved to have a density range of 96.1-97.8%.

SEM analyses revealed no U_3Si, pure U or pure Si phases in the sintered pellets. Open porosity was observed at the grain boundaries and at triple points as can be seen in Figure 3.

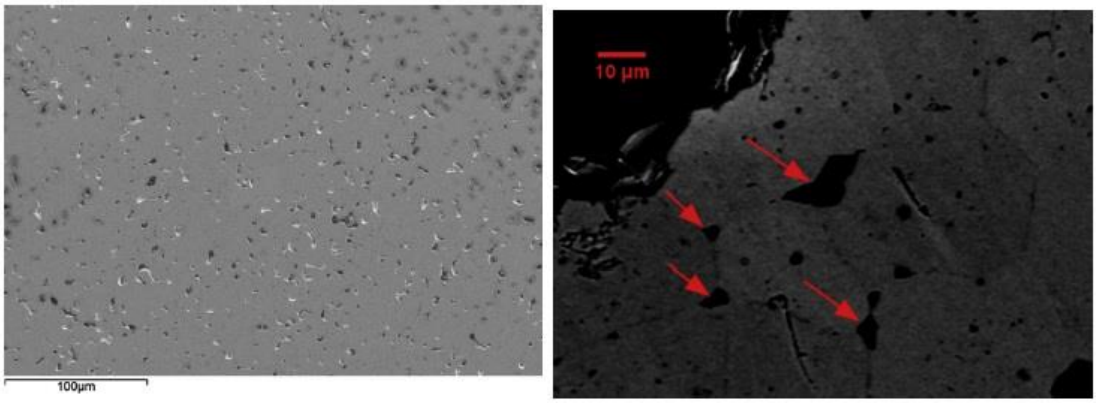

Figure 3: SEM secondary electron image showing the sintered microstructure of a 92.1% dense U_3Si_2 (left) and a SEM backscatter electron image showing the location of porosity in U_3Si_2 (right)

The method presented by Nelson *et al.* requires elevated temperatures and very long sintering times while the method presented by the Idaho National Laboratory had troubles getting highly-dense pellets without the use of additives, which created open pores. The Idaho National Laboratory method also requires a control on the particle size distribution during the milling step.

The objective of this work is to produce pellets with the required density, at lower temperatures and with much lower sintering times, thanks to Sparks Plasma Sintering. It also aims at showing that producing a more than 95.5% dense pellet without additives and without control of the particle size distribution is possible, using Spark Plasma Sintering as well.

2.4 FORMATION OF TERNARY PHASE U-Si-Mo

Molybdenum is a fission product and investigating its solubility in the U_3Si_2 matrix has therefore its importance.

The methodology employed in literature consists in mixing pure uranium, silicon and molybdenum in different proportions. This method proved to provide a matrix which was not U_3Si_2, and showed a very different morphology (Figure 4) from a U_3Si_2 fuel structure [16]. The ternary phases observed are there the result of a solidification process, i.e. the result of the interaction of liquid phases, involving a rapid diffusion of elements. It does not reflect the phases that could result from a solid-solid interaction.

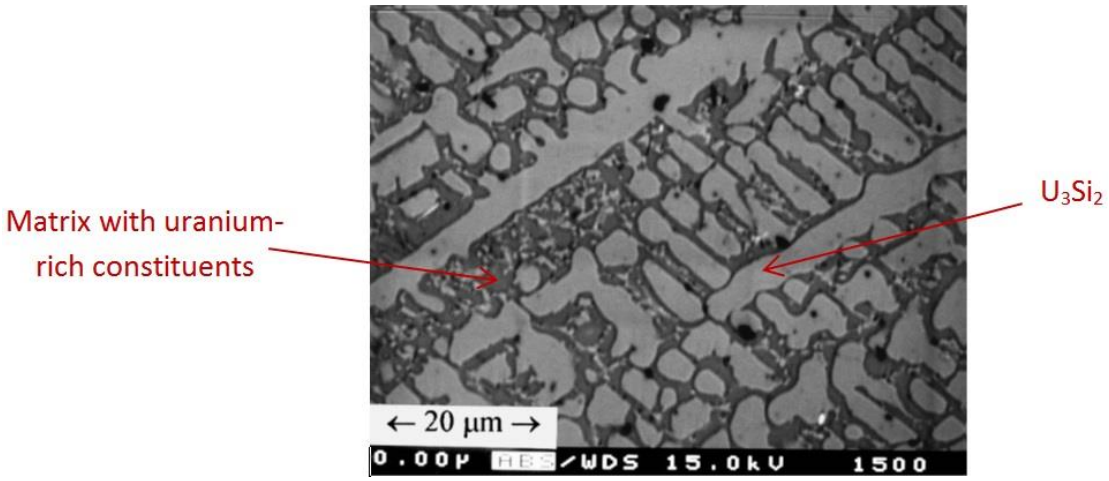

Figure 4: $U_{72}Mo_5Si_{23}$, as-cast alloy, EPMA-absorption image

Literature has reported a very low solubility of Mo in U_3Si_2, lower than 0.16at%[17]. Besides the very low solubility, the formation of ternary phases with different U/Mo/Si ratios was highlighted. The formation of $U_2Mo_3Si_4$ was put in evidence and it was observed that most of the surrounding phases engaged in a two-phase equilibrium with $U_2Mo_3Si_4$, such as U_3Si_2. It was therefore inferred a relatively high thermodynamic stability of this ternary compound. For the alloy containing 72 at.% of U, 5at.% of U and 23 at.%, $U_4Mo(Mo_xSi_{1-x})Si_2$ was also reported, and it proved to be at equilibrium with $U_2Mo_3Si_4$. They also reported the formation of γ-(U,Mo), as being in equilibrium with $U_2Mo_3Si_4$ and $U_4Mo(Mo_xSi_{1-x})Si_2$. Literature also reported the formation of U_3Si for the alloy $U_{72}Mo_5Si_{23}$[16].

The formation of U_3Si due to the presence of molybdenum could be problematic since it has poor irradiation behaviour. The work realized here aims at introducing molybdenum in an already existing U_3Si_2 matrix, which has not been done before, and investigate how the matrix adapts. It will use Spark Plasma Sintering for sintering, to observe the phases formed from the solid-solid interactions, this latter way of proceeding being closer to what happens during burn-up.

2.5 OXIDATION IN AIR

Studying the oxidation of a fuel enables to understand its reactivity in case of accident or in case it is exposed to air. Even though during an accident the fuel is more susceptible to be exposed to steam, studying the oxidation in air is a way to do a comparative study of U_3Si_2 with UO_2. The oxidation in air also gives the possibility to measure the heat realised during the oxidation, a data which is hard to get in steam.

Several papers have already recorded the oxidation behaviour of U_3Si_2 in air, doing a TG measurement. They recorded a mass gain of 20.8% or 21%, but none analysed the mass enthalpies[18,19]. Westinghouse has as well studied U_3Si_2 by doing a TG and a DSC measurement (see Figure 5).

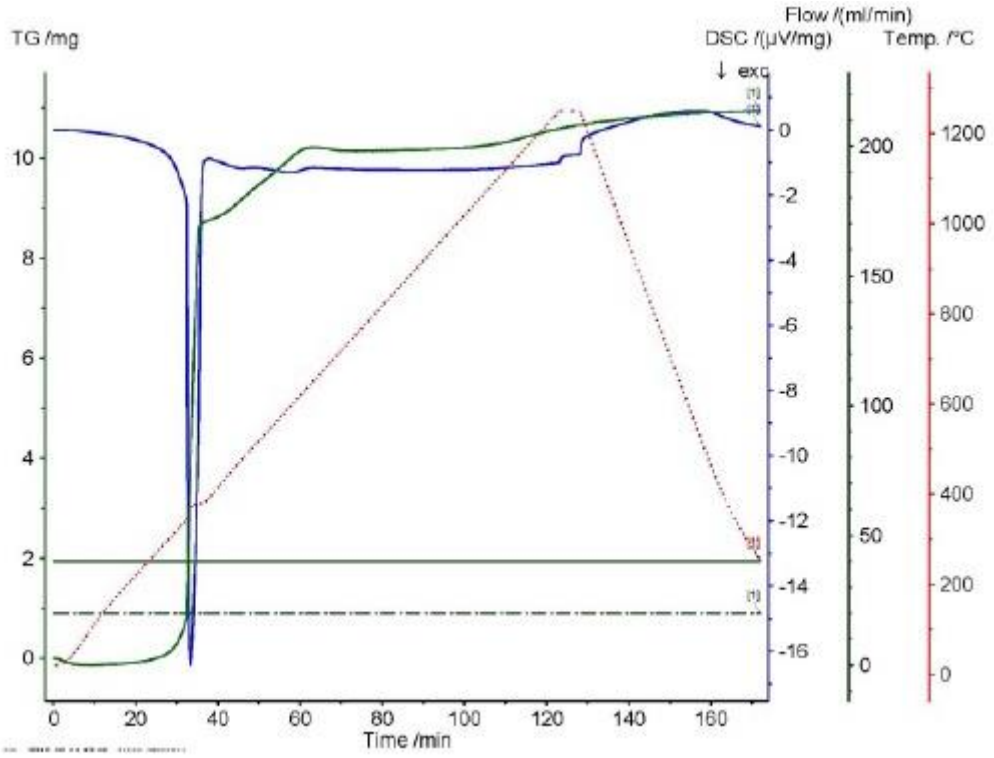

Figure 5: Typical TG+DSC signal for 10°C/min ramp to 1250°C for U_3Si_2 powder. The red plot is sample temperature in °C, the green plot is TG data mass gain in mg and blue plot is DSC data in µV/mg.

Sooby *et al.* have recorded by XRD the presence of U_3O_8 as the final product of the reaction[18]. To date, however, the oxidation product of silicon present in U_3Si_2 has not been identified. Johnson *et al.* proposed the Eq.(1), without being able to identify SiO[19]. The theoretical mass gain for Eq.(1) is of 20.8%.

$$U_3Si_2 + 5\ O_2 \rightarrow U_3O_8 + 2\ SiO \qquad m\%_1=20.8\% \qquad Eq.(1)$$

As shown in Figure 5, the TG curve increases first rapidly around 400°C and then increases more slowly to reach a final value. This observation suggests that the oxidation of U_3Si_2 is possibly a two-step reaction. It leads to think that U_3Si_2 first oxidizes to UO_2 and then to U_3O_8. To support this hypothesis, Sooby *et al.* reported UO_2 as an intermediate phase of the oxidation[18]. Nevertheless, Westinghouse reported that, after investigation, the oxidation of U_3Si_2 is a single-step reaction[3].

The present work therefore aims at assessing whether U_3Si_2 oxidizes in a two-step reaction and whether the silicon oxidizes. It will aslo compare the mass enthalpies of the oxidation of U_3Si_2 and of UO_2. TG and DSC measurements of the oxidation of U_3Si_2 and of UO_2 in air were recorded. Mass gains and reaction enthalpies were jointly analysed, which had not been done by Johnson *et al.* nor Sooby *et al.* This method was used to fill the gaps pointed out.

2.6 OXIDATION IN HYDROGEN PEROXIDE

Hydrogen peroxide is a product of radiolysis of water and would therefore be produced if water was exposed to radiations. Due to irradiation, other species than hydrogen peroxide are formed, such as radicals and anions.[20,21] Figure 6 shows the set of reactions happening during the radiolysis of water and their rate constants.

$OH\bullet + H_2 \rightarrow H\bullet + H_2O$	$k = 4.0\times10^{7}$	$OH\bullet + H_2O_2 \rightarrow HO_2\bullet + H_2O$	$k = 2.25\times10^{7}$
$OH\bullet + O_2^{-}\bullet \rightarrow O_2 + OH^-$	$k = 1.0\times10^{10}$	$H\bullet + O_2 \rightarrow H^+ + O_2^{-}\bullet$	$k = 2.0\times10^{10}$
$H\bullet + O_2^{-}\bullet \rightarrow HO_2^-$	$k = 2.0\times10^{10}$	$e_{aq}^{-}\bullet + O_2 \rightarrow O_2^{-}\bullet$	$k = 2.0\times10^{10}$
$e_{aq}^{-}\bullet + H_2O_2 \rightarrow OH\bullet + OH^-$	$k = 1.6\times10^{10}$	$e_{aq}^{-}\bullet + O_2^{-}\bullet \rightarrow HO_2^- + OH^-$	$k = 1.2\times10^{10}$
$e_{aq}^{-}\bullet + H^+ \rightarrow H\bullet$	$k = 2.2\times10^{10}$	$e_{aq}^{-}\bullet + H_2O \rightarrow H\bullet + OH^-$	$k = 2.0\times10^{1}$
$e_{aq}^{-}\bullet + HO_2^- \rightarrow O^-\bullet + OH^-$	$k = 3.5\times10^{9}$	$OH\bullet + HO_2\bullet \rightarrow H_2O + O_2$	$k = 1.2\times10^{10}$
$OH\bullet + OH\bullet \rightarrow H_2O_2$	$k = 4.0\times10^{9}$	$H\bullet + HO_2\bullet \rightarrow H_2O_2$	$k = 2.0\times10^{10}$
$H\bullet + H_2O_2 \rightarrow H_2O + OH\bullet$	$k = 6.0\times10^{7}$	$H\bullet + OH^- \rightarrow e_{aq}^{-}\bullet + H_2O$	$k = 2.0\times10^{7}$
$HO_2\bullet + O_2^{-}\bullet \rightarrow O_2 + HO_2^-$	$k = 8.5\times10^{7}$	$HO_2\bullet + HO_2\bullet \rightarrow H_2O_2 + O_2$	$k = 7.5\times10^{5}$
$H^+ + O_2^{-}\bullet \rightarrow HO_2\bullet$	$k = 5.0\times10^{10}$	$HO_2\bullet \rightarrow H^+ + O_2^{-}\bullet$	$k = 8.0\times10^{5}$
$H^+ + HO_2^- \rightarrow H_2O_2$	$k = 2.0\times10^{10}$	$H_2O_2 \rightarrow H^+ + HO_2^-$	$k = 3.56\times10^{-2}$
$OH\bullet + OH^- \rightarrow H_2O + O^-\bullet$	$k = 1.2\times10^{10}$	$O^-\bullet + H_2O \rightarrow OH\bullet + OH^-$	$k = 1.7\times10^{6}$
$H^+ + OH^- \rightarrow H_2O$	$k = 1.43\times10^{11}$	$H_2O \rightarrow H^+ + OH^-$	$k = 2.6\times10^{-5}$
$H\bullet + OH\bullet \rightarrow H_2O$	$k = 2.5\times10^{10}$	$H\bullet + H\bullet \rightarrow H_2$	$k = 1.0\times10^{10}$
$e_{aq}^{-}\bullet + H\bullet \rightarrow H_2 + OH^-$	$k = 2.0\times10^{10}$	$e_{aq}^{-}\bullet + e_{aq}^{-}\bullet \rightarrow H_2 + OH^- + OH^-$	$k = 5.0\times10^{9}$
$e_{aq}^{-}\bullet + OH\bullet \rightarrow OH^-$	$k = 2.0\times10^{10}$	$O^-\bullet + H_2 \rightarrow H\bullet + OH^-$	$k = 8.0\times10^{7}$
$O^-\bullet + H_2O_2 \rightarrow H_2O + O_2^{-}\bullet$	$k = 2.0\times10^{8}$	$OH\bullet + HO_2^- \rightarrow HO_2\bullet + OH^-$	$k = 5.0\times10^{9}$
$HO_2^- + O^-\bullet \rightarrow OH^- + O_2^{-}\bullet$	$k = 8.0\times10^{8}$	$e_{aq}^{-}\bullet + O_2^{-}\bullet \rightarrow HO_2^- + OH^-$	$k = 2.0\times10^{10}$
$OH^- + H_2O_2 \rightarrow HO_2^- + H_2O$	$k = 5.0\times10^{8}$	$HO_2^- + H_2O \rightarrow H_2O_2 + OH^-$	$k = 5.735\times10^{4}$

Figure 6: Radical reaction following radiolysis, k is in $M^{-1}.s^{-1}$

Even though other species than H_2O_2 are formed during the radiolysis of water, it was proven that this aqueous radiolysis product was mainly responsible for the oxidative dissolution of UO_2[22]. This is the reason why, in this work, the dissolution of U_3Si_2 was first studied in presence of hydrogen peroxide, added to the reaction media. The second step was to observe the dissolution of U_3Si_2 under irradiation. Studying the dissolution of U_3Si_2 in those conditions is both relevant in case of accident and for geological storage purposes, as detailed in sections 2.6.1 and 2.6.2.

2.6.1 Chemistry in a coolant

Hydrogen peroxide is being formed in the coolant of an operational nuclear reactor. In a Boiling Water Reactor (BWR), the coolant is at a pressure of 7.5MPa and with a temperature lower than 290°C. In a Pressure Water Reactor (PWR), the coolant is at a pressure of 15 MPa at a temperature around 350°C[23]. In these high-temperature conditions, the coolant is a bit acidic, with a pH around 5.8, since the equilibrium constant of the autoprotolysis of water increases with temperature. Using the conditions detailed in Table 2, recent modelling calculated the hydrogen peroxide concentration in steady-state to be 3.10^{-5}M and the oxygen level at 7.10^{-6}M[20]. In reality, the concentration in oxidant (H_2O_2 and O_2) is lower since the addition of hydrogen is widely used in the nuclear reactor industry to lower the corrosion potential[24].

Table 2: Conditions assumed for simulation of the coolant chemistry

Neutral water	pH=5.8
Temperature	300°C
Mixed radiation:	
Gamma rays	33%
2 MeV neutrons	67%
Dose rate:	
Gamma	3.3kGy/s
2 MeV neutrons	6.6 kGy/s

2.6.2 KBS-3: the Swedish geological repository

High-level waste, consisting of spent fuel, is today stored in an interim storage structure. Since it takes 100,000 years for the radioactive waste to reach the ground level, several countries have worked on the elaboration on a long-term geological storage. The Swedish solution, KBS-3, consists in a multi-layer protection. The fuel rods are inserted in copper canisters. The coper canisters are placed 500m below ground in holes dug in the bedrock. The system is sealed with bentonite clay, to adapt to the possible movement of the rock over time. It is a barrier as well in itself[25].

The objective is to have a system resistant enough to prevent the leaching of the radionuclides for the next 100,000 years. However, in case all the barriers fail, the contamination can travel through groundwater.

As U_3Si_2 is considered as a fuel, the way it is disposed in the back-end must be taken into consideration as well. If U_3Si_2 is to be disposed similarly to UO_2, it is then important to know at what rate the fuel would dissolve in case it is in contact with the groundwater.

As for the chemical conditions of the groundwater, deep in the bedrock, the oxygen level is low; therefore, it is rather a reducing environment. The groundwater contains bicarbonate coming from the dissolution of carbon dioxide.

2.6.3 Previous studies

To the author's knowledge, the only study of U_3Si_2 dissolution with hydrogen peroxide comes from a work realized by Argonne National Laboratory, in order to recover ^{99}Mo from low-enriched uranium silicide targets for medical applications. They optimised the dissolution process using 0.2 to 0.5M NaOH and 5 to 7M H_2O_2 at 80-90°C[26]. In these conditions, they proposed the equation presented in Eq.(2) [27].

$$U_3Si_2 + 25\ H_2O_2 + 10\ OH^- \rightarrow 2\ SiO_3^{2-} + 3\ UO_2(O_2H)_4^{2-} + 24\ H_2O \qquad \text{Eq.(2)}$$

They reported as well that during the dissolution of U_3Si_2, two chemical reactions would occur: both the autodestruction of hydrogen peroxide, catalysed in base, (Eq.(3)) and the dissolution of U_3Si_2.

$$2\ H_2O_2 \rightarrow 2H_2O + O_2 \qquad \text{Eq.(3)}$$

Studies evaluating the dissolution rate in presence of hydrogen peroxide have been done so far only for UO_2. The mechanism reported in Figure 7 describes the dissolution of UO_2 by the oxidation of U(IV) to U(VI)[22].

$$H_2O_2 + UO_2 \rightarrow OH^{\bullet} + OH^- + UO_2^+$$

$$UO_2^+ + OH^{\bullet} \rightarrow UO_2^{2+} + OH^-$$

Figure 7: Mechanism of dissolution of UO_2 by hydrogen peroxide

The decomposition of hydrogen peroxide has been observed to be catalysed by the presence of UO_2 and follows the mechanism described in Figure 8 [22].

$$H_2O_2\ (ads) \rightarrow 2HO^{\bullet}\ (ads)$$

$$H_2O_2\ (ads) + HO^{\bullet}\ (ads) \rightarrow H_2O\ (ads) + HO_2^{\bullet}\ (ads)$$

$$2HO_2^{\bullet}\ (ads) \rightarrow H_2O_2 + O_2$$

Figure 8: Catalytic decomposition of hydrogen peroxide in presence of UO_2

The dissolution rate of UO_2 with hydrogen peroxide has been studied on powder[28] and has been evaluated as a function of pH[29]. The dissolution of UO_2 has been studied as well on pellets under irradiation[30] and in the presence of fission products under irradiation[31].

3. THESIS OBJECTIVES

The first objective of this thesis is the production and characterization of U_3Si_2 pellets for nuclear applications. These pellets should have a density above 95%, consistent with as-fabricated UO_2 pellets, and contain a low amount of secondary U_3Si phase, which can be formed during the process. First, U_3Si_2 alloys were produced by arc melting then milled into powder, which was then sintered into U_3Si_2 pellets by Spark Plasma Sintering.

The second objective is the incorporation of molybdenum (Mo) into the U_3Si_2 matrix. Mo is one of the principal fission products and how it will be incorporated in the crystallographic structure is an important data regarding the fuel stability under irradiation.

The third objective is evaluating the oxidation resistance of U_3Si_2 in air and in presence of hydrogen peroxide. The oxidation in air will be studied using TG and DSC measurements, while the reaction in presence of hydrogen peroxide will be followed by absorbance measurements. This objective is to evaluate the possible consequences during an accident in a LWR, if the fuel were to be in contact with the coolant or with air. This approach will also enable studying its reactivity with groundwater in case of a future geological repository.

4. MATERIALS AND METHODOLOGY

4.1 FABRICATION METHODOLOGY

4.1.1 Arc melting

Arc melting is a technique used to produce ingots of a desired alloy. A strong voltage and high current is set at the W-Th electrode in an argon atmosphere to create plasma. The two pieces of metal are placed in a water-cooled conductive copper hearth, which is the anode. The cathode is oriented towards the sample and the plasma arc heats up the sample, melting it and creating the desired alloy.[32] The elements described previously are shown in Figure 9.

Figure 9: Arc melter used for melting the alloys

For a W-Th cathode, and a gas flow of 5L/min of argon, the surface temperature can reach up to 3500°C when the cathode is less than 1mm close to the sample[33], which is enough to melt both uranium and silicon.

The material was loaded in a copper holder, inserted from the bottom and that would seal the copper hearth. The copper holder was immobilized with a set of wooden pieces. The raw uranium was put on the top of the raw silicon in the copper holder, and it was arc melted several times for two reasons. First, because the installation would get too hot after a couple of seconds and second, to be able to flip the sample each time to reach a better homogeneity.

Arc melting was used here to produce U_3Si_2 alloys, as presented in section 5.1.1.

4.1.2 Milling

The ingots of alloy needed to be milled into powder to produce pellets with the desired characteristics. The milling was done with the milling machine shown in Figure 10. The ingots are placed in a metallic cylinder with a set of metallic balls. The cylinder is immobilized by a locking system. The cylinder is then set to rotation and the machine follows the program set by the user.

Figure 10: Retsch PM 100 in a glovebox used for milling

The milling step was realized in a glovebox to limit the possible oxidation of U_3Si_2. Since a powder has a higher specific surface area than an ingot, its reactivity is increased towards oxygen. The glovebox helped limiting the contamination of the powder with UO_2 or U_3O_8.

The rotation speed was set at 500rpm, with direction reversal every 2min. Fifty 5-millimeter balls were introduced and the program was run for 10min. Since the alloys were not fully milled the first time, it was decided to run the same program for another 10min, this time with seventy 5-millimiter balls.

4.1.3 Spark Plasma Sintering

Spark Plasma Sintering is a method for sintering conductive material. It is used in inert atmosphere or low vacuum. It was used here for the sintering of the U_3Si_2 powder into pellets, as presented in section 5.1.3. The material is placed in a graphite die and closed by two graphite punches. A graphite foil is used to line the die, for an easier removal of the pellet from the die after sintering. A schematic of SPS process and the equipment employed is shown in Figure 11.

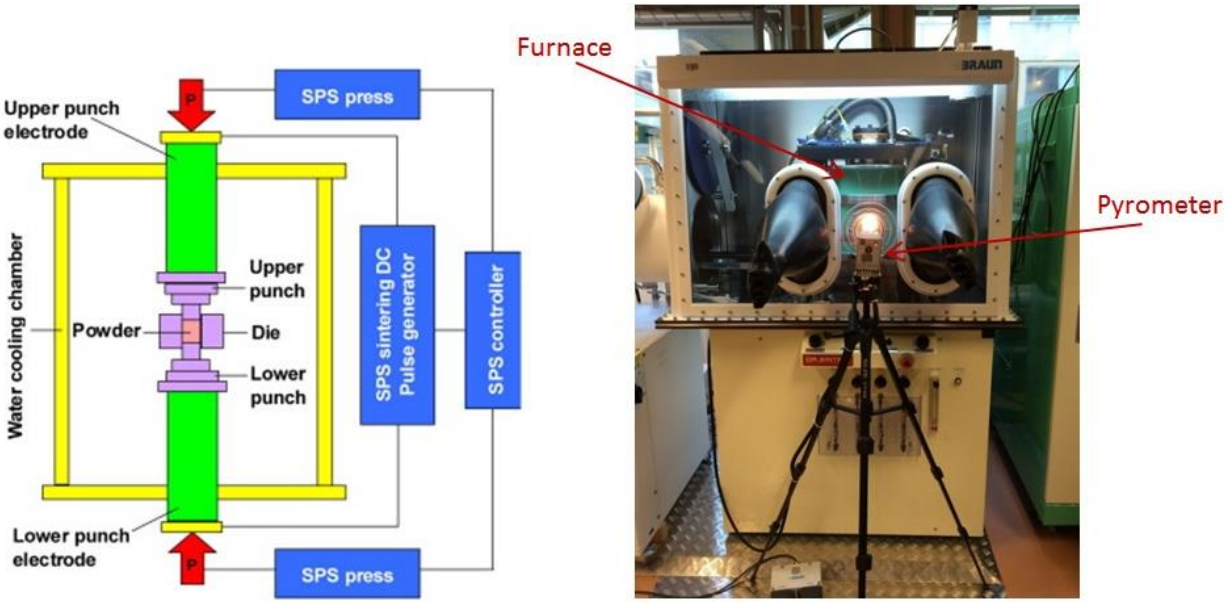

Figure 11: Schematic of SPS process[34](left) and the DrSinter SPS-5.40MK-VI (right) used for sintering

During the sintering process, pressure can be applied on the material, while a highly-energetic current passes through the material to sinter it. A pyrometer placed in front of the furnace measures

the IR intensity of thermal radiation and therefore the temperature at the point of measurement. Using this information, the SPS machine adapts the current to maintain the temperature set by the user.

The pulsed current goes from the upper graphite punch and gets divided: a part goes through the graphite die, generating heat by Joule effect, while the other part goes through the powder material itself[35], as illustrated in Figure 12. Electrical discharges in between the particles of powder create plasma, which contributes to a fast and efficient sintering process[34]. The spark discharge can eliminate adsorptive gas and any impurities that are present on the surface of particles[34]. The particles of powder also experience heating by Joule effect which leads to the local fusion of particles[35].

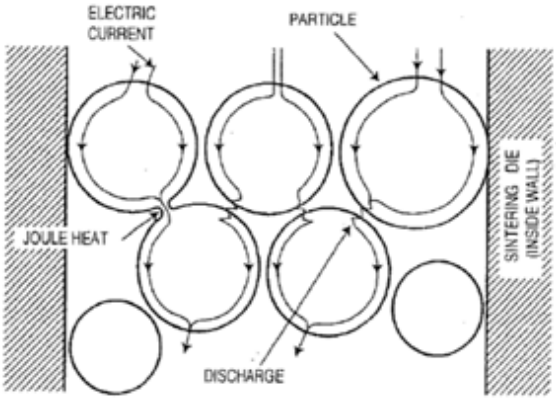

Figure 12: Schematics of the powder sintering under SPS[36]

The pressure applied during the process enhances the sintering by aiding in particle re-arrangement[37] to achieve a dense material.

Compared to conventional sintering, SPS enables the sintering of powders with lower temperatures, little grain growth and shorter holding times. It provides high heating rates thanks to the Joule effect and leads to a significant enhancement of the thermal diffusion of the sintered material.[34]

4.2. OXIDATION IN PRESENCE OF HYDROGEN PEROXIDE: METHODOLOGY

4.2.1 Experimental conditions

The results of the experiments described here are reported in section 5.4.

- Hydrogen peroxide

Hydrogen peroxide is a product of the radiolysis of water. It is therefore present in both the water used as a coolant in LWR, and present as well in case the water reaches the copper canister.

The reactivity was studied with U_3Si_2 powder. The powder has a greater reactivity than a pellet which makes it easier to observe phenomena. This is the reason why the powder was chosen over the pellet, even though in case of accident and in case of geological repository the material exposed will be a cracked pellet and not a powder.

All the experiments were carried out in a small bottle, with a total volume of reaction media of 25mL, containing milli-Q water and $NaHCO_3$ in 10mM concentration. HCO_3^- is traditionally present in groundwater, coming from the dissolution of CO_2 in water. During previous experiments made with UO_2, it has been observed that HCO_3^- would help the dissolution of UO_2 by complexing with UO_2^{2+}. It was added here in order to be able to compare more easily already carried out experiments with UO_2 in the same conditions. The reaction media was purged with N_2 for 20min before addition of the powder.

The U_3Si_2 powder was added in 50mg and covered with alumina to isolate it from light. It was done to prevent any photoreaction from happening, which would make it difficult to understand the reaction since it can be a source of the formation of radicals.

The U_3Si_2 powder was then added in a glovebox with an oxygen level inferior to 0.1ppm, with a mass of 50mg. The experiment was then carried out outside of the glovebox, under a flow of N_2. The hydrogen peroxide was added last, to reach a final concentration in the reaction media of 0.2mM. Its introduction in the media would launch the chronometer of the experiment.

- ### Uranyl experiment

A 25mL solution of 10mM $NaHCO_3$ containing 50mg of U_3Si_2 powder was prepared similarly to the hydrogen peroxide experiments presented above. Uranyl was added outside the glovebox, under a flow of N_2, and to reach a concentration of 0.06mM. Its introduction in the media would launch the chronometer of the experiment. No hydrogen peroxide was added.

- ### Radiation experiment

50mg of powder was poured in a glovebox, in a 25mL solution of 10mM $NaHCO_3$ purged with nitrogen gas for 20min. The solution was irradiated with a gamma-source at 0.1 Gy/s under nitrogen flux, as shown in Figure 13. The experiment was repeated twice, the second time for a longer time.

Figure 13: Gammacell 1000 Elite MDS Nordion (left) and the experimentation set-up (right)

Another experiment was realised to monitor the formation of hydrogen peroxide as a function of the dose without the presence of U_3Si_2. 25mL of 10mM $NaHCO_3$ purged with N_2 for 20min was put in the gamma cell for 3 hours under N_2 flow.

4.2.2 Analytical methods

The analytical methods described here were used to follow the reactions described in the section 5.4.

The reactions were followed by spectrophotometry. Both the concentration of H_2O_2 and dissolved U(VI) were monitored.

At separate times, 1 to 2mL was removed from the media, filtered through a 0.20µm cellulose acetate syringe filter. This step filters the powder from the reaction media and therefore stops the reaction in the filtrate. The filtrate was then analysed to determine the concentration in H_2O_2 and in U(VI).

For the measurement of the concentration of H_2O_2, 200µL sample would be taken from the filtrate, diluted with water. It was added 100µL of potassium iodine and 200µL of $(NH_4)_6Mo_7O_2 \bullet 4H_2O$ and sodium acetate. The ammonium salt and sodium acetate were used as a catalyst. In presence of hydrogen peroxide, I^- oxidizes to I_3^-. The concentration of I_3^- was measured at 360nm in order to know the concentration in hydrogen peroxide, accordingly to the Ghormley method[38].

For the measurement of U(VI), a volume from 750µL to 1mL of sample would be taken from the filtrate and diluted with water. Hydrogen chloride, a strong acid, and the Arsenazo III reagent (see Figure 14) were added. Arsenazo III forms a colourful complex with U(VI), but requires a pH between 4 and 1[39], explaining the addition of HCl. The concentration of the colourful species coming from the complexation of U(VI) with Arsenazo was measured at 653nm.

Concentrations in H_2O_2 and in U(VI) could be deduced from the absorbance measurements thanks to calibration curves previously established.

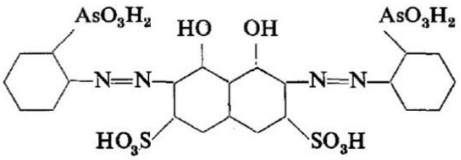

Figure 14: Arsenazo III

4.3. CHARACTERIZATION

4.3.1 Density Measurement

The density measurements of the produced pellets and alloys were realized using the Archimedes' principle. It states that "any body completely or partially submerged in a fluid at rest is acted upon by an upward force, the magnitude of which is equal to the weight of the fluid displaced by the body" [40]. In the present work, chloroform was used as the displacement fluid. The apparent weight of the material in chloroform is: $G_{app}=G-F_a$, with G the weight of the material and F_a the Archimedes' force. It leads to the Eq.(4).

$$\rho_s = \frac{m_s}{m_s - m_{chlo}} * \rho_{chlo} \quad \text{Eq.(4)}$$

where ρ_s is the density of the material, ρ_{chlo} the density of chloroform, m_s the dry mass of the material and m_{chlo} the mass of the material in chloroform. The setup used for the density measurement can be seen in Figure 15.

Figure 15: Setup for density measurements

4.3.2 SEM (EDS, SE, BSE)

The Scanning electron microscopy was used in sections 5.1 to 5.4 to analyse the microstructure, the chemical composition of the powder, of the alloys and pellets.

A scanning electron microscope (SEM) was used to obtain micro- or nano-scale images. The sample is placed in a chamber under vacuum, where it is irradiated with electrons. The analysis of the interaction of these electrons with matter provides images of the external morphology (Secondary Electrons, SE), as well as of the difference in chemical composition (Backscattered Electrons, BSE)[41]. Only SE and BSE were used in the present work.

The SEM images using SE are formed by analysing the intensity of the emitted secondary electrons as a function of irradiation position on the sample[42]. The electrons irradiated penetrate the sample in a teardrop-shaped volume – as modelled in Figure 16 - whose dimensions depend on the energy of the electron-beam, the atomic masses of the elements and the angle of incident.[43]

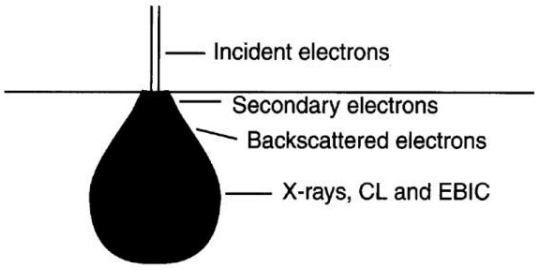

Figure 16: The sample-beam interaction volume and the regions from which SE, BSE and X-rays may be emitted[43].

The SE are electrons that escape from the sample with energies below 50eV, mainly knocked out of their orbits around an atom by an incident electron. They can only escape from a very shallow, near-surface layer of material.

BSE penetrate deeper in the sample. An accelerated electron from the incident beam is susceptible to produce a variety of elastic and inelastic collisions with the atoms of the sample. Elastic scattering changes the trajectory of an incoming electron without significant change in the kinetic energy. These elastic collisions are more likely to happen with atoms of a great atomic number, because of a bigger cross-sectional area. The number of BSE reaching the detector is

proportional to the mean atomic number of the sample. A brighter area is correlated with a greater Z average and a darker area has a lower Z average.[44]

The Energy-Dispersive spectrometry (EDS) enables a chemical identification by the analysis of the X-ray signal generated by the interaction of the beam with the sample. When the sample is irradiated by the SEM's electron beam, electrons are ejected from the atoms in the sample's surface. Electrons from a higher state will fill the electron vacancies, resulting in the emission of X-ray. The energy of the X-ray is characteristic of the element from which it was emitted. The EDS detector measures the relative abundance of the emitted X-rays for each energy detected, which enables a quantification of the amount of each element present in the sample.[45] EDS placed on a SEM cannot detect very light elements (H, He and Li)[41]. However, a proper quantitative analysis requires the calibration with standards of known composition for the elements investigated.[46] In the present work, the EDS analysis was only used to have an idea of the relative proportions of the elements present in the sample.

Two different SEM were used here: a XL-30 field emission ESEM microscope equipped for EDS, and another one for images with higher resolution, a FEG SEM-Jeol 7800F also equipped with EDS. The equipment is shown in Figure 17.

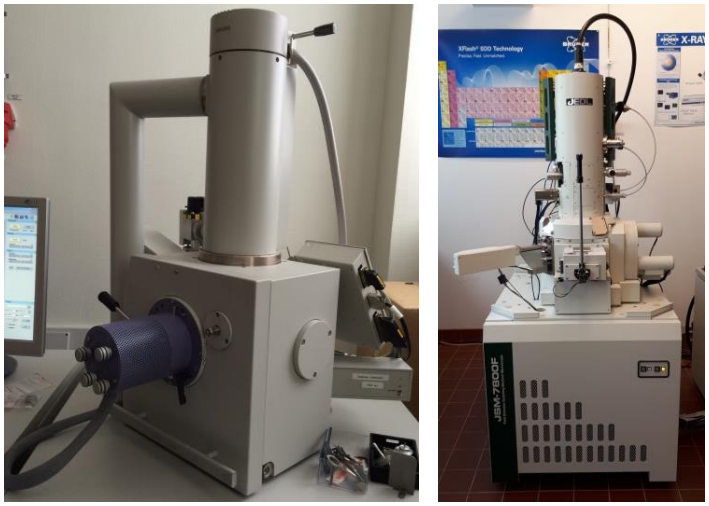

Figure 17: XL-30 field emission ESEM microscope (left) and FEG SEM-Jeol 7800F (right)

4.3.3 Sample preparation and LOM

- Light Optical Microscopy (LOM)

An optical microscope amplifies the image of a sample through a set of lenses. The optical microscope is made of a first set of lenses close to the eyes of the observer, which form the ocular of the microscope. Another set of lenses are placed in series with the ocular to form the microscope objective. The sample is placed under the objective and in the path of a source of light.

An optical microscope has several objectives and the user can go from an objective to the other by a rotative system. The objectives have different magnifications, which enables the user to observe the sample at different scales. The optical microscope used here has a magnification from times 50 to times 1000.

- Alloys

The samples were polished by hand. The first steps of grinding were realised using SiC paper, before polishing using Struers DP-Dac with a low resilience and diamond suspension. A suspension of 9, 6, 3, 1 and 0.25 µm were used successively. The samples were etched with nitric acid with a concentration of 8 M.

- Pellets

The pellets were polished by hand, and had a very different polishing behaviour than the alloys. The grinding was realised with SiC paper and the polishing was done using Struers DP-10 with a high resilience and diamond suspension. Suspensions of 9,3 and 1 µm only were used. Smaller diamond particles were found to damage the matrix. On some occasions, a last polishing step was added using colloidal silica mixed with water with the ratio 1:1 in volume. The etching was realized using a mix of acetic acid 80% with nitric acid 65% with a volume ratio of 70/30[47].

4.3.4 XRD

XRD stands for X-rays diffraction. It enables the identification of a material by using its crystallographic properties. The technique is therefore only useful for the identification of crystals and is unable to identify amorphous structures.

The sample is irradiated with X-rays and the source varies the angle with the sample. The detector collects the intensity for each angle (see Figure 18). The intensity that is collected by the detector after having interacted with the sample, follows Bragg's law, as shown in Eq.(5).

$$2 * d_{hkl} * sin\theta = n * \lambda \qquad \text{Eq.(5)}$$

d_{hkl} is the distance between two crystalline planes of Miller indexes h,k,l,
θ is the angle between the source and the sample,
n is an integer,
λ is the wavelength of the X-rays.

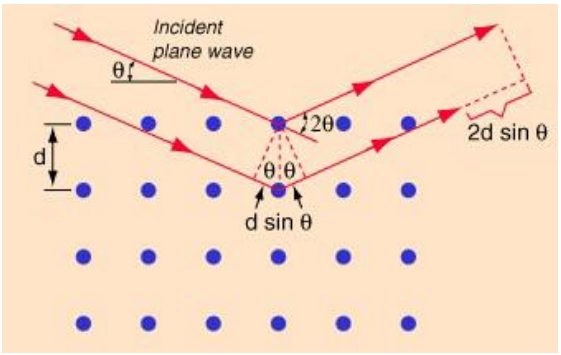

Figure 18: Illustration of Bragg's law[48]

The detector collects intensity when the interaction between the two incident waves, which have interacted with the crystal, is constructive. The interaction is constructive for specific distances d_{hkl} and specific angles, this is how the crystallographic structure can be identified.

d_{hkl} can be calculated from the experimental spectrum, using Bragg's law, all the other parameters being known. It is then possible to identify the Miller indexes of the family of planes that was involved in the constructive interaction. For a tetragonal system (like U_3Si_2), d_{hkl} is written in Eq.(6), as an example.

$$d_{hkl} = \frac{1}{\sqrt{\frac{h^2+k^2}{a^2}+\frac{l^2}{c^2}}} \qquad \text{Eq.(6)}$$

with a and c the lattice parameters.

The experimental XRD graphs are compared to a database, to identify the right compound.

The XRD graphs were realized with a Siemens D5000 X-ray diffractometer, using a Cu k-alpha target at 40 mA and 35 kV, shown in Figure 19.

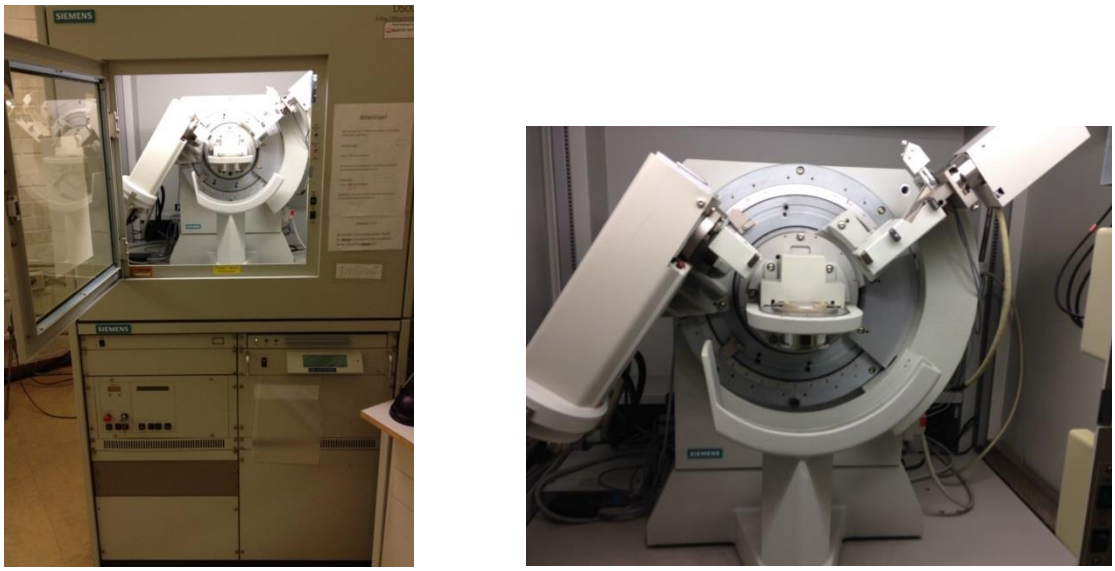

Figure 19: Siemens D5000 X-ray diffractometer

The XRD spectra for powder were realized using an air-tight dome, shown in Figure 20, to prevent the oxidation of the powder during the measurements.

Figure 20: Bruker Model A100B138-B141

4.3.5 DSC and TG

Differential Scanning Calorimetry (DSC) is the analysis of a sample's behaviour with temperature: it is used to measure melting temperature, fusion enthalpy, phase transformation temperature and energy, specific heat or heat capacity with time.

The sample is placed in a crucible and heated up according to a temperature profile. The energy released is measured and compared to the heat emitted from an empty crucible, the reference, as shown in Figure 21.

Thermogravimetric analysis (TG) analyses the mass gain during the temperature profile. It compares the mass in real time with the initial mass. One of the advantages is the precision of the measurements – range of µg to ng – which enables detection of oxidation process in the primary stages.

The experiments conducted to study the oxidation behaviour of U_3Si_2 were performed in synthetic air.

Figure 21: Netzsch STA 449 F3 Jupiter for DSC and TG

The equipment employed in this work shown in Figure 21 performs thermal analysis DSC/TG simultaneously. It has the advantage to provide perfectly identical test conditions for the TG and DSC measurements and an improved analysability of the results since two sets of information concerning the sample are always simultaneously available.

This equipment was used to assess the oxidation behaviour in air of U_3Si_2, reported in section 5.3.1.

4.3.5 FTIR

The infrared spectroscopy (IR) relies on the absorbance of some specific radiations by the sample, while others are transmitted. It enables the identification of bonds in a molecule or in a solid[49], similar to a finger print[50]. The equipment is shown in Figure 22.

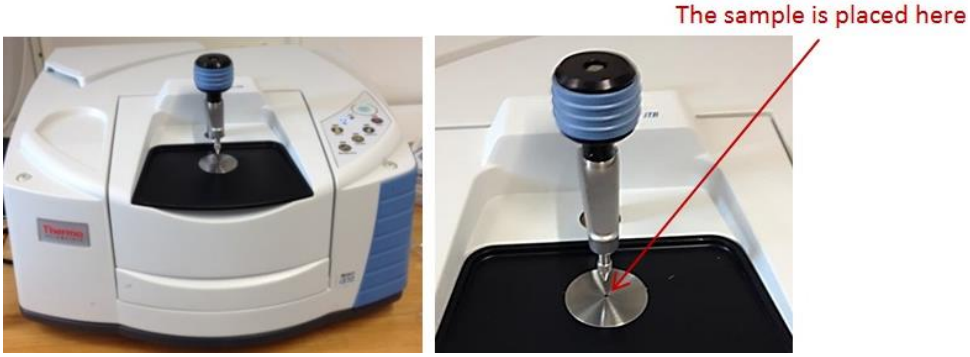

Figure 22: Thermo Scientific Nicolet iS10 used for IR analysis

The sample is placed in the path of a laser, generated from a heated ceramic filament containing rare-earth oxides. It emits radiations as heated.

A typical vibrational energy is around 0.01-0.1 x 10^{-18}J, which means that the frequency of the radiation should be around 10^{13}-10^{14} Hz, which is infrared. The transitions are however expressed in terms of wavenumbers, which lie in between 300-3000 cm^{-1}.[51]

An important condition to have an infrared absorption is that the electric dipole moment of the molecule must change during the vibration. However, the molecule does not necessarily need a permanent dipole, but only a change in dipole moment, possibly from zero. This oscillating dipole can then interact with the magnetic field. The absorption to a higher vibrational level occurs when the incident radiation provides photon with this specific energy.[51]

FT, in FTIR, stands for Fourier transform spectrometer, which means that the signal is decomposed according to the Fourier transform in order to separate each frequency[50]. Fourier transform spectrometers usually have a higher sensitivity than conventional spectrometers[51].

This technique was used to identify the products of the oxidation in air of U_3Si_2, presented in section 5.3.2.

4.3.6 Raman

Raman is a technique used to identify bonds but, unlike IR, it enables a quantitative analysis as well. It was used in section 5.3.2.

It relies on the interaction of a photon with vibrational levels of the molecules. Here, the photon leaves some energy in the vibrational modes of the molecule it strikes (Stokes-Raman scattering), or collects additional energy from a vibration that has already been excited (Anti-Stokes Raman scattering)[51,52]. It is illustrated in Figure 23.

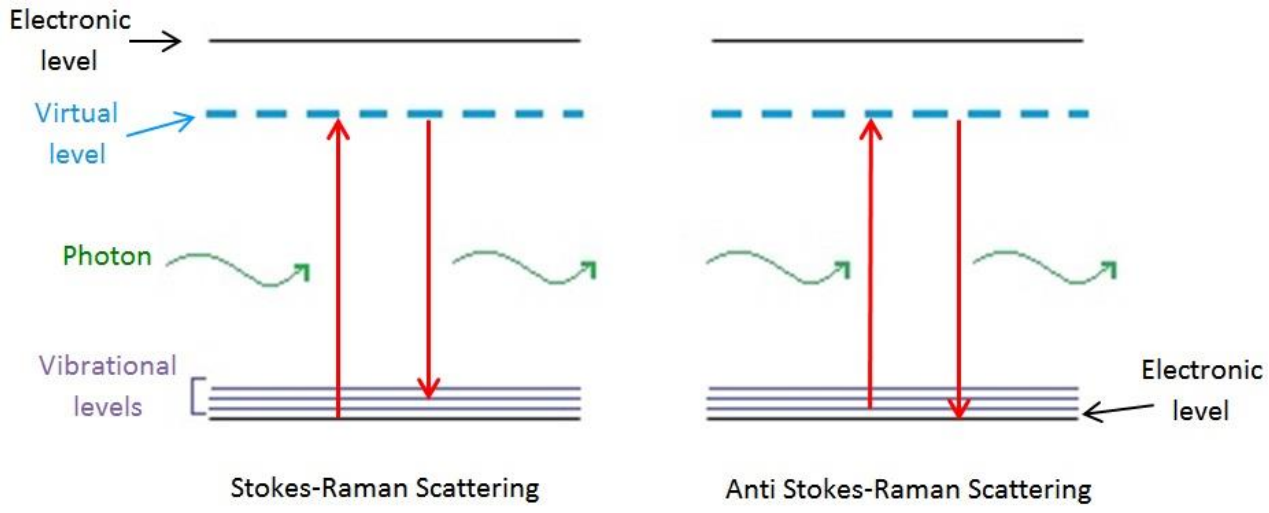

Figure 23: Stokes-Raman and Anti Stokes-Raman scattering

The molecular polarizability that changes as the molecule vibrates is here a crucial factor. The bond must be squeezed and stretched by the incident radiation so that a vibrational excitation may occur during the interaction with a photon. It is thus sensitive to both homonuclear and heteronuclear diatomic molecules, unlike IR, where homonuclear diatomic molecules cannot be detected[51].

As the absorption of a photon for Raman happens one every $30x10^6$ photons, it is necessary to use a monochromatic laser for a high photon density[52].

4.3.7 Oxygen analysis

The oxygen analysis is realized using the inert fusion method. A small amount of sample is burnt in a carbon crucible under a flow of helium gas. The oxygen present in the sample forms CO or CO_2, which is detected by infrared[53]. A LECO TC436DR was used here which, after calibration, has an accuracy of ±10% of the measured value in wppm[32]. The equipment is shown in Figure 24.

Figure 24: LECO TC436DR

The oxygen analysis was used to measure the level of oxygen in the freshly-milled U_3Si_2 powder (section 5.1.2).

4.3.8 Absorbance measurements

The absorbance measurements realized in this thesis were done using a spectrophotometer and quartz cuvettes. A beam of light is shined towards the cuvette containing the solution. For a specific wavelength, the spectrophotometer calculates the ratio between the transmitted intensity (I_t) and the initial intensity (I_0). The absorbance is then calculated as indicated by Eq.(7).

$$Absorbance\ (A) = -\log(\frac{I_t}{I_0}) \qquad \text{Eq.(7)}$$

For a certain range of concentrations, the absorbance follows the Beer-Lambert's law shown in Eq.(8).

$$A = \sum_i \varepsilon_i c_i l \qquad \text{Eq.(8)}$$

ε_i being the molar absorbance of the species i
c_i being the concentration of the species i
l the width of the cuvette.

Beer-Lambert's law was used in this thesis to link absorbance and concentrations. Calibration curves for both H_2O_2 and U(VI) had been previously established to this work. The calibration curves are prepared with a set of known concentrations of the studied absorbing species. For each known concentration, the absorbance is measured. When absorbance is plotted against the concentration in absorbing species, a linear relation between absorbance and concentration in the cuvette comes out, as Beert-Lambert's law predicts. Using this proportional relation, it is then possible to know an unknown concentration in a cuvette by measuring its absorbance.

A Thermo Scientific Genesys 20 spectrophotometer was used for the absorbance measurements (Figure 25).

Figure 25: Spectrophotometer Therno Scientific Genesys 20

Absorbance measurements were realized in section 5.4 in order to follow the dissolution of U_3Si_2 in presence of hydrogen peroxide.

5. RESULTS AND DISCUSSION

5.1 PELLET FABRICATION

5.1.1 Alloys

According to the phase diagram shown in Figure 1, only a precise composition of 40 mol% of Si and 60 mol% of U would give pure U_3Si_2. If there is a slight excess of silicon, there will be the formation of USi mixed with U_3Si_2. On the other hand, if there is a lack of silicon, U_3Si_2 and U_3Si will be formed. In the case of LWR applications, it is preferable to have a mix of U_3Si_2 with USi since U_3Si has a low melting temperature and a poor behaviour when irradiated.

Several alloys were prepared. Two pieces of pure uranium and pure silicon in the right proportions were arc melted several times, each in argon, to produce ingots, an example of which is shown in Figure 26.

Figure 26: Ingot of U_3Si_2

Table 3 is a summary of the alloys produced and Table 4 reports the densities of the compounds susceptible to be present in the ingots.

Table 3: Alloys produced by arc melting

	Total Mass (g)	**Density**	**%TD compared to U_3Si_2**
$U_3Si_2^{\text{Alloy 10A}}$	15.66	12.31	101
$U_3Si_2^{\text{Alloy 06}}$	15.27	12.32	101
$U_3Si_2^{\text{Alloy 06A}}$	7.652	12.17	99.8
$U_3Si_2^{\text{Alloy 06B}}$	7.269	12.49	102
$U_3Si_2^{\text{Alloy 06B}}$ re-melted	+0.0593 of Si	12.28	101
$U_3Si_2^{\text{Alloy 01}}$	13.68	12.30	101
$U_3Si_2^{\text{Alloy 10B}}$	6.929	12.27	101

Table 4: Theoretical densities of some uranium silicides

	Theoretical density
U_3Si_2	12.2[8]
U_3Si	15.4[54]
USi	10.4[55]

The $U_3Si_2^{Alloy\ 06}$ alloy was cut in half between $U_3Si_2^{Alloy\ 06A}$ and $U_3Si_2^{Alloy\ 06B}$. Their difference in density shows the presence of a heterogeneity in the sample. The alloy $U_3Si_2^{Alloy\ 06B}$ was then re-melted by adding a small mass of silicon. It was supposed that, since $U_3Si_2^{Alloy\ 06B}$ had a higher density than U_3Si_2, another phase with a higher density was present. The silicon was added to push the composition in the more silicon-rich part of the diagram, to obtain more U_3Si_2.

Almost all of the as-cast alloys have a higher density than the theoretical density of U_3Si_2. This observation was explained by the analysis of the ingots.

The cross-sections of the alloys were observed with the optical microscope. All the alloys presented similar features. The preparation by arc-melting led to the formation of large grains, usually around 100µm, separated by a brighter interphase, as shown in Figure 27. The matrix was assumed to be U_3Si_2 while the bright interphase, to be identified later, may explain the high density that was measured.

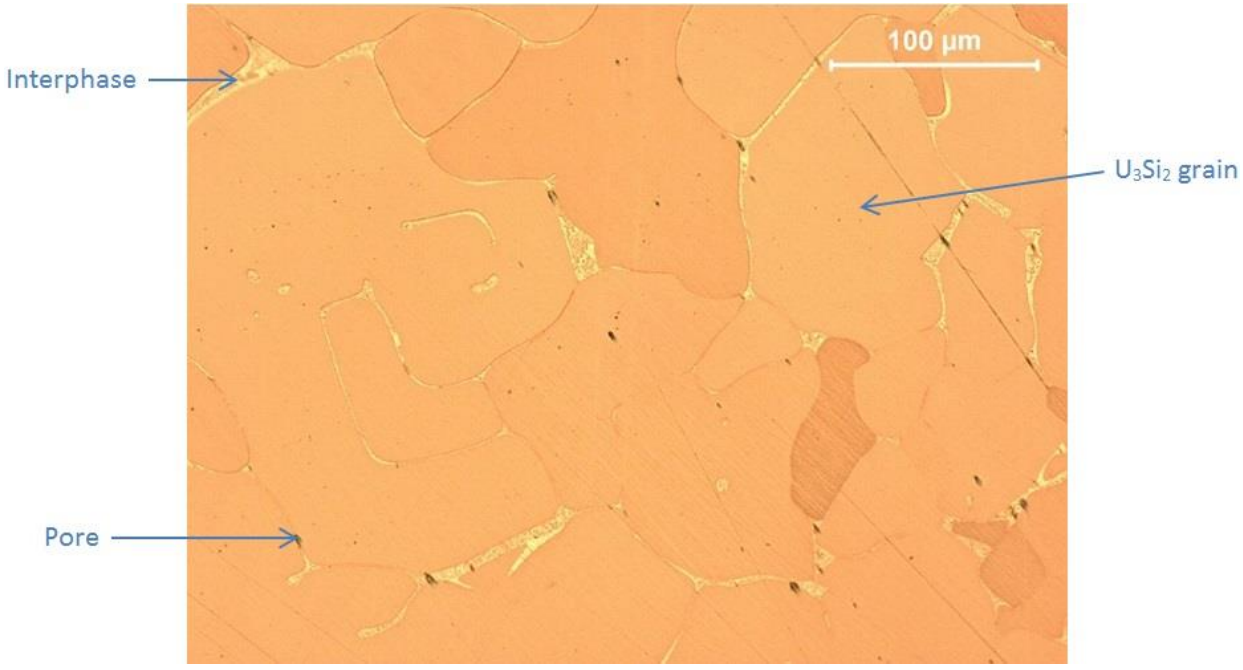

Figure 27: $U_3Si_2^{Alloy\ 10A}$ x200

The alloys appeared very dense with a small amount of pores. The pores have a “comet-tails” shape because the polishing was realised by hand and the material was pushed too hard. This kind of artefact disappears when automated polishing is used.

$U_3Si_2^{Alloy\ 06B}$ was re-melted by adding silicon. The shape of the grains appeared to be different after the second arc melting, as shown in Figure 28. The grains were smaller and even though in between the grains the interphase was still there, it was present in a much smaller amount (see Figure 27 and Figure 29).

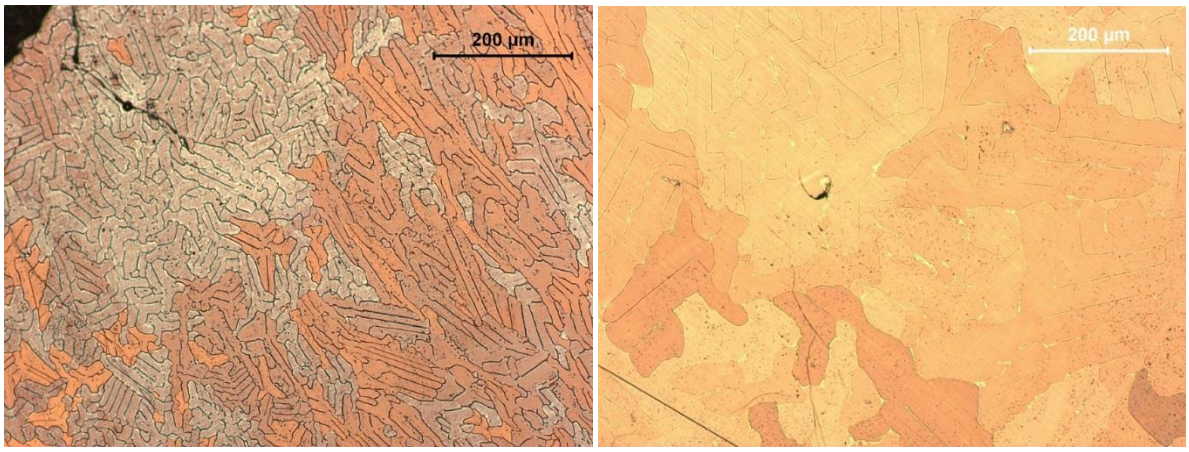

Figure 28: $U_3Si_2^{Alloy\ 06B}$ re-melted x100 (left) and $U_3Si_2^{Alloy\ 06A}$ x100 (right)

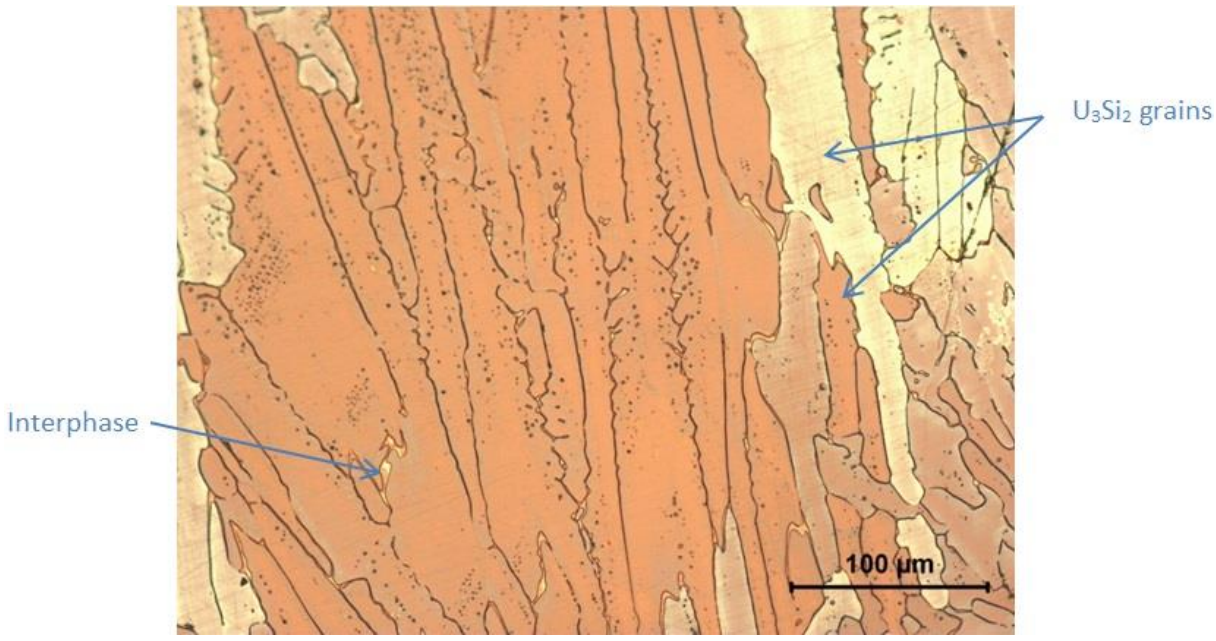

Figure 29: $U_3Si_2^{Alloy\ 06B}$ re-melted x200

The extra addition of silicon for $U_3Si_2^{Alloy\ 06B}$ re-melted seemed to have enabled the composition in the interphases to shift more closely to the ration 40 mol% of Si/60mol% for U. More U_3Si_2 was formed, reducing the quantity of the bright phase.

The grains have a lamellar shape in Figure 29: they grow from the coldest spot and then build up progressively. Here the grains most certainly have grown from the copper holder, which is water-cooled, going towards the centre of the sample.

For the last alloy produced, $U_3Si_2^{Alloy\ 10B}$, the total mass of material was decreased compared to the previous ones. The reduction of the mass led to a better homogenization of the sample during the arc-melting, bigger grains, and a lower amount of the bright phase as shown in Figure 30.

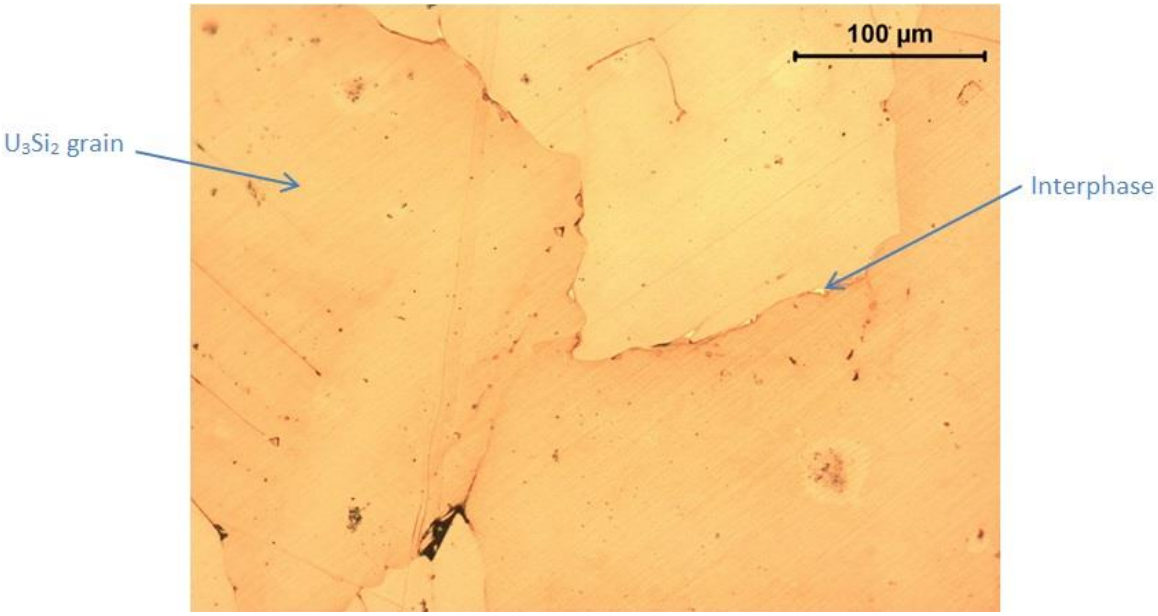

Figure 30: $U_3Si_2^{Alloy10B}$ x200

Figure 31 shows a SEM/EDS analysis used to identify the bright phase common to all the alloys. Table 5 summarizes the EDS results. The data however only gives the general proportion of the elements present in the sample.

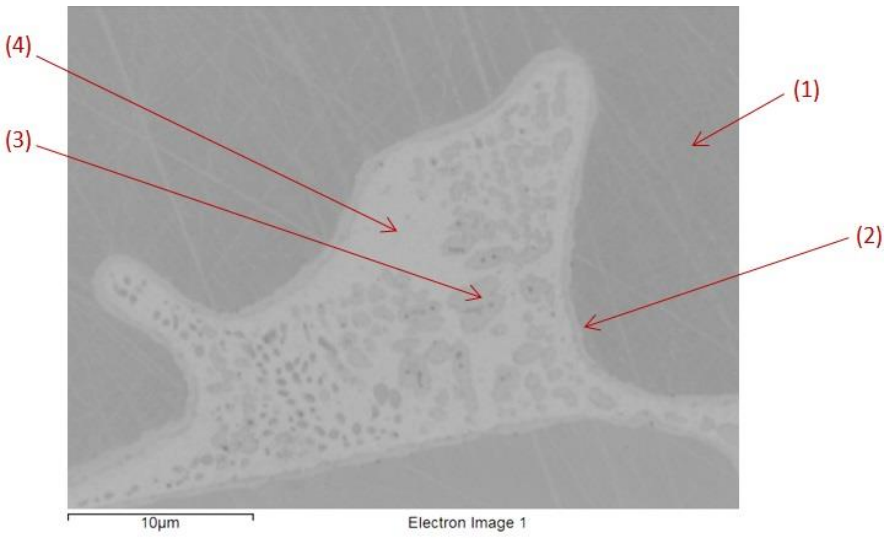

Figure 31: BSE image of $U_3Si_2^{Alloy\ 10A}$ inclusion

Table 5: EDS measurements of $U_3Si_2^{Alloy\ 10A}$ inclusion

Element (mol%)	(1)	(2)	(3)	(4)
Si	47	38	28	0
U	53	62	72	100
Most likely compound	U_3Si_2	U_3Si_2	U_3Si	U

The bright inclusions observed by LOM were found to be a mix of pure uranium and U_3Si. The pure uranium inclusions indicate that the sample is not at thermodynamic equilibrium. At thermodynamic equilibrium, U_3Si_2 can only co-exist with U_3Si or USi, as suggested by the phase diagram. To reach thermodynamic equilibrium, the alloys could have been annealed.

These inclusions are in reality unreacted U_3Si. Although the eutectic reaction of $3U + U_3Si_2 \rightarrow 2\ U_3Si$ is activated from 800°C, the reaction is slow and homogeneity is difficult to obtain. Because of this sluggishness, as-cast alloys around the composition of U_3Si consist essentially of unreacted uranium and U_3Si_2[55].

The presence of pure uranium and U_3Si inclusions in the interphase can explain the high density obtained, since pure uranium has a density of 19.1 g/cm^3 and U_3Si of 15.4 g/cm^3.

All the inclusions observed by EDS for each alloy showed the presence of pure uranium.

Re-melting the $U_3Si_2^{Alloy\ 06B}$ alloy did not prevent the formation of these inclusions, as can be seen in Figure 32 and Table 6.

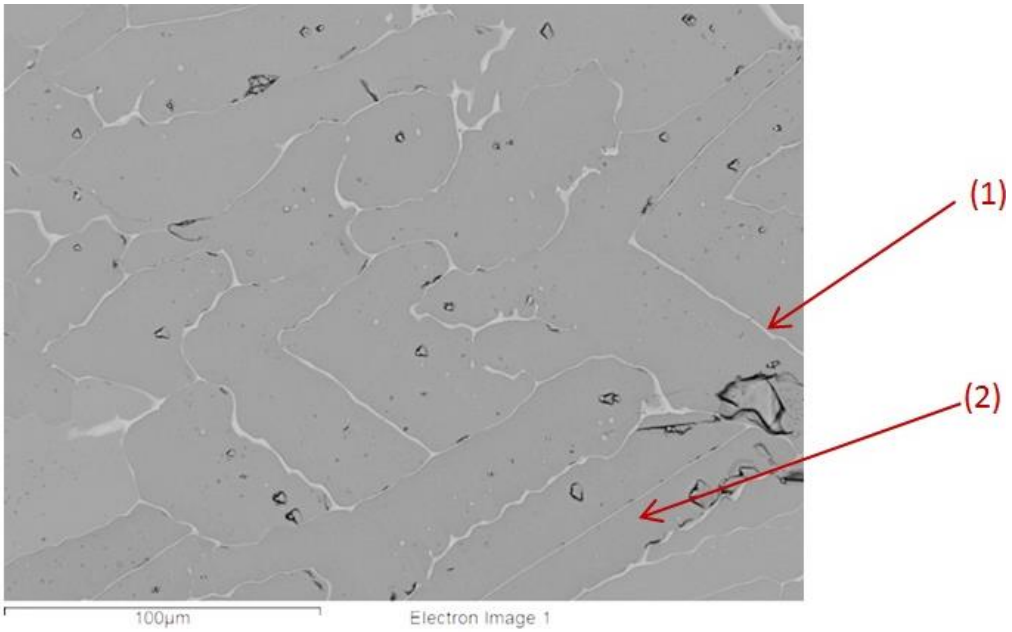

Figure 32: BSE image of $U_3Si_2^{Alloy\ 06B}$ re-melted

Table 6: EDS measurements of $U_3Si_2^{Alloy\ 06B}$ re-melted

Element (mol%)	(1)	(2)
Si	5	45
U	95	55
Most likely compound	U	U_3Si_2

Decreasing the total mass of the alloy, as it was done for $U_3Si_2^{Alloy\ 10B}$, did not prevent the formation of these inclusions either, but the formation of U_3Si_2 inside of the uranium inclusions was noticed in Figure 33 and Table 7.

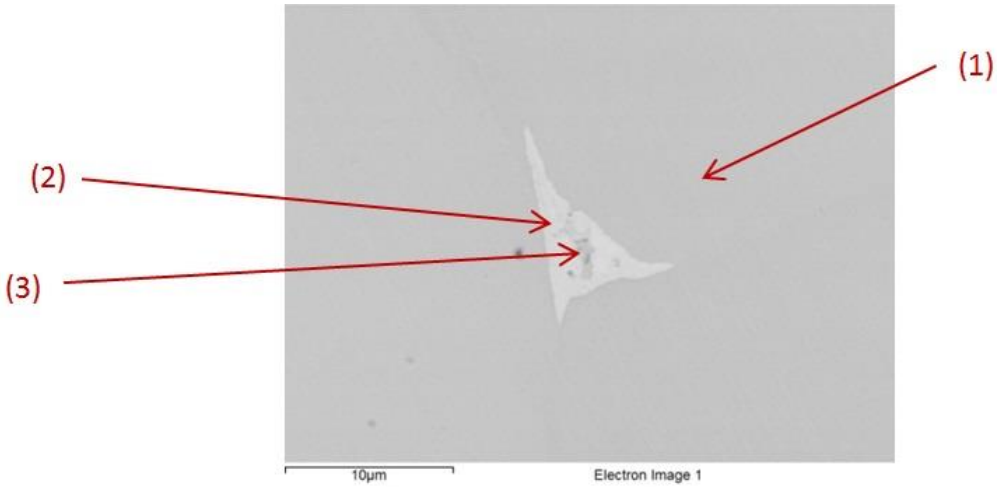

Figure 33: BSE image of $U_3Si_2^{Alloy\ 10B}$ inclusion

Table 7: EDS measurements of $U_3Si_2^{Alloy\ 10B}$ inclusion

Element (mol%)	(1)	(2)	(3)
Si	44	0	36
U	56	100	64
Most likely compound	U_3Si_2	U	U_3Si_2

5.1.2 Powder

After arc-melting, the alloys were milled all together to produce a fluffy powder. The alloys were cut in two and milled in an automated milling machine. The total amount of powder collected was 43g.

- Morphology of the powder

The milled powder was characterized with secondary electron microscopy. The results shown in Figure 34 and Figure 35 highlight a very heterogeneous distribution of particles.

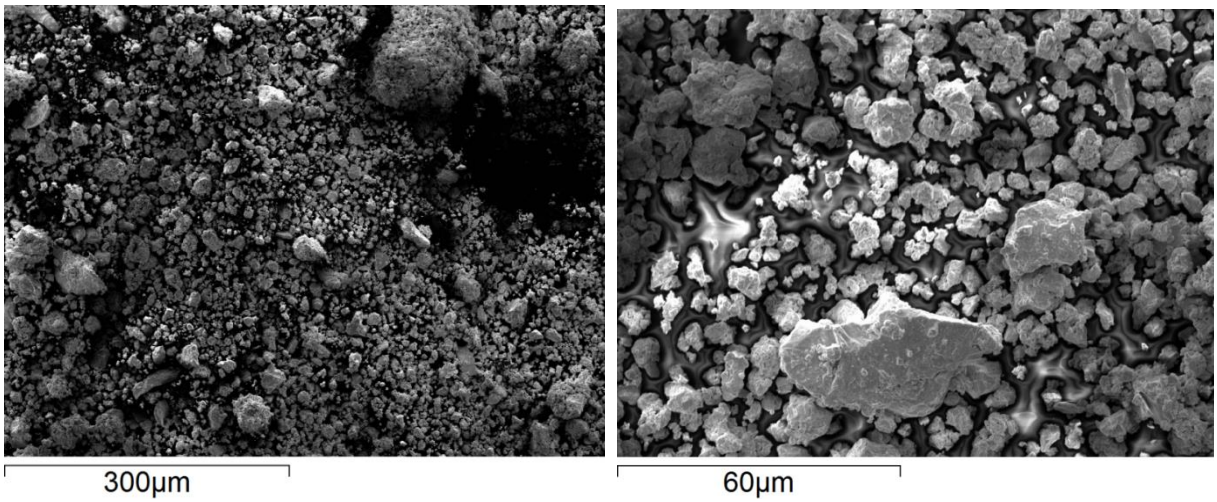

Figure 34: SEM images of the powder using SE

The size of a particle could range from 50 µm to less than 1 µm, as seen in Figure 34 and Figure 35.

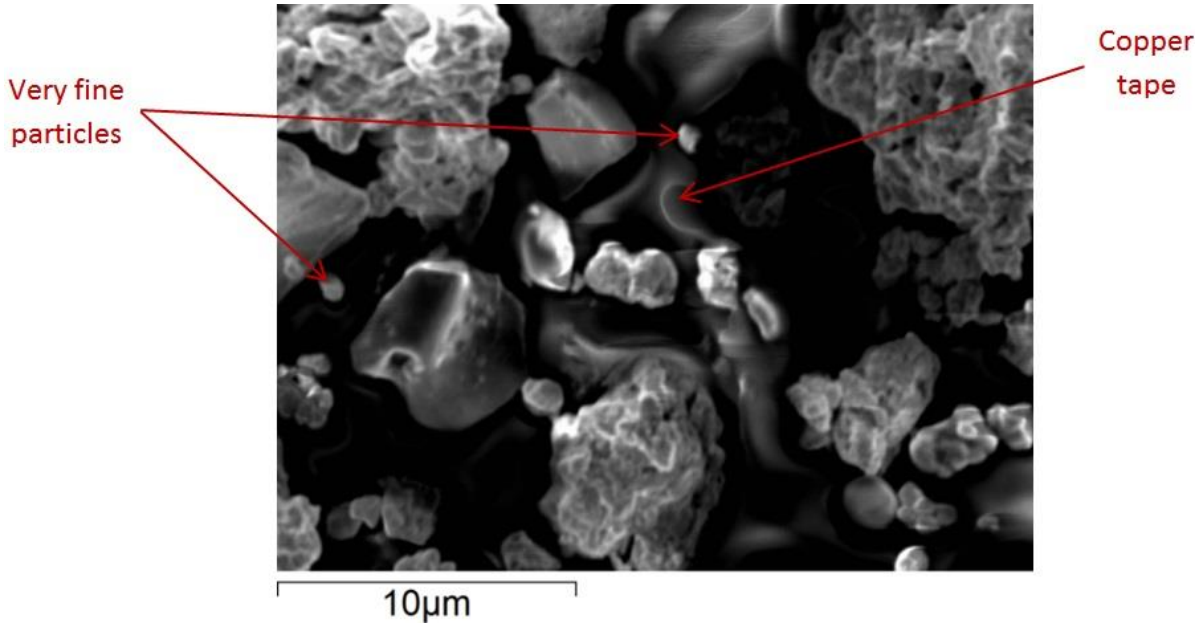

Figure 35: SEM image of fine particles of powder using SE

Some of the particles even turned out to be an agglomerate of finer particles, as demonstrated in Figure 36.

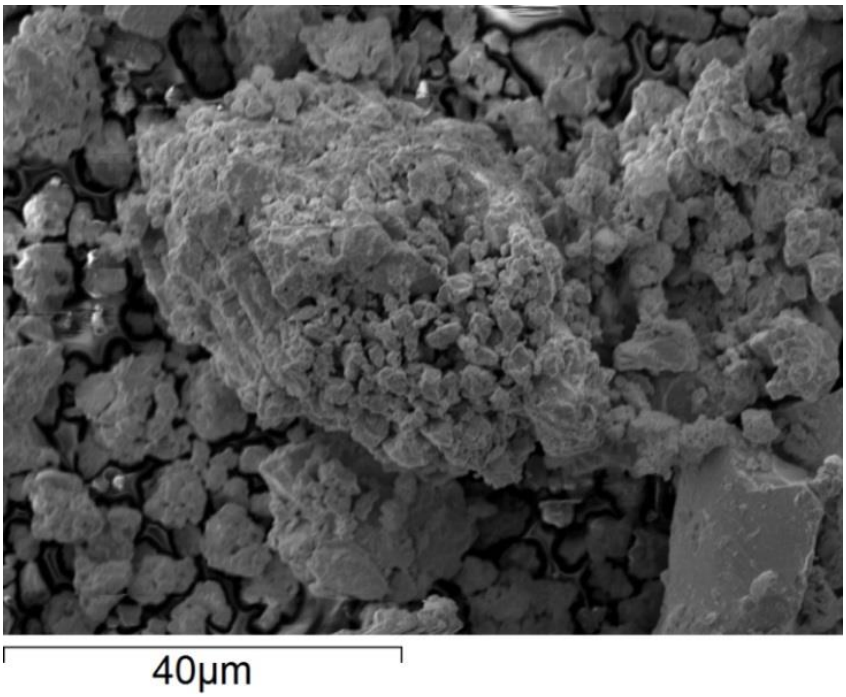

Figure 36: SEM image of an agglomerate of particles using SE

The features of the U_3Si_2 powder was inferred to have an impact on the final microstructure of the sintered pellets. They are also important to explain the reactivity observed in the chemical experiments detailed in section 5.4.

- ### Identification of U_3Si_2

The powder was analysed by XRD and U_3Si_2 with the space group P4/mbm could be identified as demonstrated in Figure 37. Rietveld refinement turned out to be difficult due to the importance of the noise created by the highly-deformed structure in the as-milled condition. However, the lattice parameters obtained were a=7.337Å and c=3.889Å, against a=7.410Å and c=3.913Å in literature[56]. No clear second phase could be identified, meaning that the uranium and U_3Si inclusions observed in the alloys are below detection.

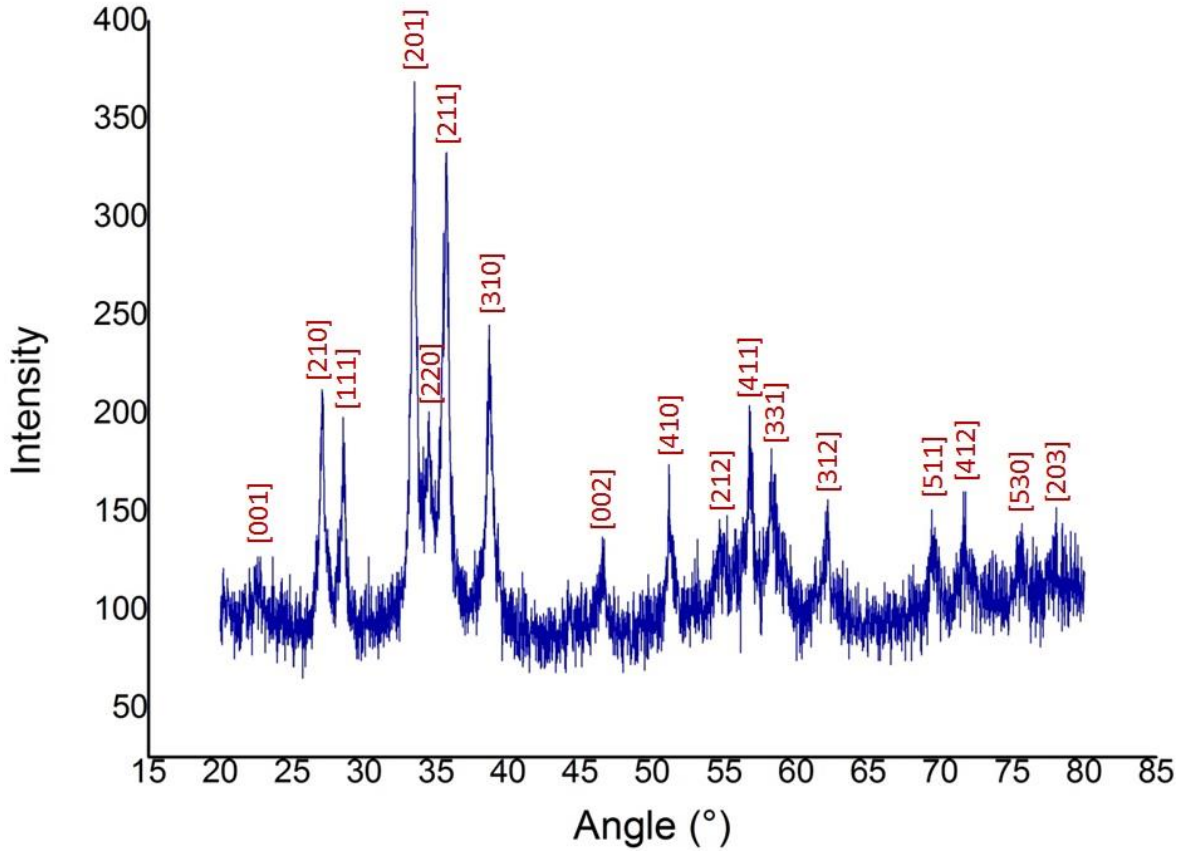

Figure 37: XRD graph of the as-milled U_3Si_2 powder with the peak identification (in red)

The peaks tend to be broad, since the powder has a very inhomogeneous distribution. Peak broadening happens for particles with a size around 0.1 µm. For particles of 40 µm or more, less diffraction occurs, meaning that less diffracted beams will be collected by the detector[57]. This means that only a certain range of particle sizes contribute to the X-ray diffraction spectrum. The full width at half maximum (FWHM) is also determined by residual lattice strain in the grains, that comes here from the stress induced by the machine milling. Lattice strain modifies the interatomic distances[57] as demonstrated in Figure 38.

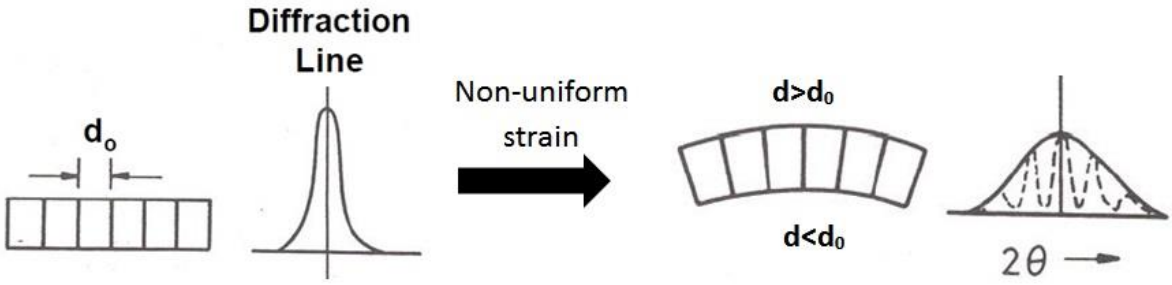

Figure 38: Illustration of the peak broadening due to non-uniform strain

- Oxygen Level Analysis

In the proposed fabrication route, the milling process is a critical step to meet purity requirements for nuclear fuel application. Therefore, immediately after the powder fabrication, a

small mass of U_3Si_2 powder was taken for oxygen analysis. It was measured 1500ppm of oxygen, which means that oxygen represents 1.4 at% of the powder; uranium is present at 59.1 at% and Si at 39.6 at%. It is worth to mention that the presence of oxygen can affect the density measurements of the pellets that are reported.

Considering that the oxygen was all captured by uranium atoms, the sample would be a mix of UO_2, U_3Si_2 and amorphous Si. The resulting density is described in Table 8.

Table 8: Density in case oxygen is captured by uranium

Compounds	At%	Wt%	Resulting density (g/cm3)
UO_2	3.35	1.3	12.14
U_3Si_2	93.3	98.6	
Si	3.35	0.1	

If the oxygen were to combine only with silicon, it could form either silicon monoxide, SiO, or silica, SiO_2 (see Table 9).

Table 9: Densities in case oxygen is captured by silicon

Compounds	At%	Wt%	Resulting density (g/cm3)
SiO	6.3	0.4	12.09
U_3Si_2	85.7	96.8	
U	8	2.8	

Compounds	At%	Wt%	Resulting density (g/cm3)
SiO_2	3.35	0.3	12.12
U_3Si_2	93.3	98.6	
U	3.35	1.1	

The expected density of a fully dense pellet should range between 12.09 and 12.14.

In the previous XRD, Figure 37, no UO_2 peak could be detected, due to a combination of volume fraction and of the importance of the noise.

5.1.3 Pellet fabrication

The produced powder was sintered using a Spark Plasma Sintering (SPS). As described earlier, this technique is very sensitive to the geometry of the die used. As the present work is the first in literature to apply SPS to U_3Si_2 pellets fabrication, it was decided to keep the geometry of the die constant for all the manufactured samples. The diameter chosen was 10 mm. The pellets were heated until a pre-set holding temperature, the length of which varied between runs. The force applied was kept constant at 3.9 kN, which means a pressure of 50 MPa.

- Optimisation of the sintering profile

Table 10 shows the sintering profiles used, the final densities and the integrity of the pellets manufactured in the present work. Several pellets were prepared and for each temperature profile, the heating and the cooling rate were kept the same, except for $U_3Si_{2\ 6}^{1300}$. The pellets are named using the following pattern: $U_3Si_2\ ^{\text{Temperature (°C)}}_{\text{Holding time (min)}}$.

Table 10: Description of the conditions for the sintering of the pellets

Pellet name	Mass of powder	Heating/Cooling rate	Sintering temperature	Holding Time	Density (%TD U_3Si_2)	Pellet cracked
$U_3Si_{2\ 3}^{1000}$	3.47g	400°C-600°C: 100°C/min 600°C-1000°C: 50°C/min	1000°C	3 min	95	Yes
$U_3Si_{2\ 6}^{1200}$	2.6g	100°C/min	1200°C	6 min	97	No
$U_3Si_{2\ 15}^{1200}$	2.6g	100°C/min	1200°C	15 min	99	Yes
$U_3Si_{2\ 6}^{1300}$	3g	Heating: 400°C-1200°C: 100°C/min 1200°C-1300°C: 50°C/min Cooling: 1300°C-400°C: 100°C/min	1300°C	6 min	99.8	No

The mass was decreased after $U_3Si_{2\ 3}^{1000}$ to help the sintering and because the geometry was assumed to be at the origin of the cracking.

A sintering temperature of 1000°C showed to be too low for sintering a U_3Si_2 pellet, as demonstrated in Figure 39. At 1200°C and above, the sintering of the material was observed.

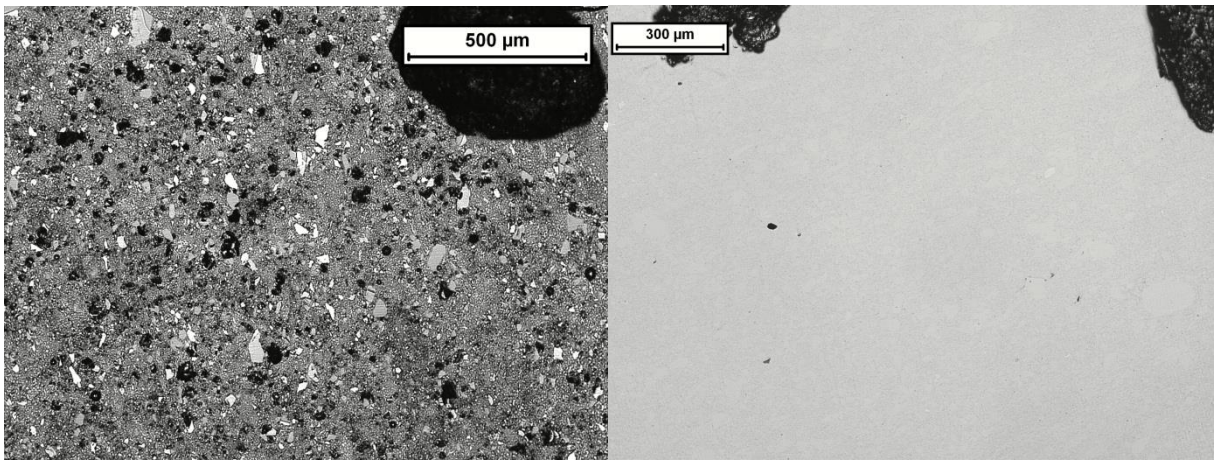

Figure 39: LOM image of $U_3Si_{2\ 3}^{1000}$ x50 (left) and of $U_3Si_{2\ 6}^{1300}$ (right) x50

The pellet sintered at 1000°C was only compact powder. The grains still had very sharp edges, characteristic of the powders produced during the milling process. When sintering starts to occur, the grains tend to minimize their surface area, converging towards a circular shape. In the case of 1000°C, the temperature was not high enough to enable diffusion and to start creating grain boundaries.

For temperatures from 1200°C and more, a sintered pellet with a density in the desired range for fuel application could be produced. The desired density was achieved without the incorporation of additives to the powder, as in the methodology employed by Nelson et al[15], but with much lower sintering times. The presence of additives can favour the presence of open pores in the final microstructure. As described thereafter, the application of SPS lead to a unique microstructure for U_3Si_2 pellets.

- ## Microstructure: pores and inclusions

Each manufactured pellet was subjected to microstructure analysis using LOM and SEM. The high-density pellets – for a sintering at 1200°C and above – presented an interesting microstructure (Figure 40). The presence of closed pores could be put in evidence, as seen in Figure 41.

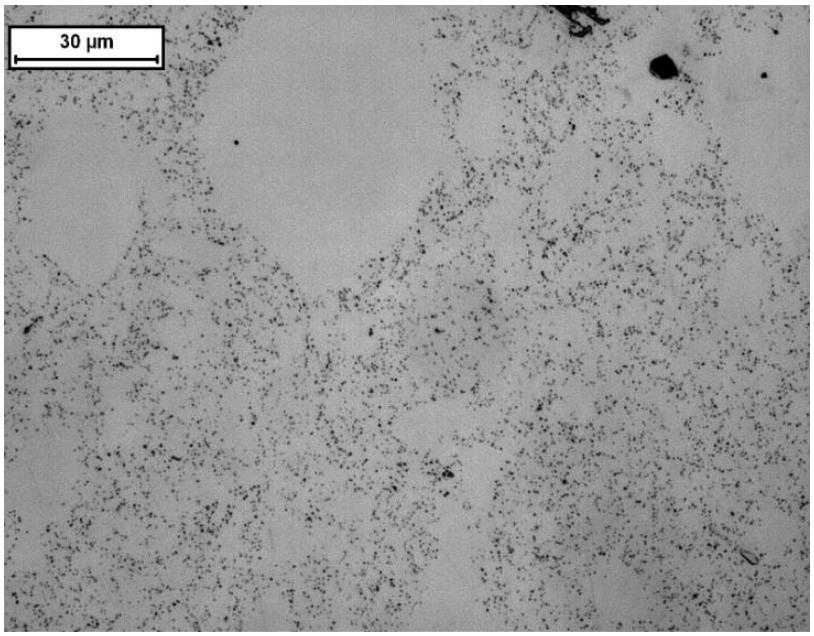

Figure 40: LOM image of U_3Si_2 6 1200 x500 polished using colloidal silica as the final polishing step

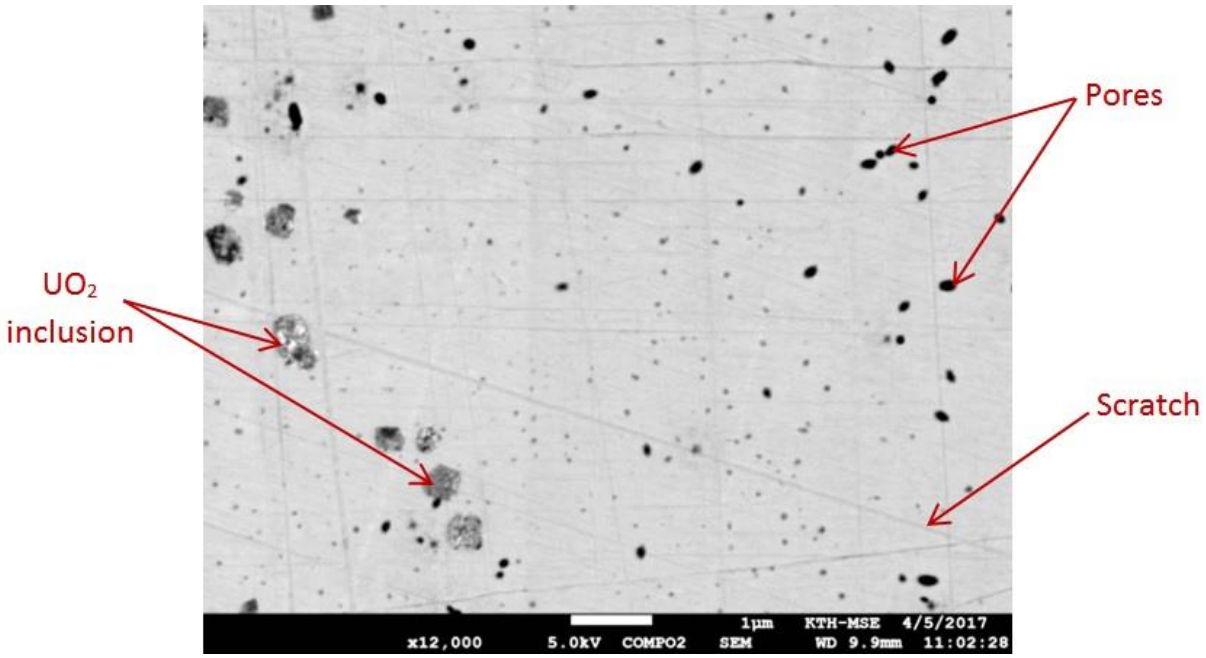

Figure 41: U_3Si_2 6 1300 observed with BSE, not polished in the final step with colloidal silica

The SEM revealed the presence of UO_2 inclusions (Figure 41). The existence of UO_2 inclusions are consistent with the oxygen level measured in the powder.

The presence of scratches in the matrix in Figure 41 comes from the fact that it was difficult to find the right polishing for U_3Si_2 as a pellet. A wrong polishing procedure could lead to close the pores with material or make them bigger. When inclusions are present, a bad polishing can also lead to pull-outs, cavities created after grains or particles are torn out. It happened for previous polishing, especially when colloidal silica was used in the final step of polishing, as demonstrated in Figure 42.

On the left image of Figure 42, particles of silica are trapped in the pores. When using BSE, which penetrate deeper, the matrix appears with holes. However, no oxide inclusions have been identified in this sample, which leads to think that they were pulled-out by the polishing. Due to polishing problems, it was therefore difficult to investigate more thoroughly the influence of the different sintering profile on the size of the pores.

Since the analysis of the pores area using Figure 40 was not consistent with the density measurements, it was assumed that the black dots observed in Figure 40 may reflect the combination of uranium oxide inclusions and pores.

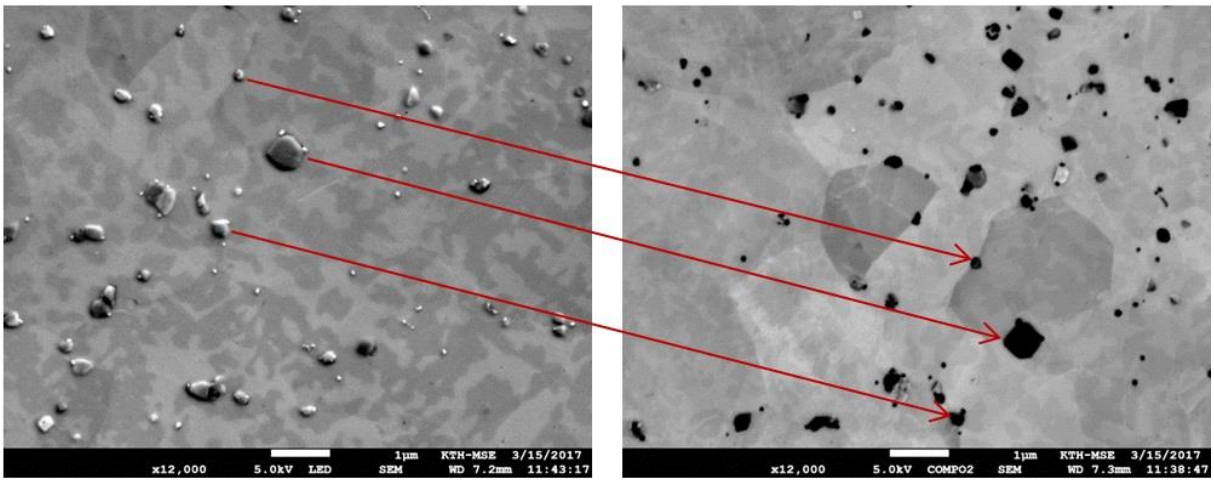

Figure 42: U_3Si_2 $^{1200}_{6}$ polished with colloidal silica as a final step, observed with SE (left) and BSE (right)

Closed nano-pores are a desirable microstructure for a fuel. It enables the storage of the gaseous fission products in the fuel pellet, without permitting them to leave the fuel through a network of open pores. The fission products remain trapped in the fuel, which facilitates the geological storage and the handling of the spent fuel. Having pores such as the ones observed in Figure 41, is not common for a uranium fuel. Previous work on sintering uranium nitride powder by Spark Plasma Sintering showed different microstructure and the absence of nano-pores, as demonstrated in Figure 43 [32].

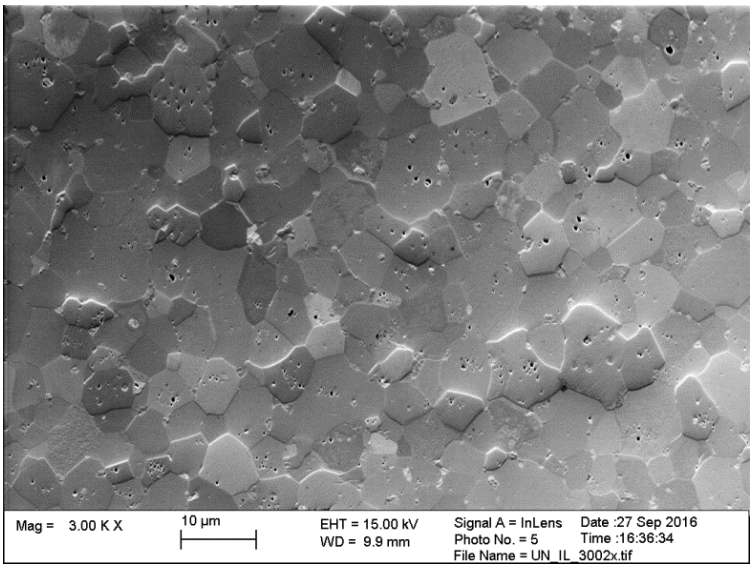

Figure 43: UN pellet sintered by SPS observed by SEM using SE

In this case, pores are present in UN pellets as well but they are larger. They can be present both within the grains (intragranular) and in the grains boundary (intergranular), as it is possible to see in Figure 43.

The existence of a unique nano-pore structure created in the U_3Si_2 samples produced in this work can likely be attributed to the very heterogeneous distribution of the powder. For uranium nitride, the powder is synthesized chemically and therefore has a much more regular particles size and a more homogeneous distribution. The pores could also come from a feature of the material itself.

The samples $U_3Si_{2\ 6}^{1200}$, $U_3Si_{2\ 15}^{1200}$, $U_3Si_{2\ 6}^{1300}$ were etched to reveal the grain structure and analysed with optical microscopy. By comparing Figure 44 to 47, it appeared by a qualitative analysis that the grains of $U_3Si_{2\ 6}^{1300}$, sintered at 1300°C instead of 1200°C for $U_3Si_{2\ 6}^{1200}$ and $U_3Si_{2\ 15}^{1200}$, were bigger. It was assumed that temperature had an influence on grain growth. Nevertheless, no clear difference could be spotted between $U_3Si_{2\ 6}^{1200}$ and $U_3Si_{2\ 15}^{1200}$.

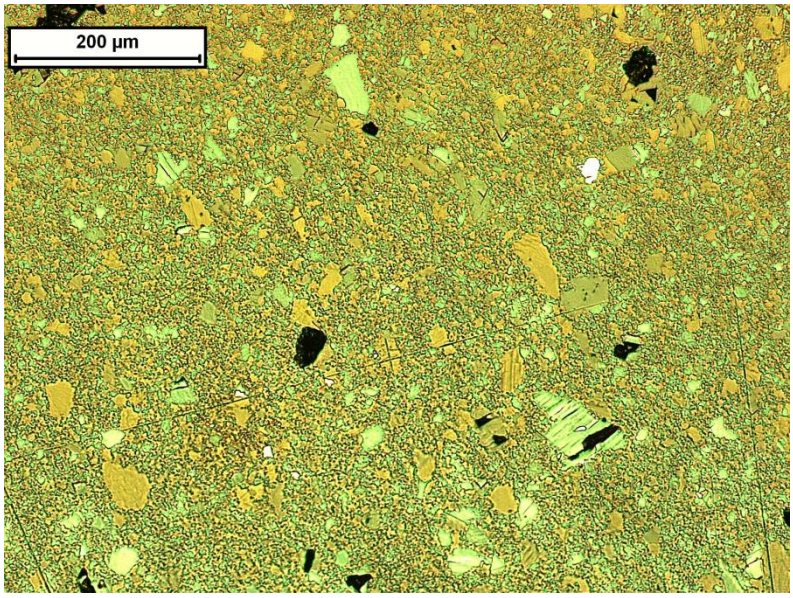

Figure 44: $U_3Si_{2\ 6}^{1200}$ etched observed with LOM x100 with color saturation

Figure 45: $U_3Si_{2\ 15}^{1200}$ etched observed with LOM x100 and with color saturation

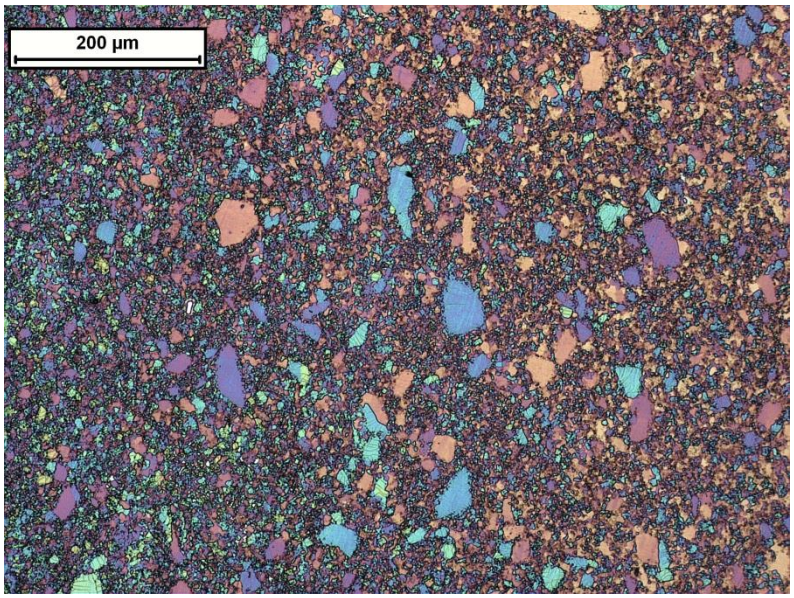

Figure 46: $U_3Si_{2\ 6}^{1300}$ etched observed with LOM x100 and with color saturation

The different colors produced by the etching reflect different grains orientations as reported here[47].

All of the pellets revealed an inhomogeneity in the grains size: from large grains of 30 µm or more, until very small ones, of 1 µm or less, as it is visible in Figure 47. This observation is coherent with the distribution of particles in the powder. It means that, with SPS, the size of the grains could be controlled by controlling the size of the milled particles.

Some very bright phases were observed in each sample as well, as demonstrated in Figure 47. It could be U_3Si or unreacted uranium, as it was observed in the alloys.

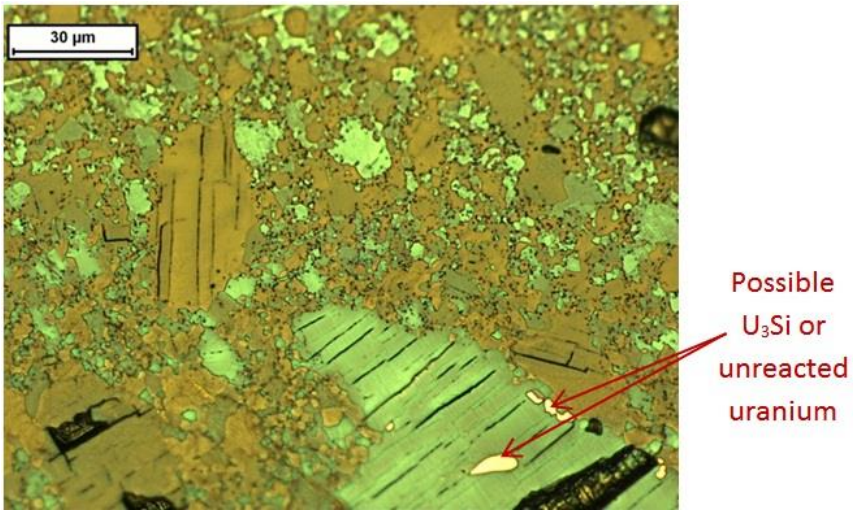

Figure 47: $U_3Si_{2\ 6}^{1200}$ etched observed with LOM x500 and color saturation

These areas were subject to analysis with SEM and EDS. For the etched sample, no difference in composition could be discerned as shown in Figure 48 and Table 11.

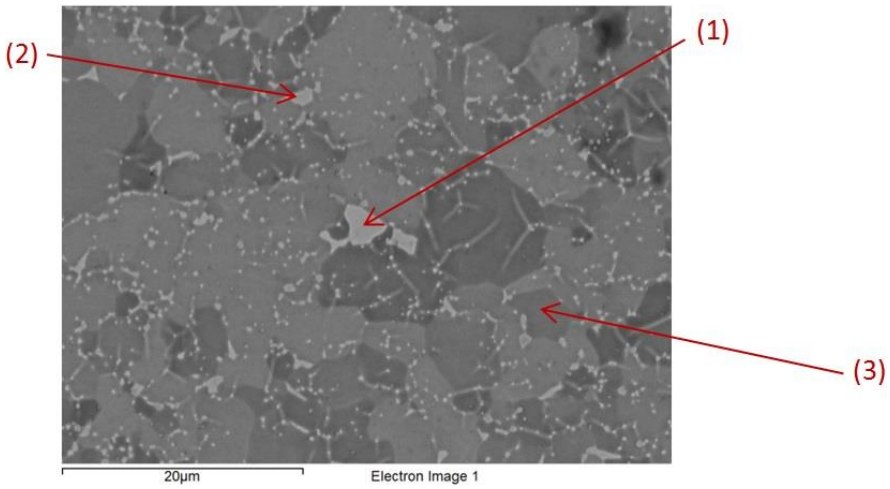

Figure 48: BSE image of etched $U_3Si_{2\ 6}^{1300}$

Table 11: EDS results for $U_3Si_{2\ 6}^{1300}$

Element (at.%)	(1)	(2)	(3)
Si	47	48	56
U	53	52	44

Since uranium and U_3Si have a poorer behaviour regarding etching than U_3Si_2, they should be chemically more attacked than U_3Si_2. If they had been present on the sample, they would have appeared as lighter phases than U_3Si_2, which means dark spots with BSE. Nothing as such was observed. The very bright spots seen in Figure 47 can come from the fact that the U_3Si_2 grains are chemically attacked at very different speeds, since the crystallographic structure of U_3Si_2 is

anisotropic. Depending on the plane orientation of the U_3Si_2 lattice, the structure will be attacked very differently.

- XRD

To determine the final crystallography lattice present in the pellets, a piece of $U_3Si_{2\ 6}^{1200}$ was cut and gently milled by hand and subjected to XRD analysis. The result is presented in Figure 49. It turned out to have an important contamination with an intense peak at 26.4° coming from the graphite, which contained the powder during SPS. It has been observed during previous experiments that, during the sintering, the graphite foil can be bounded to the surface of the pellet. If this graphite is not removed completely during sample preparation, residual contamination can be detected via XRD. This contamination that was not observed when a cross-section of the pellet was analysed by SEM.

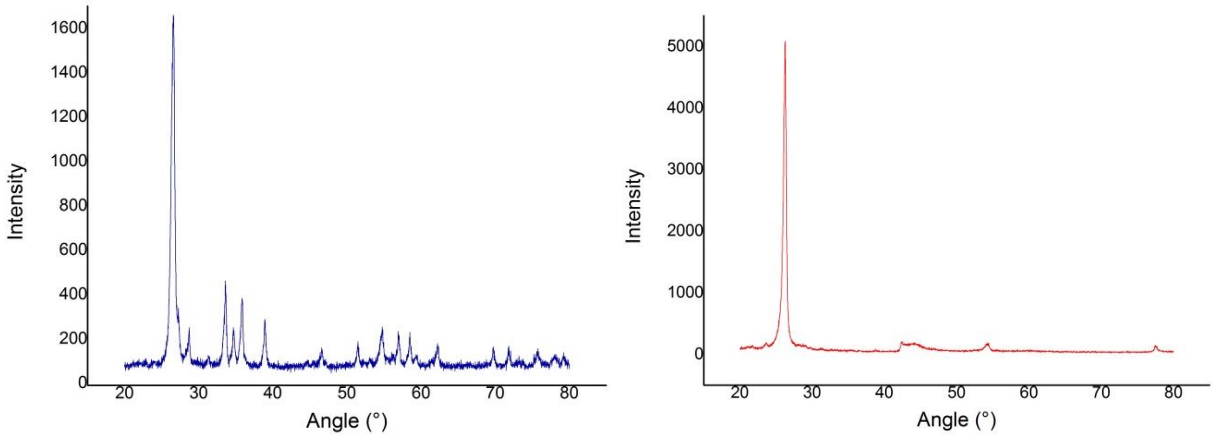

Figure 49: XRD graphs of a piece of $U_3Si_{2\ 6}^{1200}$ hand milled (right) and of graphite (left)

The XRD of $U_3Si_{2\ 6}^{1200}$ was zoomed in for the identification of the peaks as shown in Figure 50.

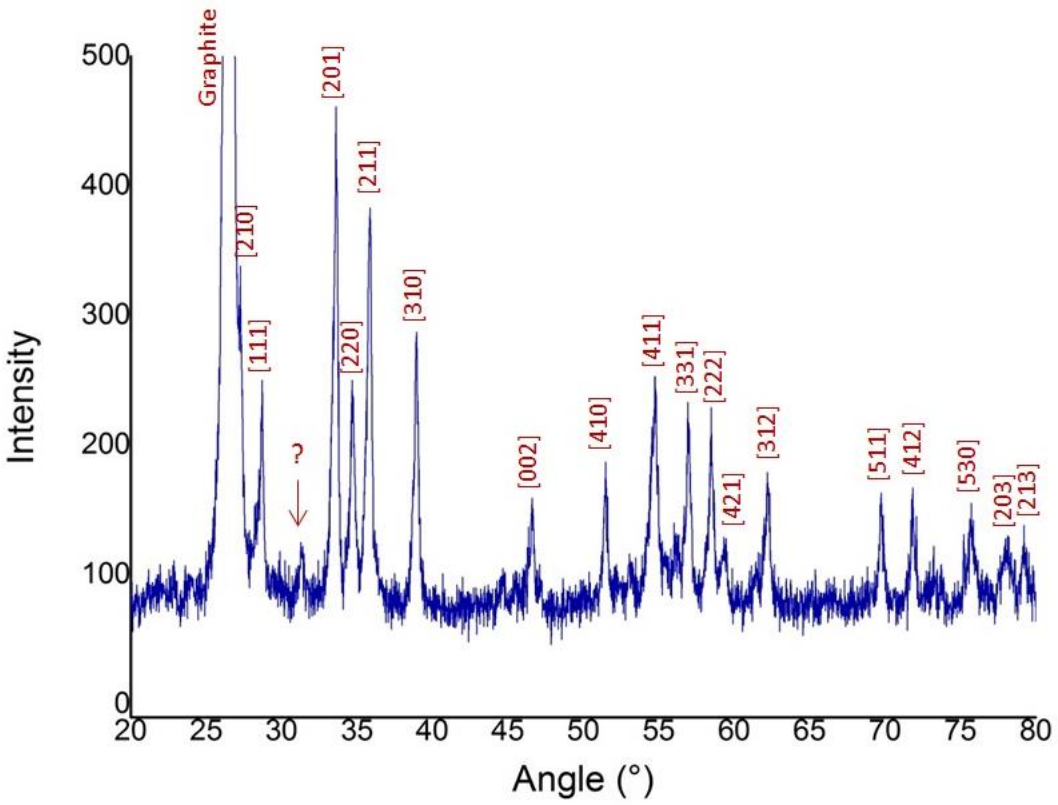

Figure 50: XRD graph of hand-milled $U_3Si_{2\ 6}^{1200}$

The majority presence of U_3Si_2 could be verified. Additionally, an unidentified peak at 31.3° is present. Several standard XRD profiles were tested, such as α-, β- or γ-U, as well as UO_2, U_3O_8 and U_3Si, and the most suitable to meet this extra peak was uranium carbide. During SPS, carbon can interact with uranium to form uranium carbide on the surface of the pellet, causing a contamination. A Rietveld refinement gives around 2wt.% of UC. Here, it is the diffraction coming from the plane [111] that can be seen, the most intense peak of UC XRD. No uranium carbide contamination was spotted in the bulk using SEM, which reflects the presence of this phase only in the surface. No UO_2 peak is visible here either, meaning its amount, estimated at 1.3wt.%, must be under detection limit.

As expected, the sintered U_3Si_2 XRD pattern proved to have more intense and sharper peaks than the milled powder. This observation is in agreement with the concept of thermal elimination of crystallographic defect, increase in crystallite size and reduced stress.

- ## Expansion during sintering

One of the outputs of the SPS machine is the displacement of the punches, i.e. the displacement in the z direction, perpendicular to the radial direction, as a function of time. Using this output, it is possible to monitor the expansion or the contraction of the sample during sintering. In Figure 51, an expected sintering graph is presented. The curve presented here was collected during the SPS sintering of UN pellets[32].

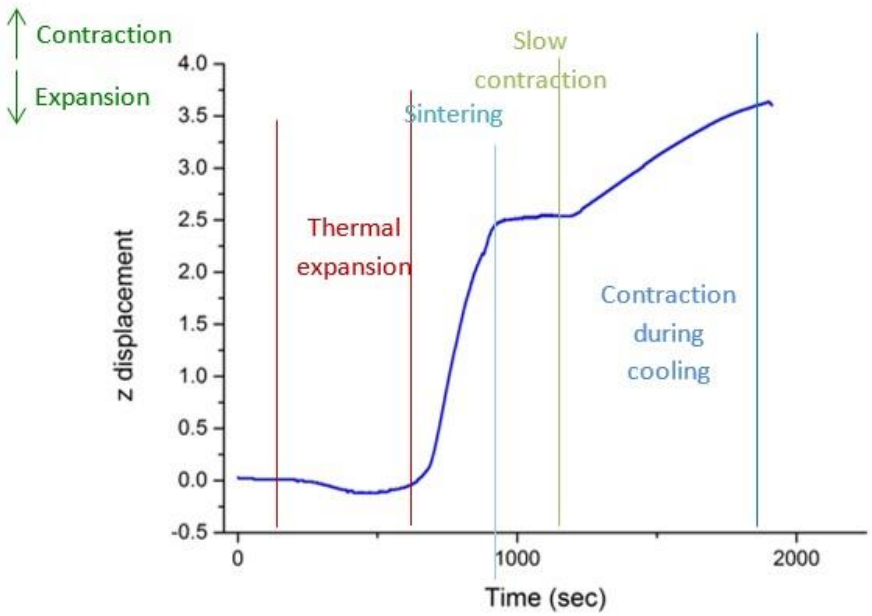

Figure 51: Z displacement vs time of a UN pellet during sintering

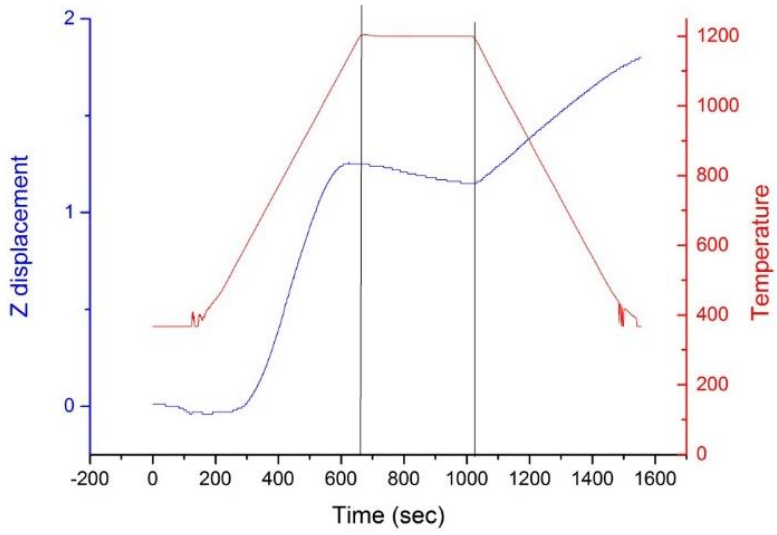

Figure 52: Z displacement vs time of $U_3Si_{2\ 6}^{1200}$

For the UN sintering, the expected behaviour, the thermal expansion and the main part of the sintering happen during the increase in temperature, until the isothermal temperature is reached. Then, during the holding time, a slow contraction happens as the sintering continues slowly. During the cooling time, the material shrinks again.

All the sintering processes of U_3Si_2 performed in this work had a similar behaviour, as represented in Figure 52. Most of the sintering had already occurred when 1200°C was reached. In the case of $U_3Si_{2\ 6}^{1200}$, for instance, the z displacement seems constant when reaching the isotherm at 1200°C. For each of the sintered pellet, a linear expansion happened during the holding time, in opposition to the trend observed for UN. The expansion, linear at the beginning, seems to tend to a constant value of z, as it was observed for $U_3Si_{2\ 15}^{1200}$. For all the different sintering conditions, the expansion rates were calculated and are shown in Table 12.

Table 12: Expansion rates for three of the pellets

Pellet	Sintering	Expansion rate
$U_3Si_{2\ 6}^{1200}$	1200°C (6min)	-3.26 x 10^{-4} z/sec
$U_3Si_{2\ 15}^{1200}$	1200°C (15min)	-3.57 x 10^{-4} z/sec
$U_3Si_{2\ 6}^{1300}$	1300°C (6min)	-3.04 x 10^{-4} z/sec

It was observed that the rates have close values. Literature says that this kind of expansion happens for inorganic compounds formed by the compaction of powder. Most of the sintering shrinkage happens in the intermediate "stages" of thermally driven sintering. Then, the dimensionality of the sample is most sensitive to microstructural factors[58]. This hypothesis tends to be confirmed by another pellet, $U_3Si_2Mo_{\ 6}^{1200}$, described in section 5.2. Molybdenum was added at 1.5 at.% to the U_3Si_2 matrix and, with the same sintering conditions but with different compositions, $U_3Si_{2\ 6}^{1200}$ and $U_3Si_2Mo_{\ 6}^{1200}$ got different expansion rates: -3.26 x 10^{-4} z/sec and -2.49 x 10^{-4} z/sec respectively. It shows that the expansion observed in this work is connected with microstructure features.

The expansion observed with the produced pellets could therefore be explained on a microstructural level, such as intern reorganization, pore coalescence or by grain boundary relaxations originating from rapid grain growth[59]. An expansion due alone to pore coalescence would rather have a logarithmic dependence of time: pores tends to move more and more slowly when they are growing big and therefore they coalesce less and less. The proportional dependence of time may therefore come from a combination of factors, or from a mechanism proportional to time.

Homogenization is amongst the most likely factors to contribute to the expansion. The inclusions observed in the alloys, U and U_3Si, have a higher density than U_3Si_2. Since these inclusions were not observed in the pellets, the composition must have been homogenized during the sintering, forming more U_3Si_2 with a lower density, explaining the expansion.

The methodology described in this section proved to be efficient to form highly dense pellets at low temperature and with low sintering times. It proved to form pellets with a unique microstructure, with nano-metric closed pores, a microstructure not achieved by the normal sintering route, where only open pores were formed. The sintering process showed the ability to homogenise the sample, to form a uniform U_3Si_2 matrix, despite the inclusions observed in the as-cast alloys.

5.2 DOPING WITH MOLYBDENUM

Molybdenum is one of the main fission products produced during irradiation. Present in 1.5at% for a burn-up of 119.55 MWd/kg(U), it is amongst the most abundant solid fission products to be generated in the fuel. It is the third most important contribution after Xe (1.9 at%) and Pu (2.7 at%)[60]. It is therefore important to investigate whether it will be soluble in U_3Si_2 or whether it will form a ternary phase that would disrupt the fuel stoichiometry.

Two ways of proceeding were considered: either mix pure uranium, silicon and molybdenum together via arc-melting or to integrate the molybdenum in an already existing U_3Si_2 matrix. The former had already been done in literature and did not prove to reproduce closely the morphology found in a fuel during burn-up, as explained in section 2.4.

5.2.1 Pellet fabrication

To prepare the doped pellet, named here as $U_3Si_2Mo_6^{1200}$, pure molybdenum was milled in a glovebox with a combination of balls with two different sizes. It was milled with the same program as the one used for U_3Si_2. 0.6wt% of molybdenum was then mixed with U_3Si_2 powder to form 3g of powder in total. In the same way as the U_3Si_2 pellets, the sintering was performed using SPS with a holding temperature of 1200°C for 6min. The heating and the cooling rates were of 100°C/min.

The pellet did not crack and a density of 98.9% was measured, compared to the theoretical density of U_3Si_2.

5.2.2 Formation of a ternary phase

The main reason to study the morphology of doped U_3Si_2 is to try to understand the solid interactions of molybdenum with the U_3Si_2 matrix. Figure 53 shows the morphology of the doped pellet after the sintering process. The as-sintered sample may not represent the thermodynamic equilibrium, but this is not a concern, since a considerable number of phenomena happens out of equilibrium in a reactor.

In literature however, all studies of U-Mo-Si ternary systems are done at equilibrium, therefore a gap on the transitional states exist. Nevertheless, some of the results shown here were reported in literature too.

Observing the morphologies, molybdenum showed the presence of inclusions, as shown in Figure 53.

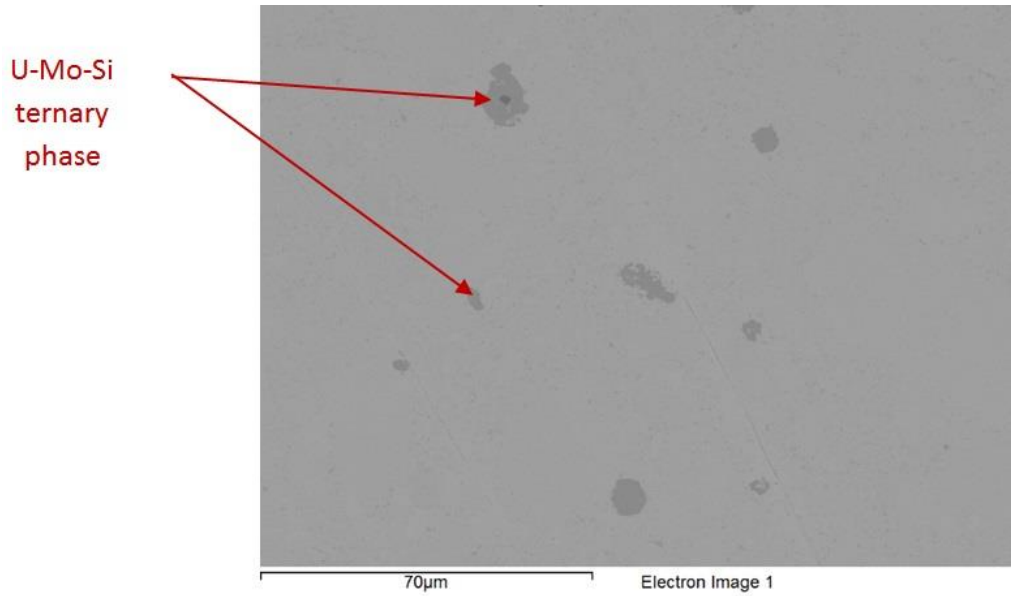

Figure 53: BSE image of $U_3Si_2Mo_6^{1200}$

The result shown in Figure 54 is a SEM/EDS analysis of the sample after etching. It revealed the presence of an interphase that was not visible without etching.

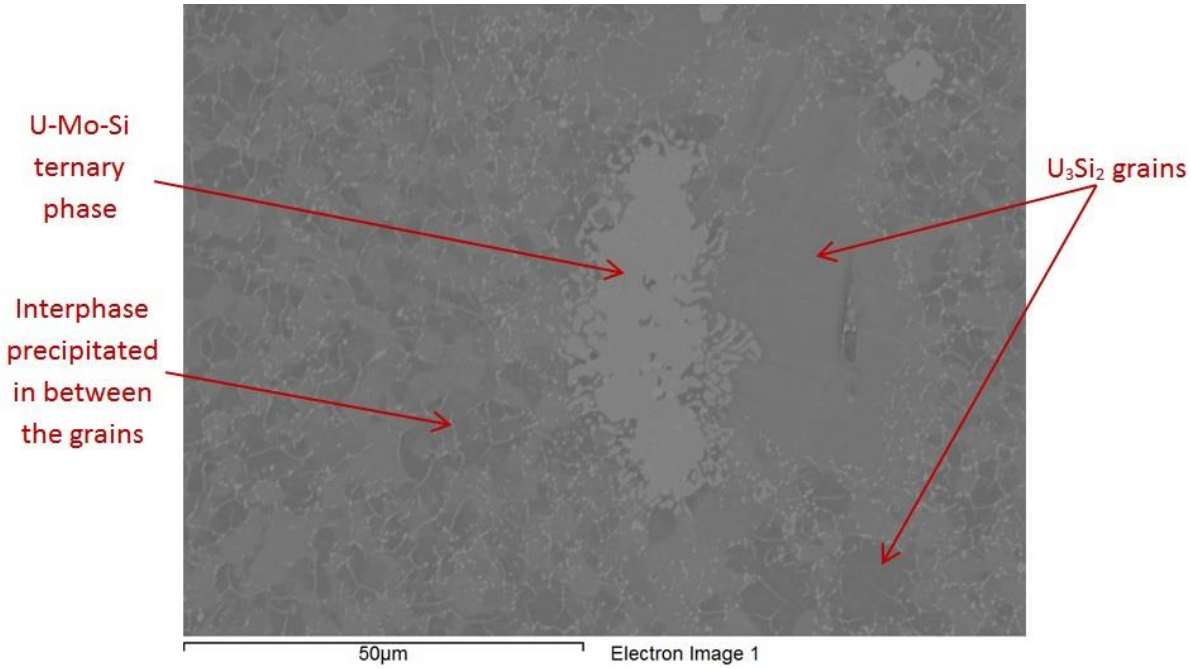

Figure 54: $U_3Si_2Mo_6^{1200}$ etched observed with BSE

The EDS analysis permitted to identify the composition of the ternary phases spotted in the U_3Si_2, the non-etched sample, that are seen in Figure 53. The results of the EDS analyses of the inclusions and of the matrix are shown in Figure 55 and Figure 56.

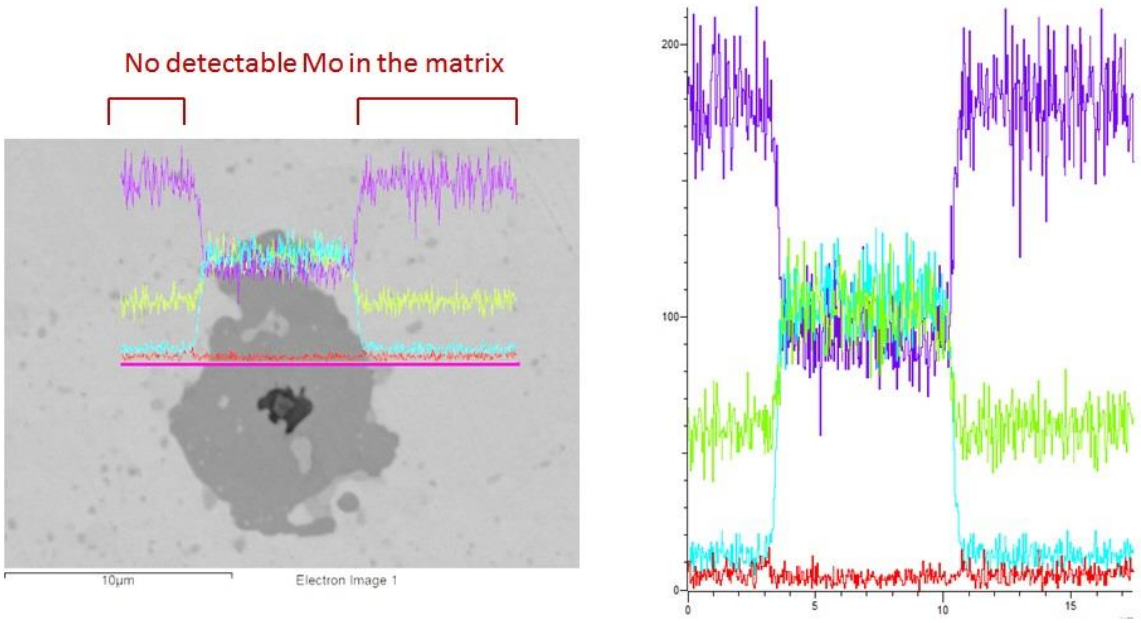

Figure 55: $U_3Si_2Mo_6^{1200}$ image using BSE (left) and corresponding elemental analysis (right) showing uranium (purple), silicon (green), molybdenum (blue) and oxygen (red)

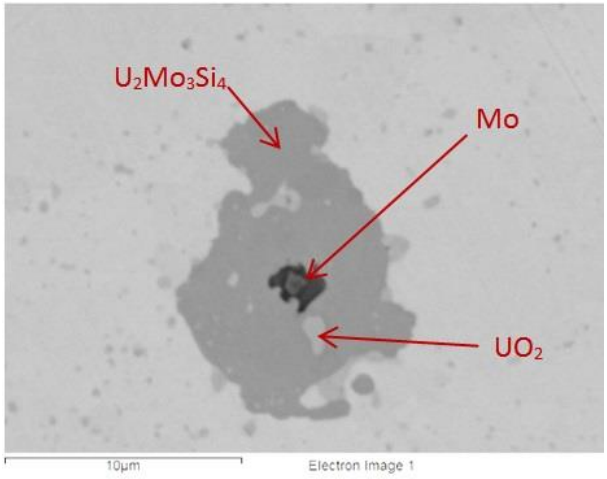

Figure 56: $U_3Si_2Mo_6^{1200}$ observed with BSE

The molybdenum showed no solubility in the U_3Si_2 matrix, as demonstrates Figure 55, a result reported by literature, as explained in section 2.4.

Pure grains of molybdenum reacted to form the ternary phase $U_2Mo_3Si_4$ which was observed throughout the sample. The interaction process was observed even for the large pieces of molybdenum, which demonstrates that the diffusion process can easily pass through distances higher than 10µm. $U_2Mo_3Si_4$ seemed to be the dominant ternary phase, leading to the hypothesis that it is a phase considerably stable, which is coherent with literature. In the sample produced in the present work, it was also possible to observe another ternary phase in a few spots, as demonstrated in Figure 57.

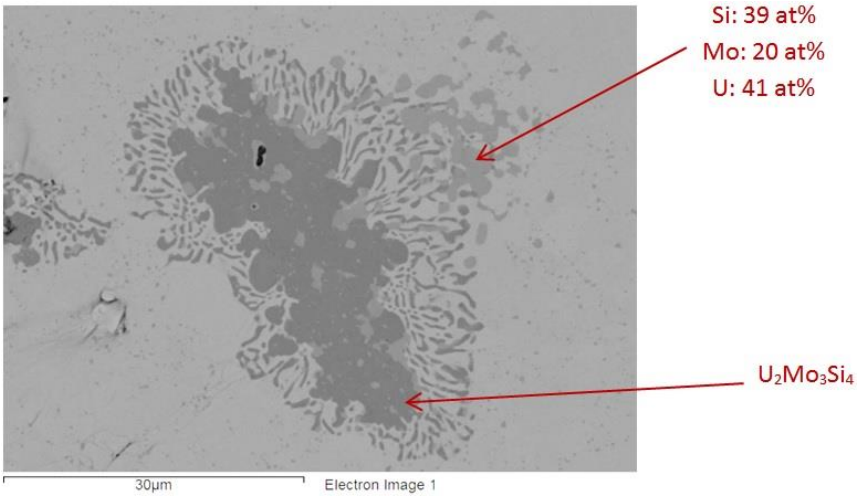

Figure 57: $U_3Si_2Mo_6$ 1200 observed with SEM

As it can be seen on Figure 57, $U_2Mo_3Si_4$ tends to a lamellar structure. It most likely indicates that, once pure molybdenum had reacted with the matrix to form $U_2Mo_3Si_4$, this ternary phase would tend to increase its surface contact with the matrix. To a lesser extent, the phase $U_{41}Mo_{20}Si_{39}$ was spotted only where the lamellar structure could be observed. It suggests that this phase is formed from the reaction of the matrix with $U_2Mo_3Si_4$. The phase $U_{41}Mo_{20}Si_{39}$ is most likely $U_4Mo(Mo_xSi_{1-x})Si_2$, also reported in literature[16].

$U_2Mo_3Si_4$ and $U_4Mo(Mo_xSi_{1-x})Si_2$ are phases poor in uranium compared to U_3Si_2. Therefore, when the matrix is consumed to form a ternary phase with Mo, some uranium is left over. The two possibilities are either the matrix became uranium-doped to accommodate – which is more likely to happen in high temperature as reported here [7] – or that a uranium-rich phase formed. In literature, when Mo was introduced in the melting process, it was reported the formation of γ-(U,Mo), as being in equilibrium with $U_2Mo_3Si_4$ and $U_4Mo(Mo_xSi_{1-x})Si_2$. Literature also reported the formation of U_3Si for the alloy $U_{72}Mo_5Si_{23}$[16].

To investigate deeper the occurrence of additional phases, the sample, $U_3Si_2Mo_6$ 1200, was etched and analysed with SEM/EDS (Figure 58 and Figure 59).

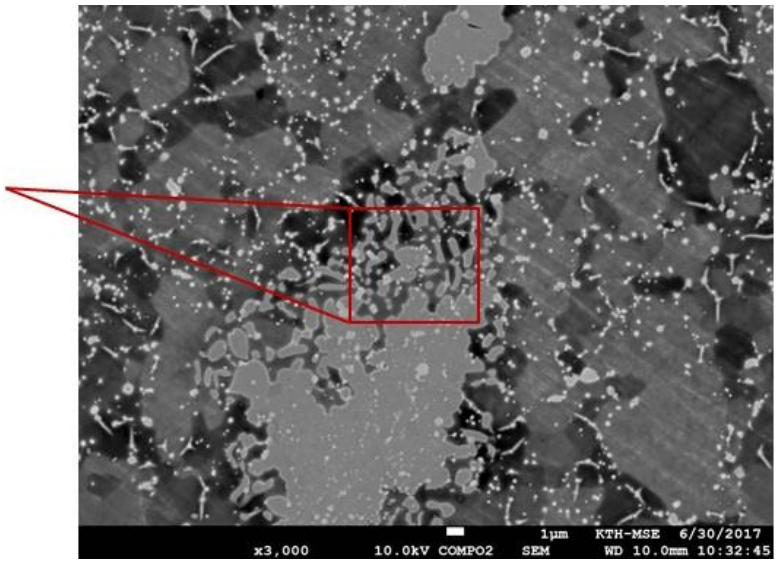

Figure 58: SEM image of $U_3Si_2Mo_6$ 1200 etched using BSE

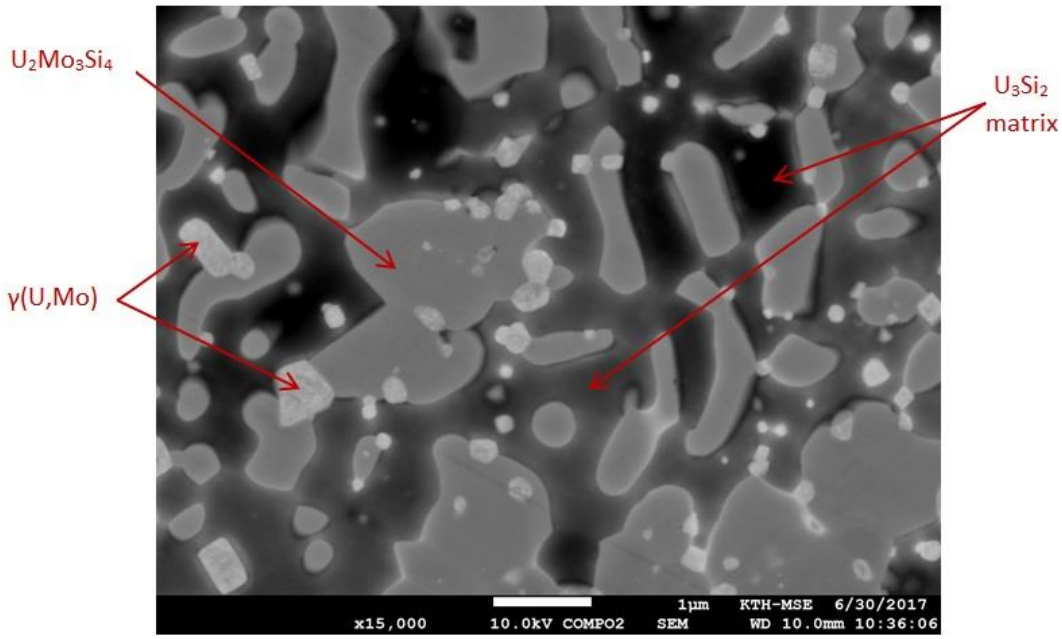

Figure 59: SEM image of $U_3Si_2Mo_6^{1200}$ etched using BSE, zoom on the composition of the lamellar structure

A uranium-rich phase, γ-(U,Mo), was found connected to the formation of the U-Si-Mo ternary phase. It contains here approximately 90wt% of uranium for 10wt% of molybdenum. It means that the formation of $U_2Mo_3Si_4$, by reaction of pure molybdenum with U_3Si_2, also leads to the formation of γ-(U,Mo). γ-U has a bcc structure and is formed at a temperature superior to 750°C. Several transition metals, particularly 4d and 5d elements in Group IV through VIII, form solid solutions with γ-U and can retain this crystallographic structure upon cooling[61]. It has been already produced here[62] a U-10wt%Mo alloy, suggesting that a γ-(U,Mo) phase can be retained here upon cooling.

One can wonder if in a LWR a γ-(U,Mo) phase will really form, since uranium is being consumed to form fission products.

During its life, the fuel swells due to burn-up. It is therefore important for future work to study $U_2Mo_3Si_4$ and $U_4Mo(Mo_xSi_{1-x})Si_2$, to understand their properties and how they would contribute to the swelling of the fuel.

No U_3Si could be spotted anywhere on the sample. The formation of U_3Si due to the burn-up of the fuel would be troublesome since it has poor irradiation behaviour.

None of the other phases reported by the melting process used in literature[16] were observed in the doped sample. This result demonstrates the difference in mechanism of a solid-solid interaction, the dominant interaction in a fuel in service, with a mechanism of liquid-liquid interaction.

The methodology employed, which consisted in sintering by SPS milled U_3Si_2 with milled Mo, seems to be more appropriated to simulate a burn-up structure, rather than the direct melting process. The short sintering time used in SPS provided a way to assess the primary stages of the Mo-U_3Si_2 reaction, which completes a gap in literature.

5.2.3 Assessing thermal stability

In sequence, the doped sample was subject to a heating cycle within a DSC equipment in inert atmosphere. The main purpose was to record any exo/endo thermic reaction that could be associated with phase transformation. The sample was heated at 10°C/min until 1000°C and held for 10min and cooled at 10°C/min. The results are shown in Figure 60.

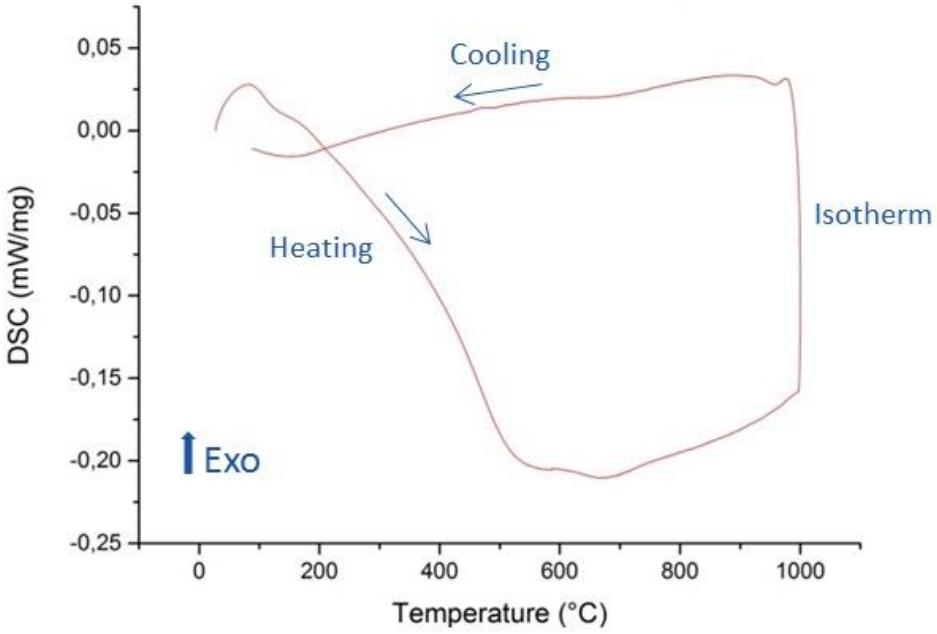

Figure 60: DSC of $U_3Si_2Mo_6^{1200}$ in inert atmosphere

The calorimetric analysis demonstrated the absence of peaks for the thermal cycle applied, which would come from a reaction inside the sample, a reorganisation of the phases. It is therefore assumed that the phases obtained during the sintering process, mainly $U_2Mo_3Si_4$ and $U_4Mo(Mo_xSi_{1-x})Si_2$, have a certain thermal stability. It is however important to mention that a longer heat treatment may be necessary to produce a significant amount of change in the observed phases. However, it is out of scope for this project to assess the long-time reactions, since the purpose is to understand how fast the solid-solid reaction occurs and what are their primary phases.

5.3 OXIDATION BEHAVIOR OF U_3Si_2 IN AIR

5.3.1 Oxidation in air

As described in the introduction, an accident tolerant fuel must have an increased oxidation resistance compared to existing UO_2 fuel. In the present work, to assess this important parameter, a U_3Si_2 as-cast piece of alloy was oxidized in synthetic air using DSC and TG analysis (see Figure 63). To make a comparative study, a piece of UO_2 pellet (provided by Westinghouse) was also submitted to the same heating cycle (see Figure 61 and Figure 62). Around 20mg of sample was heated until 1000°C with a rate of 5 °C/min, the temperature was held for 1h and the sample cooled at 20°C/min.

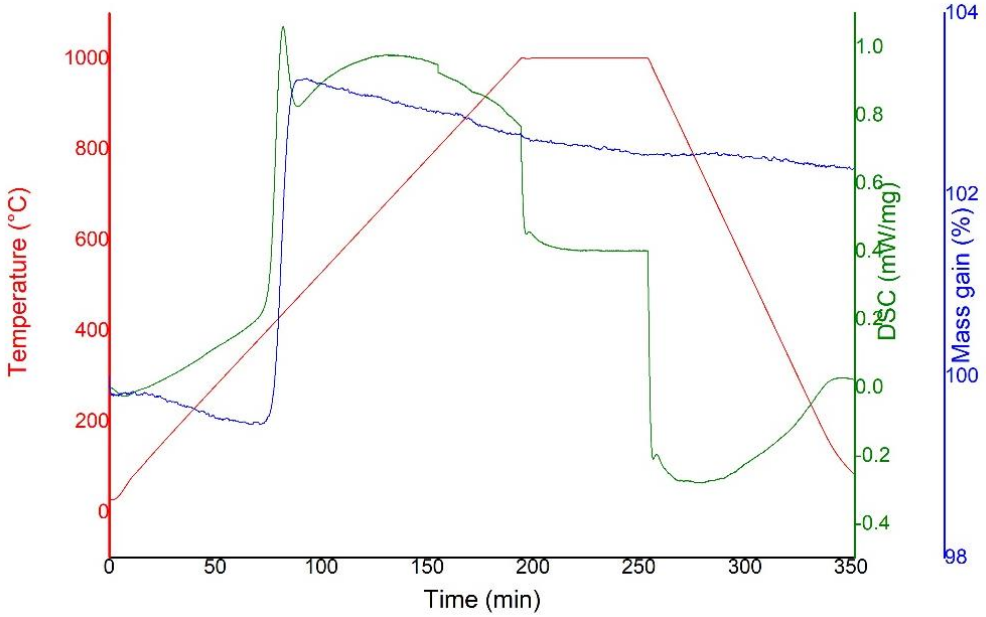

Figure 61: DSC in green, TG in blue and temperature profile in red of the oxidation of UO_2 in air

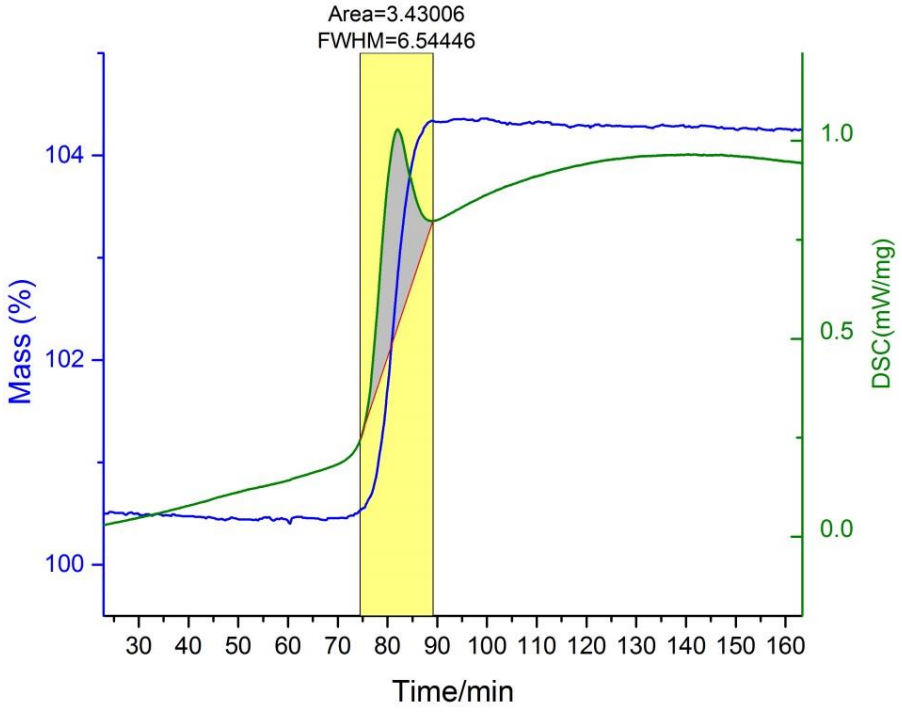

Figure 62: Zoom on the exothermic peak of DSC and TG of the oxidation of UO_2 in air

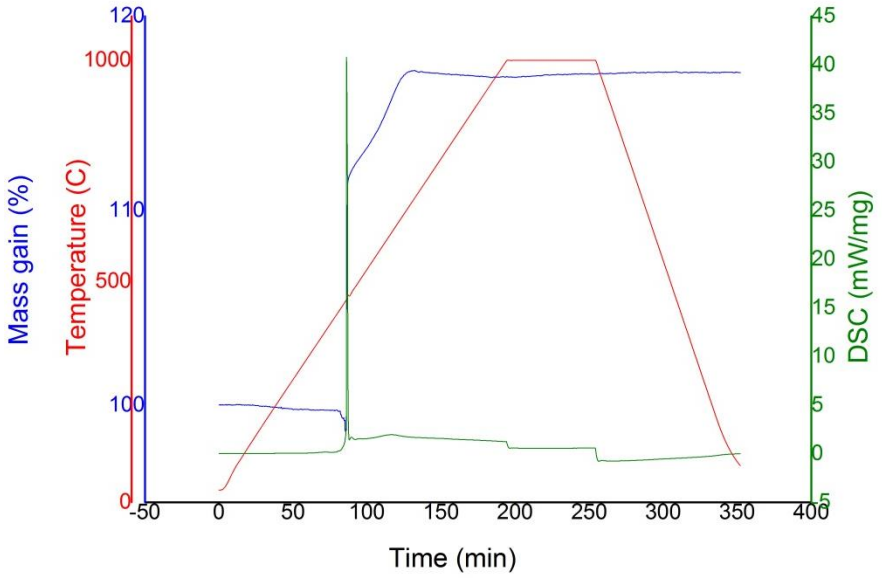

Figure 63: DSC and TG of the oxidation of U_3Si_2 in air

The measured onset temperature of U_3Si_2, 438.5°C, is coherent with literature which reported the stability of U_3Si_2 against atmospheric oxidation and the formation of a protective film when heated in air between 150 and 400°C[55].

The energy released by the UO_2 oxidation (Eq.(9)) was used as a reference to calculate the energy released by the U_3Si_2 oxidation.

$3\ UO_2 + O_2 \rightarrow U_3O_8$ $\quad \Delta H_9$=-320 kJ/mol [63] $\quad$ Eq.(9)

It means that the mass enthalpy expected is -396J/g of UO_2 which corresponds on the DSC graph to 3.43 mW/mg.min. The energy released by U_3Si_2 during oxidation is 32.8 mW/mg.min, which corresponds to a mass enthalpy of -4807J/g of U_3Si_2.

The results are summarized in Table 13.

Table 13: Summary of oxidation results

Compound	Mass gain (%)	Onset Temperature (°C)	Offset Temperature (°C)	Mass enthalpy (J/g)
UO_2	3.9	402	475.5	-396
U_3Si_2	18.6	438.5	720.6	-4807

5.3.2 Identification of the products

Several references have identified U_3O_8 as being the final product of UO_2 and U_3Si_2 oxidation, without being able to detect a silicon oxide phase. Uranium, having a much higher atomic scattering factor than silicon[64], makes it difficult to identify a phase containing silicon by XRD. If it is an amorphous silicon oxide phase, it will not be visible by XRD either.

Several equations are possible for the oxidation of U_3Si_2 in air. As mentioned in section 2.5, Eq.(1) was said to be the most likely to happen. It is also possible that the silicon did not oxidize (Eq. (10)), or that it oxidized to SiO_2 (Eq. (11)). The mass gain is symbolized by m%.

$U_3Si_2 + 5\ O_2 \rightarrow U_3O_8 + 2\ SiO$ $m\%_1=20.8\%$ Eq.(1)

$U_3Si_2 + 4\ O_2 \rightarrow U_3O_8 + 2\ Si$ $m\%_{10}=16.6\%$ Eq.(10)

$U_3Si_2 + 6\ O_2 \rightarrow U_3O_8 + 2\ SiO_2$ $m\%_{11}=25\%$ Eq.(11)

The mass gain measured experimentally, superior to the mass gain of Eq. (10), suggests that the oxidation of silicon did happen.

In an attempt to detect secondary silicon oxide phases, Raman spectrometry was used on the oxidized U_3Si_2 and on the oxidized UO_2 (Figure 64). Raman has the advantage to be sensitive to crystalline structure and to be quantitative.

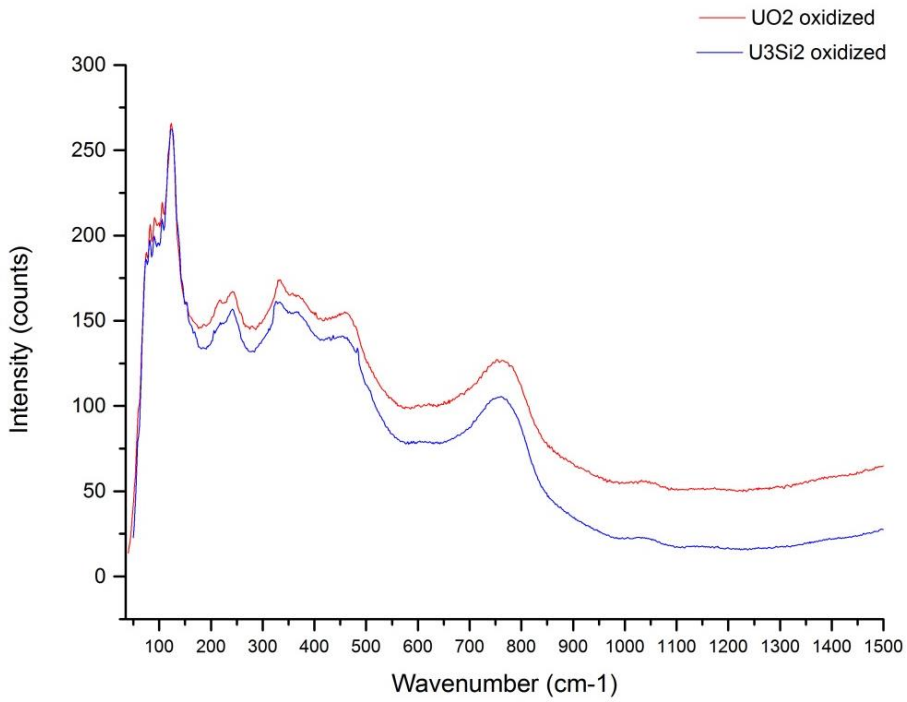

Figure 64: Raman spectrum of UO_2 oxidized in air and of U_3Si_2 oxidized in air

The recorded spectra had already been reported in literature as being the one of U_3O_8[65]. No extra peak, which could come from Si, SiO or SiO_2, was detected. It can be the consequence of low crystallinity of this secondary phase and/or low intensity compared to the intensity of the uranium oxide.

An additional spectrometry technique was also employed as an attempt to identify secondary silicon oxide phases. FTIR is more sensitive to the detection of bonds than to crystalline structure. It was therefore used to detect the presence of Si-O bonds. The results are shown in Figure 65.

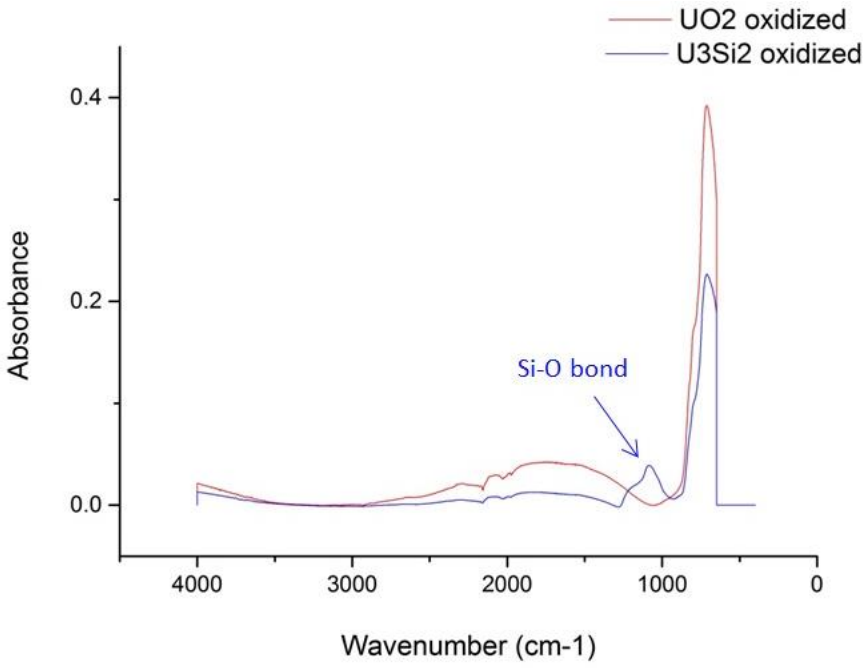

Figure 65: FTIR spectrum of UO_2 and U_3Si_2 oxidized in air

It is possible to notice, on both spectra of Figure 65, the presence of a big peak at 800 cm^{-1}. This peak was reported in literature as coming from U_3O_8[66]. It is in agreement with the obtained data from XRD.

For the oxidized U_3Si_2, it is possible to observe an additional peak at 1085 cm^{-1}. Through search in literature, it was possible to determine that for SiO, a similar peak is present[67]. For vitreous silica and other polymorphs of SiO_2, peaks are expected near 1100 cm^{-1}, 800 cm^{-1} and 480 cm^{-1}. [68,49] The two last peaks are most likely hidden by the absorbance of the U-O bond. Although IR is good at identifying bonds, it is difficult to know for sure the crystalline structure of this silicon oxide. It may as well be SiO or SiO_2. In literature, it has even been reported that SiO is actually a mix of Si and SiO_2[69].

The IR technique applied in the present work proved that the residual is composed of both uranium and silicon oxides, despite being unable to identify the silicon oxide. This result has a significant relevance for understanding the degradation process in oxidative atmosphere. It can be as well useful for geological repository conditions. A simple way to store U_3Si_2 would be to oxidize it to UO_2, a material already well known. In that case, assessing the nature of the silicon oxide phase would be relevant, in order to assess its impact on the leaching of the fuel when in contact with groundwater, for example.

5.3.3 Mass enthalpy of the reaction

The experimental mass enthalpy and the experimental mass gain were analysed to be able to more completely assess the equation of the reaction. Since only 18.6% of the mass was gained, opposed to the 20.8%-21% expected in similar conditions, it was assumed that the oxidation was a combination of two reactions. The first possible combination is a linear combination of Eq.(1) and Eq.(10).

$U_3Si_2 + 5\ O_2 \rightarrow U_3O_8 + 2\ SiO$ $\quad m\%_1=20.8\%$ $\quad \Delta_m H_1$=-5451 J/g of U_3Si_2 [70] $\quad$ Eq.(1)

$U_3Si_2 + 4\ O_2 \rightarrow U_3O_8 + 2\ Si$ $\quad m\%_{10}=16.6\%$ $\quad \Delta_m H_{10}$=-4419 J/g of U_3Si_2 [63] $\quad$ Eq.(10)

To calculate the proportion of each equation, α was defined as the ratio of mass between the mass of U_3Si_2 which would be converted according to Eq.(10) and the initial mass of U_3Si_2. The experimental mass gain $m\%_{exp}$ can therefore be expressed as a function of α and of the two theoretical mass gains of Eq. (10) and (1), $m\%_{10}$ and $m\%_1$, as explained in Eq. (12).

$$m\%_{exp} = \alpha * m\%_{10} + (1 - \alpha) * m\%_1 \qquad \text{Eq. (12)}$$

α was calculated from that equation and it gave α=52%.

In the same way, it is possible to express the mass enthalpy of the oxidation, $\Delta_m H$, as a function of α, $\Delta_m H_1$ and $\Delta_m H_{10}$, the mass enthalpies of reactions (1) and (10), as summarized in Eq. (13).

$$\Delta_m H = \alpha * \Delta_m H_{10} + (1 - \alpha) * \Delta_m H_1 \qquad \text{Eq. (13)}$$

The expected mass enthalpy calculated with the value of α=52% is then $\Delta_m H$=-4915 J/g of U_3Si_2. The experimental value is 2% lower, highly consistent with the expected value. It means that the reaction can be most likely modelled by a linear combination of Eq.(1) and Eq.(10).

α is also equal to the ratio of quantity of matter between the U_3Si_2 which would be converted according to equation (10) and the initial quantity of matter of U_3Si_2. It is then possible to connect it with the quantity of matter of SiO in the system through Eq. (14).

$$1 - \alpha = \frac{n_{SiO}}{2 * n_{U_3Si_2,i}} \qquad \text{Eq. (14)}$$

According to stoichiometry, $2*n_{U3Si2}=n_{Si}+n_{SiO}$, so 1-α represents as well the molar ratio of SiO compared to the total amount of silicon species. The sample is therefore expected to have 48 at.% of SiO for 52 at.% of Si.

The second possible combination is a linear combination of Eq.(10) and Eq. (11). Similar calculations were done for the second possible combination of equations.

$U_3Si_2 + 4\ O_2 \rightarrow U_3O_8 + 2\ Si$ $\quad m\%_{10}$=16.6% $\quad \Delta_m H_{10}$=-4419 J/g of U_3Si_2 [63] $\quad$ Eq.(10)

$U_3Si_2 + 6\ O_2 \rightarrow U_3O_8 + 2\ SiO_2$ $\quad m\%_{11}$=25% $\quad \Delta_m H_{11}$=-6785 J/g of U_3Si_2 [63] $\quad$ Eq.(11)

α was defined here as the ratio between the mass of U_3Si_2 which would be converted according to equation (10) and the initial mass of U_3Si_2. The value obtained was α=76%, meaning there would be 24 at.% of SiO_2 in the system. The mass enthalpy $\Delta_m H$ calculated from α was -4612 J/g of U_3Si_2. The experimental mass enthalpy value is 4% higher than the one calculated here, which is also quite consistent. It means that the reaction may as well be modelled by this second set of equations.

It was not possible to conclusively identify SiO or SiO_2, as the final oxidation product from the preceding experiment, which can be a combination of equations (1)+(10) or (10)+(11). It is however clear that the oxidation of silicon does not get to completion. It leads to think that the oxidation of silicon may be more difficult than that of uranium, that it may require a higher temperature than 1000°C to be fully oxidized until its maximum state of oxidation, Si(IV).

5.3.4 One-step or two-step oxidation?

By looking at the mass gain curve from the U_3Si_2 oxidation (Figure 63), it seems that the oxidation operates in two steps: a first step happening rapidly at 438.5°C with a mass increase of 13.2% and another one that happens more slowly between 438.5°C and 682°C. The mass increase and the heat released by the first and the second step are summarized in Table 14.

Step	Mass increase	Heat (kJ/mol of U_3Si_2)
1st	13.2%	-2915
2nd	5.4%	-785

Table 14: Characteristics of the two observed steps during the oxidation of U_3Si_2

A first possibility would be the two-step oxidation of U_3Si_2 to first UO_2 and then U_3O_8. Westinghouse reports that the oxidation of UO_2 happens in one step but in literature, they clearly show that at 438.5°C, UO_2 is the dominant phase and U_3O_8 is the dominant phase when the oxidation in air is completed.

In the hypothesis that U_3Si_2 would oxidize in a two-step reaction to U_3O_8, the oxidation of U_3Si_2 to UO_2 alone would not explain the first step reported in Table 14, as demonstrated in Eq.(15).

$$U_3Si_2 + 4\ O_2 \rightarrow 3\ UO_2 + 2\ Si \qquad m\%_{15}=12.4\% \qquad \Delta_r H_{15}=-3084\ kJ/mol\ of\ U_3Si_2\ ^{63} \qquad Eq.(15)$$

The heat release of Eq.(15) is close to the one experimentally observed, but the mass increase of Eq. (15) is lower than the one experimentally observed. It suggests that Eq.(15) does not go until completion during the first step. The first step would therefore be a mix of an on-going Eq.(15) with another reaction happening in parallel, contributing to the mass increase and the heat observed. It can be one of the Eq.(9), Eq.(16) or Eq. (17).

$$3\ UO_2 + O_2 \rightarrow U_3O_8 \qquad m\%_9=4.2\% \qquad \Delta_r H_9=-320\ kJ/mol\ of\ U_3Si_2\ ^{63} \qquad Eq.(9)$$

$$2\ Si + O_2 \rightarrow SiO \qquad m\%_{16}=4.2\% \qquad \Delta_r H_{16}=-795\ kJ/mol\ of\ U_3Si_2\ ^{70} \qquad Eq.(16)$$

$$2\ Si + 2\ O_2 \rightarrow 2\ SiO_2 \qquad m\%_{17}=8.3\% \qquad \Delta_r H_{17}=-1822\ kJ/mol\ of\ U_3Si_2\ ^{63} \qquad Eq.(17)$$

Eq.(16) and Eq.(17) are to be chosen between one or the other, depending on if the product is SiO or SiO_2. The mass increase of Eq.(9), Eq.(16) and Eq.(17) was calculated regarding the initial mass of U_3Si_2. For Eq.(9), it reflects the mass increase due to the oxidation of the UO_2 partial fraction in the sample. For Eq.(16) and Eq.(17), it reflects the mass increase due to the oxidation of the silicon partial fraction in the sample.

In case SiO is produced, the other equation happening in parallel during the first step can be Eq.(9), Eq.(16) or both. In case SiO_2 is produced, the other equations would be Eq.(9), Eq.(17) or both.

The two increases seen in Figure 63 can therefore not represent the following pattern: the first increase is the oxidation to UO_2, the second increase is the oxidation to U_3O_8. It is possible that U_3Si_2 first oxidizes to UO_2 and then to U_3O_8, but it cannot be clearly interpreted through the two successive mass gains and the two successive heat releases. If U_3Si_2 would oxidize through a two-step reaction, it would be occurring throughout the two steps observed in Figure 63.

In the hypothesis that U_3Si_2 would oxidize through a single-step oxidation to U_3O_8, the first step could not either represent alone the oxidation of U_3Si_2 to U_3O_8, accordingly to Eq.(10). The mass

increase and the reaction enthalpy are both higher than the ones obtained in the first step reported in Table 14. The oxidation of silicon to either SiO (Eq.(16)) or SiO_2 (Eq.(17)) could not be the second step alone, as both equations have a lower mass increase and a lower reaction enthalpy than the ones obtained for the second step. The first step would therefore be a combination of Eq.(16) or Eq.(17) with Eq.(10), the reactions happening in parallel and reaching the observed completion in the second step.

This section has put in evidence the highly exothermic reaction that the U_3Si_2 oxidation is, compared to the oxidation of UO_2 in similar conditions. This can be of concern in case of accident. It has also been put in evidence U_3O_8 as the final product in the oxidized U_3Si_2 and the existence of a Si-O bound. However, it was not possible here to determine whether it would mean the formation of SiO or SiO_2.

5.4 OXIDATION OF U_3Si_2 IN WATER IN PRESENCE OF H_2O_2

5.4.1 Reactivity in presence of H_2O_2

The powder was put in presence of 0.2mM of hydrogen peroxide and the dissolution was followed by using Arsenazo III while the consumption of hydrogen peroxide was followed by the Ghormley method. The same experiment was repeated several times to have repeatable results.

The dissolution of U(VI) is shown in Figure 66 while the consumption of hydrogen peroxide is shown in Figure 67.

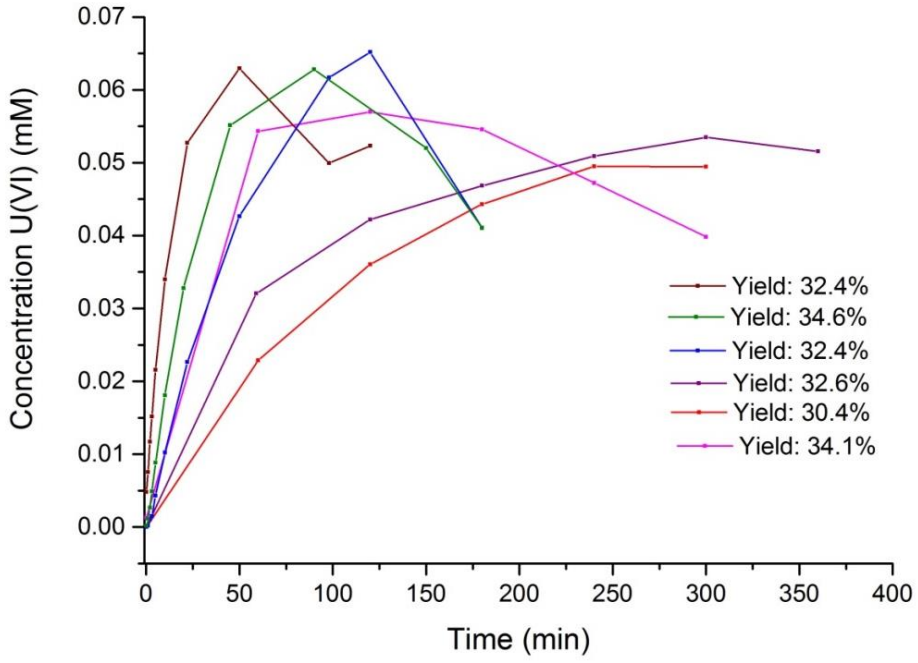

Figure 66: Concentration of U(VI) vs time

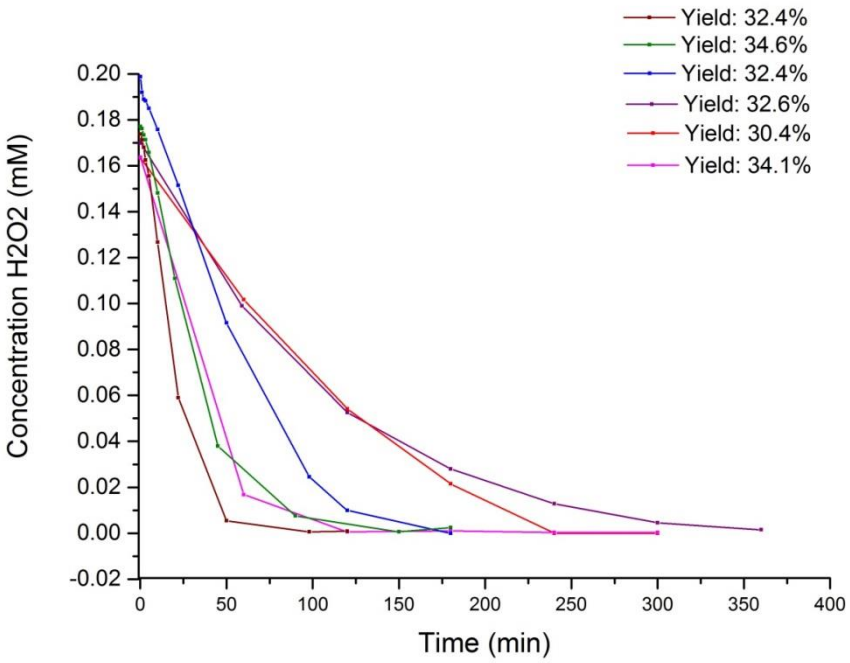

Figure 67: Concentration in H_2O_2 vs time

The yield was calculated as such:

$$\eta = \frac{[U(VI)]_{max} - [U(VI)]_0}{[H_2O_2]_0 - [H_2O_2]_f}$$

$[U(VI)]_0$ and $[H_2O_2]_0$ are the initial concentrations

$[H_2O_2]_f$ is the final concentration in H_2O_2

$[U(VI)]_{max}$ is defined as being the maximum concentration of uranyl, before it decreases.

The uranyl concentration versus time evolved at different speeds for each of the 6 experiments. For 4 out of the 6 experiments, a decrease in uranyl concentration was spotted after the total consumption of hydrogen peroxide. It is a possibility that a parallel reaction of consumption happens with the reaction of dissolution to U(VI), which can be only visible when the dissolution ends. It is also a possibility that the reaction of consumption begins once the hydrogen peroxide is totally consumed. The consumption is visible each time the consumption of hydrogen peroxide happens fast. This phenomenon was further investigated in section 5.4.2.

- Yields

Although very different amounts of time are needed for all the hydrogen peroxide to be consumed, all the yields are quite close to an average of 32.8%, with a standard deviation of 1.4.

Similar experiments carried out on UO_2 powder, with a specific surface area of 5.85m^2/g, gave a yield around 70%[28]. Even though one could expect for UO_2 a yield of 100% (see Eq.(18)), the difference can be explained by the catalytic decomposition of hydrogen peroxide on UO_2 surface.

$$UO_2 + H_2O_2 \rightarrow UO_2^{2+} + 2\ OH^- \qquad \text{Eq.(18)}$$

The Argonne National Laboratory has reported that the catalytic decomposition of hydrogen peroxide happens as well with U_3Si_2. It means that here as well, the yield may be lowered by the

decomposition of hydrogen peroxide. The yield is not sufficient in itself to give the stoichiometry of the reaction.

- Oxidation states

Silicon has a higher electronegativity than uranium on the Pauling scale. It means that in U_3Si_2, silicon has most likely a negative oxidation state. Uranium can have oxidation states from +I to +VI but the minimum oxidation state of silicon is –IV. It means that U_3Si_2 cannot contain entirely neither uranium VI – which means that an oxidation of uranium is indeed happening – nor entirely uranium V, IV or III.

Unlike in UO_2, uranium in U_3Si_2 has two types of positions, each with different chemical environments. However, atoms of silicon always have the same chemical environment. One can therefore assume that silicon in the crystallographic structure has one oxidation state while uranium atoms may be a combination of two different oxidation states, as it is the case for some solids, such as Fe_3O_4.

As can be seen in Figure 68, the grey atoms correspond to one type of position for uranium which represents 1/3 of all the positions occupied by uranium while the red atoms correspond to the second type of positions for uranium, which represents 2/3 of all the positions occupied by uranium. The blue atoms are silicon.

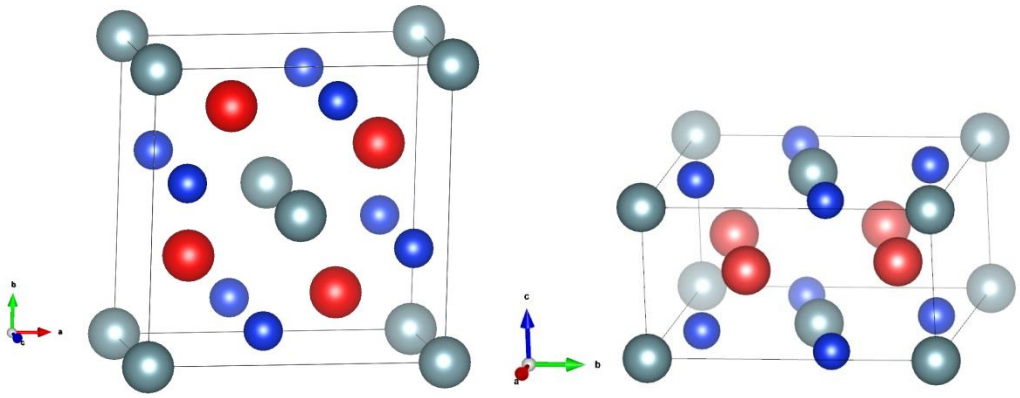

Figure 68: Unit cell containing two U_3Si_2 under two different point of views

Assuming that the crystallographic positions reflect the proportions of the two different oxidation states in uranium, Table 15 lists all the possibilities for the uranium oxidation state, depending on the oxidation state of silicon. An experimental approach to know the oxidation state in the material would be to do XPS.

Table 15: Different possibilities for uranium oxidation state depending on the oxidation state of silicon

Silicon oxidation state	**Oxidation state of type 1 uranium (1/3 of the positions)**	**Oxidation state of type 1 uranium (2/3 of the positions)**
-IV	+VI	+I
-IV	+II	+III
-III	+IV	+I
-II	+I	+II

- ## Products

Since silicon has most likely a negative oxidation state, it is possible that some hydrogen peroxide is consumed to oxidize silicon under a soluble form.

Argonne National laboratory has reported the formation $UO_2(HO_2)_4^{2-}$ and SiO_3^{2-}. It means that the oxidation of uranium went up until U(VI) and silicon up to Si(IV), which are the maximum oxidation states possible. This is explained by the fact that they use highly oxidizing conditions: a 5M concentration in hydrogen peroxide and a reaction conducted in air, conditions different from the experiments conducted here. UO_2^{2+} is complexed with HO_2^- because they use hydrogen peroxide in a strongly basic environment, which strongly encourages the consumption of hydrogen peroxide to the formation of HO_2^-. If the formation of HO_2^- is not taken into consideration, the reaction be re-written as exposed in equation Eq.(19).

$$U_3Si_2 + 13\ H_2O_2 \rightarrow 2\ SiO_3^{2-} + 3UO_2^{2+} + 2OH^- + 12\ H_2O \qquad \text{Eq.(19)}$$

If the catalytic decomposition of hydrogen peroxide is neglected, the equation Eq.(19) leads to a theoretical yield of 23%, which is lower than the one measured here. It most likely means that the species in the medium do not get oxidized until their maximum oxidation state.

It is worth to mention that it is possible that the dissolved uranium measured here is not necessarily uranium VI. For each sampling, a fraction of the reaction media, before under nitrogen gas purging, is put in contact with air, and therefore oxygen, during the measurements. There is a possibility that uranium with a lower oxidation state is produced during the dissolution and then gets oxidized during the measurements. In aqueous solutions, uranium can as well exist with the oxidation states of +III, +IV and +V. Uranium +V, UO_2^+, is unstable and reacts with itself to from uranium +IV and +VI. Uranium +IV is relatively stable but uranium +III easily oxidizes to +IV[71]. Uranium +IV seems to be the other most likely possibility. One would need to perform a similar experiment in a glovebox and analyse the oxidation state of the dissolved uranium.

- ## Morphology of the powder after exposure

For every experiment, the amount of hydrogen peroxide introduced in the reaction media was not enough to completely dissolve the powder. Some powder could be recovered and was analysed with SEM in Figure 69. The morphology of the powder proved to be different before and after the experiment.

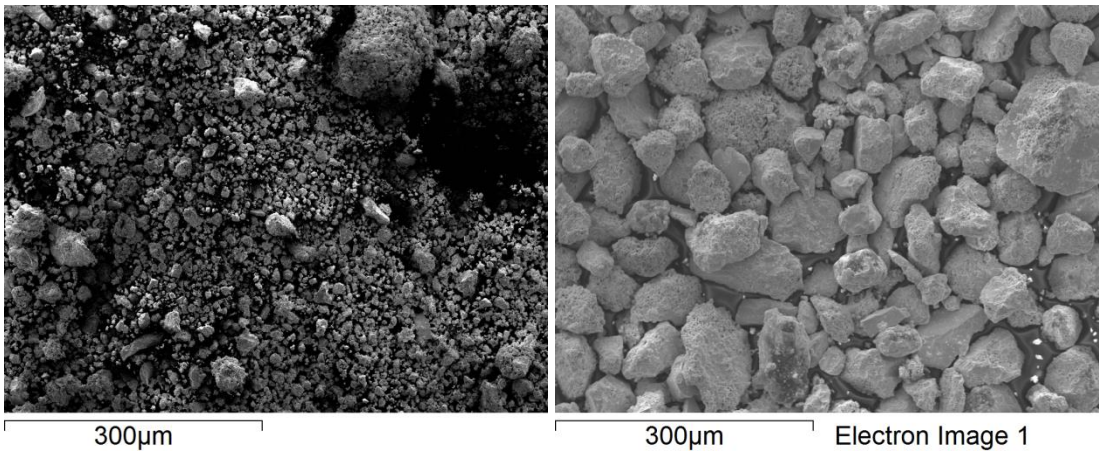

Figure 69: Powder before H_2O_2 (left) and powder after H_2O_2 (right) using SE

After oxidation, the distribution of the particles appears very different for two reasons. First, all the smallest particles visible before the oxidation were most likely consumed entirely by the experiment and only the largest particles are still visible. The second reason is that the powder was dried and some of the particles formed aggregates, as one can see in Figure 70.

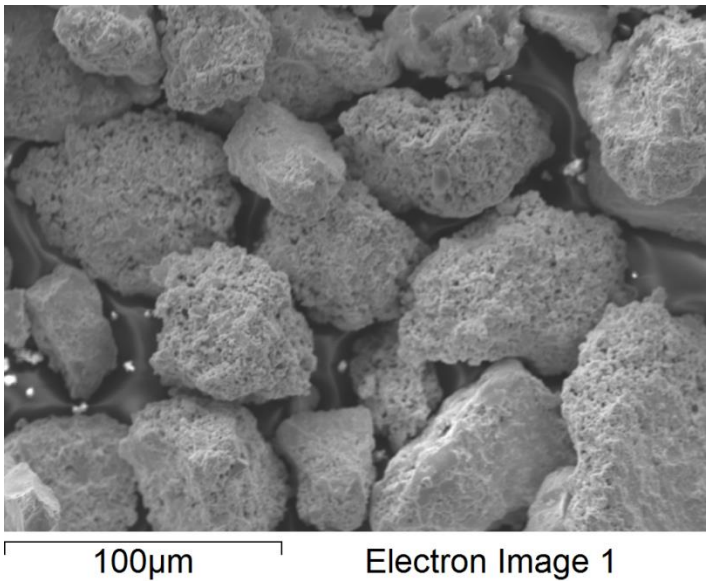

Figure 70: Powder after H_2O_2 using SE

The powder particles also proved to have smoother edges than before. The surface reactions usually start at specific sites of a crystalline structure, taking advantage of a defect, such as a vacancy. Sharp-edged particles are particles that have undergone stress and it is therefore more likely that defects have been formed at the edges, being the most exposed to the chemical oxidation.

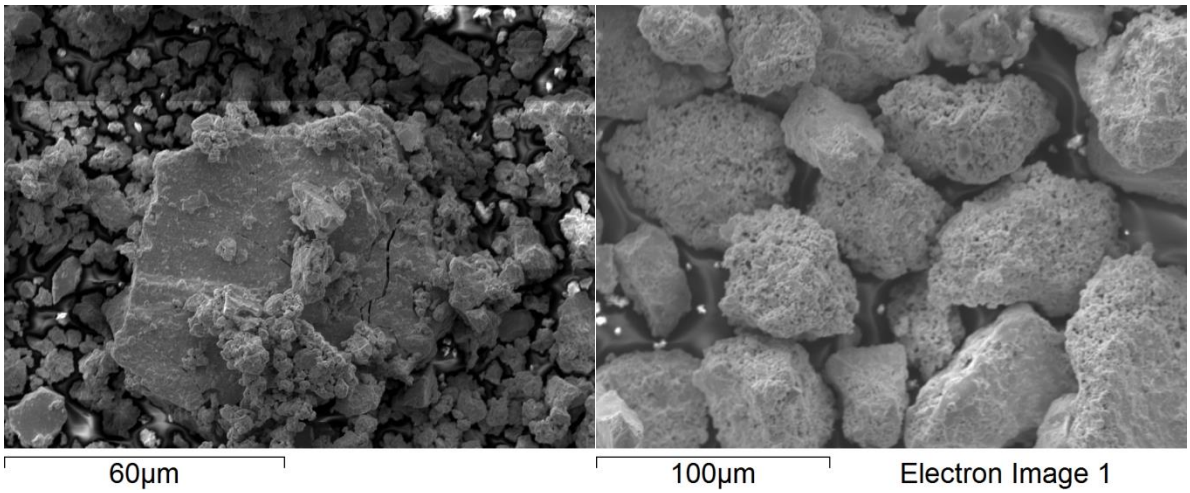

Figure 71: Powder before H_2O_2 (left) and powder after H_2O_2 (right) using SE

A chemical analysis using BSE did not show the formation of a new phase, as reported in Figure 72 and Table 16. The chemical composition appeared the same on all the particles of powder: they contained uranium, silicon and oxygen. The oxygen could mean that an oxide layer has formed on the particles or it could come from the fact that the powder was dried from water.

Table 16: EDS results of the powder after H_2O_2

Element (at.%)	(1)	(2)	(3)
O	27	26	31
Si	31	29	29
U	42	45	40

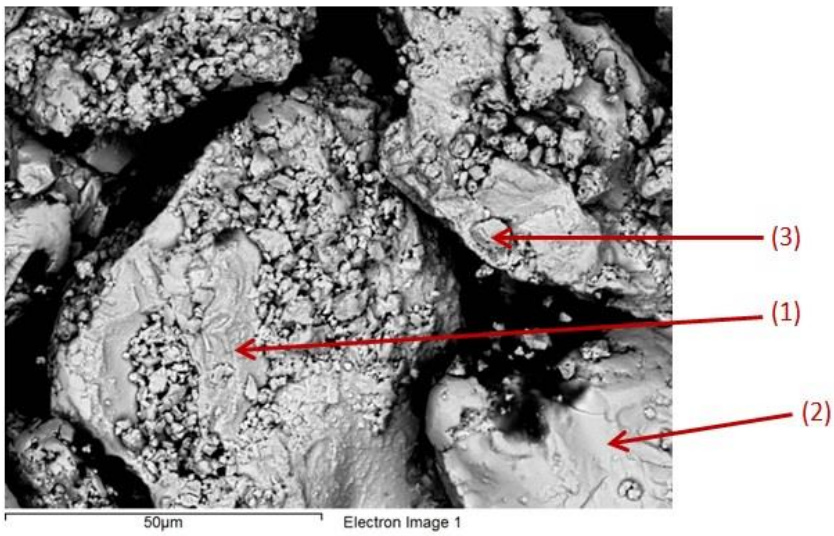

Figure 72: Powder after H_2O_2 using BSE

To further assess the formation of an oxide phase, XRD was conducted on the powder, visible in Figure 73.

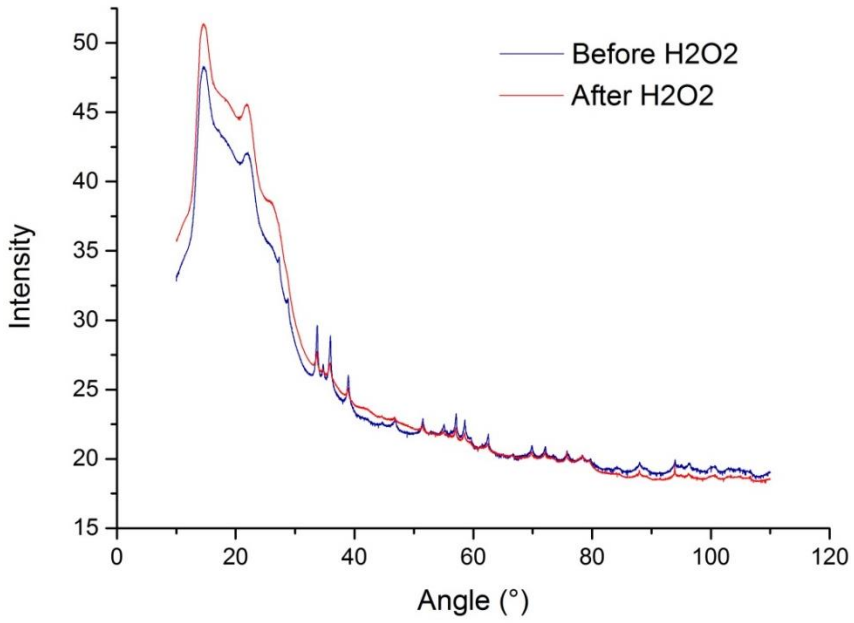

Figure 73: XRD of U_3Si_2 powder before and after H_2O_2

No oxide phase could be determined from the XRD. The bulk of the powder is still U_3Si_2, meaning that the dissolution is a surface reaction. If an oxide layer is formed on the surface, it is under limit detection and/or it is amorphous. The XRD and BSE images results suggest that silicon gets removed as well.

- Kinetics

The equation Eq.(20) describes the rate consumption of hydrogen peroxide by the powder[72]. In this equation, SA represents the surface area of the powder, V the volume, and $[H_2O_2]$ the concentration of H_2O_2.

$$-\frac{d[H_2O_2]}{dt} = k(\frac{SA}{V})[H_2O_2] \qquad \text{Eq.(20)}$$

If the assumption is made that the product $k(\frac{SA}{V})$ remains constant over time, the equation Eq.(20) can be re-written with k'= $k(\frac{SA}{V})$. The equation then becomes a first order differential equation with one variable and the solution can be written in Eq.(21) where $[H_2O_2]_0$ is the initial concentration, 0.2mM.

$$\ln\left(\frac{[H_2O_2]}{[H_2O_2]_0}\right) = -k't \qquad \text{Eq.(21)}$$

For each of the six experiments, $\ln\left(\frac{[H_2O_2]}{[H_2O_2]_0}\right)$ was plotted against time and modelled as a linear curve, using the uranyl concentration values before it starts to decrease. The results are presented in Table 17.

Table 17: Results from the linear regression

Reaction number	Yield (%)	k' (s^{-1})	R^2	Number of points plotted
1	32.6	2.17×10^{-4}	0.992	7
2	30.4	2.00×10^{-4}	0.988	4
3	34.1	7.83×10^{-4}	0.993	3
4	32.4	1.03×10^{-3}	0.991	9
5	32.4	3.83×10^{-4}	0.978	10
6	34.6	6.33×10^{-4}	0.998	10

The R^2 is close to 0.99 for almost every experiment, meaning that k' is constant, confirming that the product $k(\frac{SA}{V})$ is constant during a given experiment. However, k' changes a lot from one experiment to another, multiplied by a factor of five for the two most extreme values. For reaction 2 and 3, the liability of the results can be questioned since the modelling was done with a few points only.

Since the yields are similar for all those experiments, the difference in kinetics between the six experiments most likely comes from a difference in reactivity of the surface area, rather than from an inhomogeneity in composition of the powder.

The differences observed for k' can be explained by two factors.

First, it can be explained by the broad particle distribution of the powder, as shown in section 5.1.2. Since a very low quantity of powder is used each time (50mg), it is possible that the distribution of the particles changes significantly from an experiment to another. The specific surface area being changed, the total surface area exposed to oxidation (SA) can increase with a constant mass.

Second, it was shown for UO_2 powder that k would increase with the decrease of particle size[73]. The smaller the particles are, the higher k is. It means that, for a sample of 50mg where the particles size is in average lower, both the surface area and k are higher, meaning that their product, $k(\frac{SA}{V})$, is higher as well.

Both contributions, SA and k, could explain that from an experiment to another, a factor of five is observed for $k(\frac{SA}{V})$, even if the same mass was used.

One can note that the volume of the reaction media decreases over one experiment, since 1 to 2mL is removed for each measurement. Since $k(\frac{SA}{V})$ is constant over one experiment, it means that (k*SA) decreases over one experiment.

5.4.2 Consumption of uranyl

This experiment was realized to understand the consumption of uranyl observed in the hydrogen peroxide experiments, presented in section 5.4.1. This consumption has not been observed for UO_2 powder.

In this experiment, the powder was put in the same conditions as for the hydrogen peroxide experiments (section 5.4.1), except that instead of adding hydrogen peroxide, uranyl was added to reach 0.06mM, the maximum concentration observed in the experiments of section 5.4.1. The experiment was repeated three times.

The powder showed uranyl consumption for one of the three experiments, as shown in Figure 74. This difference can be explained by the fact that the powders used for the three experiments were stored in different gloveboxes: one with an oxygen level inferior to 0.1ppm (red curve) and another one with an oxygen level of 500ppm (blue and green curves). It is therefore possible that the powder stored in the glovebox with the higher oxygen level could have passivated, creating a thin layer of oxide. Since the reactions studied here are surface reactions, this passivation layer can totally change the reactivity of the powder. For reactions realized in sections 5.4.1 and 5.4.3, the powder used was the one stored in the glovebox with an oxygen level inferior to 0.1ppm.

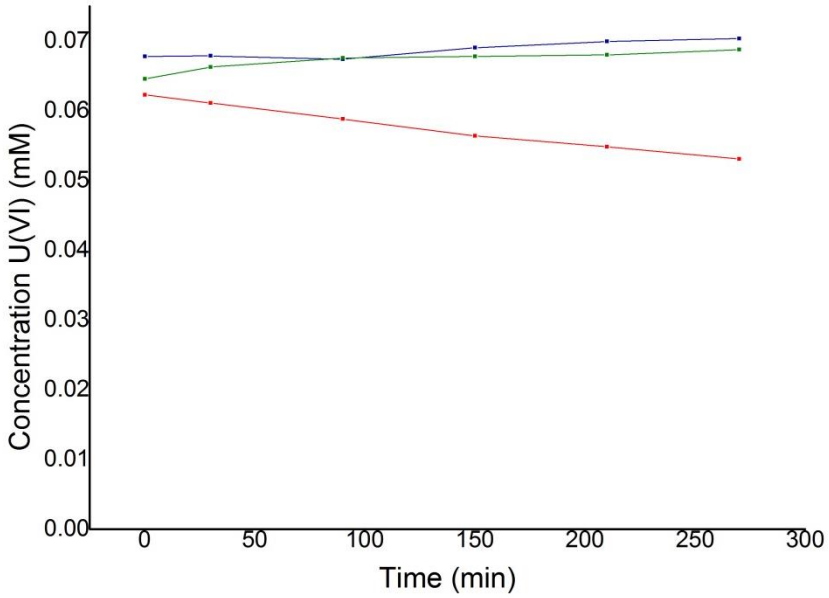

Figure 74: U(VI) concentration in presence of 0.06mM of uranyl

The red curve indicates that an interaction between U_3Si_2 and the dissolved uranium indeed exists. Nevertheless, the consumption of uranyl observed here is slower than the one observed in section 5.4.1. It leads to the hypothesis that during the reaction in presence of hydrogen peroxide, a catalyst or some products may be involved in the acceleration of the consumption.

5.4.3 Dissolution under irradiation

To get closer to real conditions, the powder was exposed to a gamma source. The hydrogen peroxide was therefore generated *in situ*.

- Reference curve

A first experiment without the powder was realised to monitor the hydrogen peroxide production. The result is shown in Figure 75.

The concentration of hydrogen peroxide generated increases until converging to a constant value. The values obtained could be modelled by an asymptotic fit with a very good R^2, shown in Figure 75.

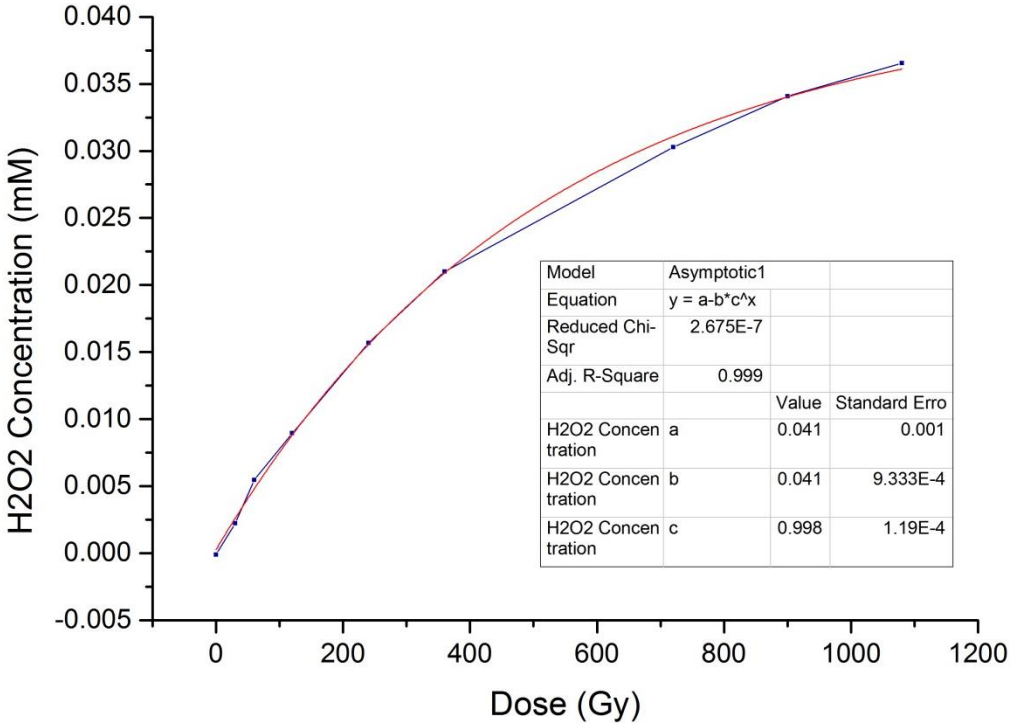

Figure 75: H_2O_2 concentration vs absorbed dose: experimental values in blue and in red the asymptotic fit

The asymptotic function increases until converging to a limit concentration of 0.041mM.

- ### Irradiation with U_3Si_2 powder

The powder was submitted to irradiation and the hydrogen consumption, as well as the uranyl dissolution, were recorded (Figure 76 and Figure 77). The experiment was repeated twice (pink and blue curve), the second time for a longer time (pink curve). Thanks to the reference curve established in Figure 75, it was possible to highlight the hydrogen peroxide consumption.

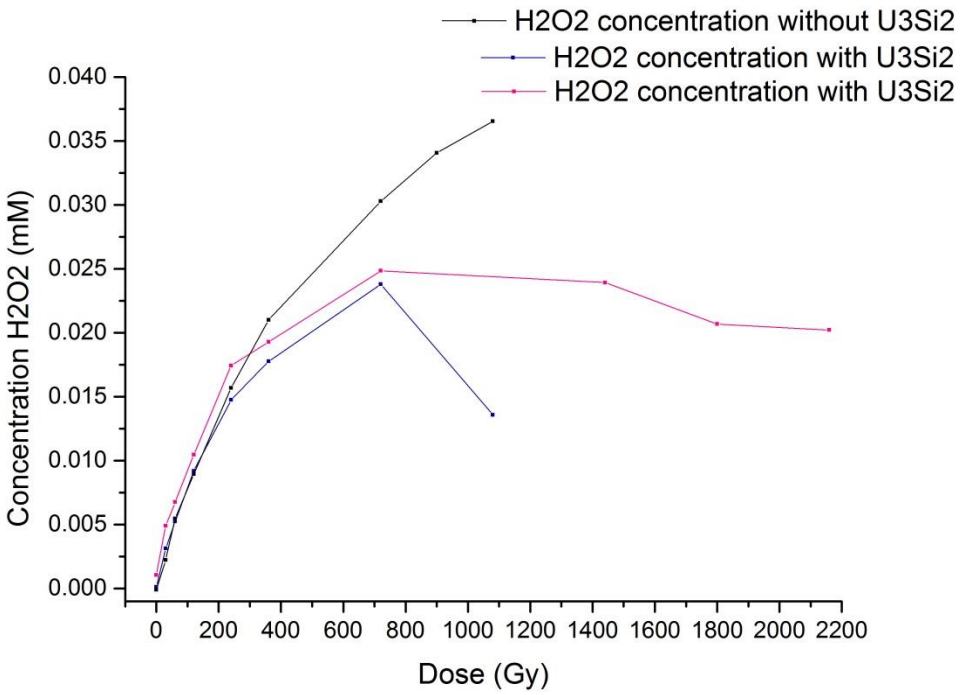

Figure 76: Hydrogen peroxide concentration in presence and in absence of U_3Si_2 as a function of the absorbed dose

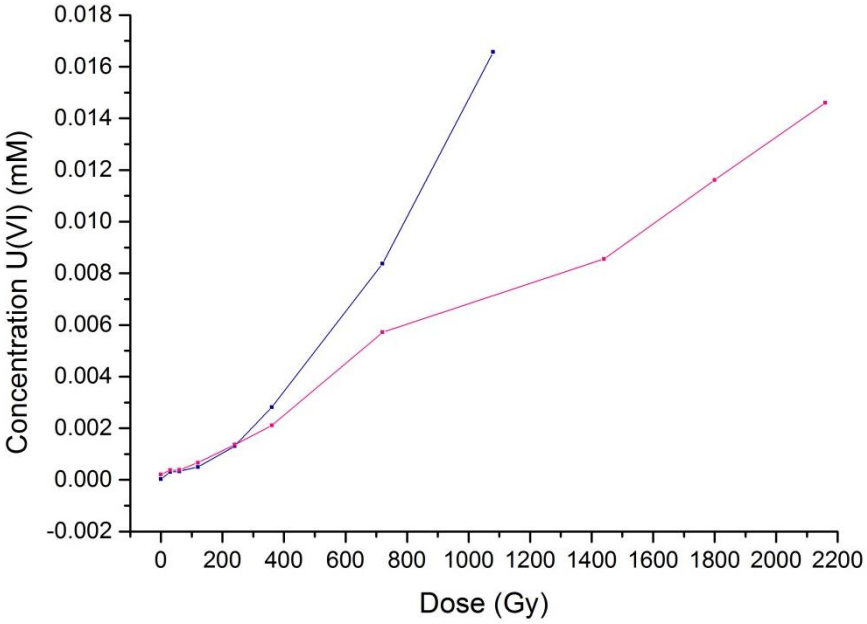

Figure 77: U(VI) concentration as a function of absorbed dose

The measured concentration of U(VI) is lower than the ones from the experiments in section 5.4.1, where the maximum concentration achieved was 0.06mM. The difference in concentrations between the pink and blue curves observed from 720Gy to 1400Gy in Figure 77 can be explained by the incertitude of the value due to the equipment and manipulation, and/or by the difference in reactivity of the powder due to the particles size, as mentioned before.

As for the hydrogen consumption, the sudden decrease observed for the blue curve in Figure 76 seems to be an artefact since it was not confirmed by repeating the experiment (pink curve). However, the pink curve denotes after 800Gy either stagnation or a consumption of hydrogen peroxide slightly faster than the production.

At 2200Gy, the yield for the pink curve was calculated as being the ratio between the concentration of U(VI) and the concentration of hydrogen peroxide consumed, calculated as the difference between the hydrogen peroxide at 2200Gy without powder (calculated using the asymptotic fit) and the concentration measured with powder. It gave 60%, a much higher value than the one registered before. Two explanations are possible and both rely on the fact that the concentration in hydrogen peroxide is here much lower than the one used for the experiments in section 5.4.1. It is first possible that the catalytic decomposition of hydrogen peroxide happens in a lower amount here, since the decomposition increases with concentration. It is also possible that since less hydrogen peroxide is accessible, that the products have lower oxidation states than the ones from the hydrogen peroxide experiments.

The dissolution behaviour of U_3Si_2 in presence of hydrogen peroxide still requires investigation. The yield is higher than for UO_2, meaning that more hydrogen peroxide than for UO_2 is needed for the dissolution of U_3Si_2, but the identification of the dissolved species is still necessary. The broad particle distribution makes it harder to have an idea of the dissolution rate, as it changes from an experiment to another. An unexpected consumption of dissolved uranium was put in evidence and seems to be accelerated after total consumption of hydrogen peroxide, as in section 5.4.1. Work is still required to understand the products and the reactants of this uranyl consumption.

CONCLUSIONS

Fabricating the alloys by arc melting, milling them and sintering the powder by Spark Plasma Sintering has proven to be an efficient way of producing pellets suitable for LWR applications. This methodology requires low sintering temperature and low sintering times, without the use of any additives which create open pores. The produced pellets proved to be dense (>96%TD) and to have an advantageous microstructure with nano-metric closed pores, which are an asset for the retention of fission products.

Using a similar sintering methodology for studying the interaction of U_3Si_2 with one of the most abundant fission products, molybdenum, showed the different stages of this solid-solid interaction. While molybdenum proved to have no solubility in the matrix, the formation of two ternary phases could be put in evidence: $U_2Mo_3Si_4$, resulting from the solid-solid interaction of pure molybdenum with U_3Si_2, and $U_4Mo(MoxSi_{1-x})Si_2$, resulting from the interaction of $U_2Mo_3Si_4$ with U_3Si_2. The formation of γ(U, Mo), produced to balance the overall system, was connected to the formation of the ternary phases. The results obtained here proved to be different from those recorded in literature, where a melting process was used. In literature, much more phases were recorded than here, showing that liquid-liquid interactions cannot be used to predict solid-solid interactions.

The oxidation of U_3Si_2 in air showed the formation of an oxide of silicon, whose existence had been not demonstrated before. The oxidation of U_3Si_2 happens through a much more exothermic reaction than the oxidation of UO_2. The heat released could be troublesome in case of accident and accelerate the melting of the core, for example.

As for the oxidation of U_3Si_2 in presence of hydrogen peroxide, the identification of the products remains an important part to be able to understand the dissolution of U_3Si_2. Due to the heterogeneous distribution of the powder, it was hard to get to the dissolution rate. However, the yields calculated for each experiment had a low standard deviation, showing the homogeneity in composition of the powder. It is as well lower than the yield of UO_2 for similar experiments, meaning that more hydrogen peroxide is required to dissolve the material. It is most likely due to the fact that both uranium and silicon get oxidized and dissolved, but their oxidation states, both in the material and in solution, need to be determined. An unexpected consumption of dissolved uranium was put in evidence, which still needs to be further investigated.

A possible improvement to the methodology of the experiments in presence of hydrogen peroxide could be to hand-mill U_3Si_2 and then sieve it, to be able to control the particles size. Once the surface area is known, it would be possible to know the dissolution rate for this specific surface area. It is also possible to realize XPS on U_3Si_2 to understand the oxidation states in the material and to follow the dissolution in presence of hydrogen peroxide by using ICP-OES, for a better understanding of the dissolved species.

U_3Si_2 is still a fuel under investigation, to understand whether it fulfils the criteria of an accident tolerant fuel. Despite some advantages, such as its high thermal conductivity or its high uranium-loading that could be economically beneficial, it presents some drawbacks, such as an exothermic oxidation. The question of the handling of the back-end is also a decisive problematic, that will help decide whether this fuel can be used in a LWR.

REFERENCES

[1] Institut de Radioprotection et de Sûreté nucléaire, *L'Analyse de l'IRSN du déroulement de l'accident de Fukushima* (2013)

[2] J. Bischoff, P. Blanpain, J-C. Brachet, C. Lorrette, A. Ambard, J. Strumpell, K. McKoy, *Development of Fuels with enhanced accident tolerance*, Accident Tolerant Fuel Concepts for Light Water Reactors, IAEA Tecdoc 1797, (2014) 22-29.

[3] Westinghouse Electric Company, *Development of LWR Fuels with Enhanced Accident Tolerance*, Final Technical Report (2015).

[4] Argonne National Laboratory, RERTR Department, http://www.rertr.anl.gov/ (2013).

[5] R.F. Domagala, T.C. Wiencek, H.R. Thresh, *U-Si and U-Si-Ai Dispersion Fuel Alloy Development for Research and Test* Reactors, American Nuclear Society, 62, 3, (1983) 353-360.

[6] R. Nave, *Abundances of the Elements in the Earth's Crust*, Georgia State University.

[7] S.C. Middleburgh, R.W. Grimes, E.J. Lahoda, C.R. Stanek, D.A. Andersson, *Non-stoichiometry in U_3Si_2*, J. of Nucl. Mat., 482, (2016) 300-305.

[8] J. M. Harp, P. A. Lessing, R. E. Hoggan, *Uranium silicide pellet fabrication by powder metallurgy for accident tolerant fuel evaluation and irradiation*, J. of Nucl. Mat., 466 (2015) 728-738.

[9] Westinghouse Electric Company, *Development of LWR Fuels with Enhanced Accident Tolerance*, Final Technical Report (2015), 34-36.

[10] K. D. Kok, *Nuclear Engineering Handbook*, Second Edition (2016), 357-358.

[11] D. G. Cacuci, *Hanbook of Nuclear Engineering, Vol.1: Nuclear Engineering Fundamentals*, (2010), 1523-1524.

[12] V. V. Rondinella, T. Wiss, *The High burn-up structure in nuclear fuel*, Materials Tody, 13, 12 (2010) 24-32.

[13] K. Kapoor, A. Ahmad, A. Laksminarayana, G.V.S. H. Rao, *Fracture properties of sinteres UO2 ceramic pellets with duplex microstructure*, J. of Nucl. Mat., 366, 1-2 (2007) 87-98.

[14] L. O. Jernkvist, A. Massih, *Analysis of the effect of UO2 high burnup microstructure on fission gas release*, IAEA online database, 2002.

[15] A.T. Nelson, J.T. White, D.D. Byler, J.T. Dunwoody, J.A. Valdez, K.J. McClellan, *Overview of properties and performance of uranium-silicide compounds for Light Water Reactor Applications*, Transactions of the American Nuclear Society, Vol. 110, Reno, Nevada, June 15-19, 2014.

[16] P. Rogl, T. Le Bihan, H. Noël, *Phase equilibria and magnetism in the Mo-Si-U system*, J. of Nucl. Mat., 288, (2001) 66-75.

[17] M. Ugajin, A. Itoh, S. Okayasu, Y. Kazumata, *Uranium molybdenum silicide U3MoSi2 and phase equilibria in the U-Mo-Si system, J*. of Nucl. Mater. 257 (1998) 145-151.

[18] E. S. Wood, J.T. White, A.T. Nelson, *Oxidation behavior of U-Si compounds in air from 25 to 1000°C*, J. of Nucl. Mat. 484 (2007) 245-257.

[19] K. Johnson, V. Ström, J. Wallenius, D. Adorno, *Oxidation of accident tolerant fuel candidates*, J. of Nucl. Science and Technology, 54, 3 (2017) 280-286.

[20] D. Swiatla-Wojcik, *Hybrid method for numerical modelling of LWR coolant chemistry,* Radiation Physics and Chemistry 127 (2016) 236-242.

[21] Personal archives from a lecture of M. Jansson, Dpt of Nuclear Chemistry, KTH, during the course Nuclear Fuel Cycle KD2430.

[22] A. B. Fidalgo, M. Jonsson, *Can H_2 enhance the oxidative dissolution of UO_2?*, J. of Nucl. Mat. 477 (2016) 85-87.

[23] W. Loveland, *Nuclear Reactor Chemistry*, Oregon State University, 2015.

[24] K. Kanjana, K. S. Haygarth, W. Wu, D. M. Bartels, *Laboratory studies in search of the critical hydrogen concentration,* Radiation Physics and Chemistry 82 (2013) 25-34.

[25] J. Andersson, T. Jalonen, *Challenges in Developping the Basic Design of the KBS-3 System into a Qualified and Industrially Viable Operation*, Powerpoint presentation at the International Conference on the Management of Spent Fuel from Nuclear Power Reactors at IAEA HQ, SKB, 2015.

[26] B. A. Buchholz, G. F. Vandegrift, *Processing of LEU targets for ^{99}Mo production: dissolution of U_3Si_2 targets by alkaline hydrogen peroxide*, Argonne National Laboratory, 1994.
[27] L. Chen, D. Dong, B. A. Buchholz and G.F. Vandegrift, *Progress in alkaline peroxide dissolution of low-enriched uranium metal and silicide targets*, Argonne National Laboratory, 1996.
[28] M. Jonsson, E. Ekeroth, O. Roth, *Dissolution of UO_2 by one- and two-electron oxidants*, Mat. Res. Soc. Symp. Proc. 807 (2004) 77-82.
[29] F. Clarens, J. de Pablo, I. Casas, J. Giménez, M. Rovira, J. Merino, E. Cera, J. Bruno, J. Quinones, A. Martinez-Esparza, *The oxidative dissolution of unirradiated UO2 by hydrogen peroxide as a function of pH*, J. of Nucl. Mat. 345, 2-3 (2005) 225-231.
[30] E. Ekeroth, O. Roth, M. Jonsson, *The relative impact of radiolysis products in radiation induced oxidative dissolution of UO_2*, J. of Nucl. Mat. 355 (2006) 38-46.
[31] A. Barreiro Fidalgo, *Experimental studies of radiation-induced dissolution of UO2*, Doctoral Thesis in Chemistry, KTH, 2017.
[32] K. Johnson, *High Performance Fuels for Water-Cooled Reactor Systems*, Doctoral Thesis in Physics, KTH (2016), 45-51.
[33] J. Haidar, A. J. D. Farmer, *Surface temperature measurements for tungsten-based cathodes of high-current free-burning arcs*, J. Phys. D: Appl. Phys., 28 (1995) 2089-2094.
[34] Z. Zhang, Z. Liu, J. Lu, X. Shen, F. Wang, Y. Wang, *The sintering mechanism in spark plasma sintering – proof of the occurrence of spark discharge*, Scripta Materialia, 81 (2014) 56-59.
[35] Cema Technologies, *Le principe Spark Plasma Sintering*, cema-technologies.fr.
[36] N. Saheb, Z. Iqbal, A. Khalil, A.S. Hakeem, N. Al Aqeeli, T. Laoui, A. Al-Qutub, R. Kirchner, *Spark Plasma Sintering of Metals and Metal Matrix Nanocomposites: A Review*, J. of Nanomaterials (2012) 1-13.
[37] Z. A. Munir, U. Anselmi-Tamburini, M. Ohyanagi, *The effect of electric field and pressure on the synthesis and consolidation of materials: A review of the spark plasma sintering method*, J. Mater. Sci., 41 (2006) 763-777.
[38] J.A. Ghormley, A.C. Stewart,*Effects of gamma-Radiation on Ice*, J. Am. Chem. Soc. 78 (1956) 2934-2939.
[39] S. B. Savvin, *Analytical use of Arsenazo III,* Talanta 8 (1961) 673-685.
[40] The Editors of Encyclopaedia Britannica, *Archimedes' principle*, Encyclopaedia Britannica.
[41]Susan Swapp (University of Wyoming), *Scanning Electron Microscopy (SEM)*, Carlton College (2017).
[42] K. Maehata, K. Idemitsu, K. Tanaka, *X-ray energy dispersive spectroscopy of uranium ore using a TES microcalorimeter mounted on a field-emission scanning electron microscope*, Nuclear Instruments and Methods in Physics Research A 648 (2011) 285-289.
[43] K. D. Vernon-Parry, *Scanning Electron Microscopy: an introduction*, III-Vs Review, 13, 4 (2000) 40-44.
[44] J. Goodge (University of Minnesota at Duluth), *Back-scattered Electron Detector (BSE)*, Carlton College (2016).
[45] Materials Evaluation and Engineering, Inc*, EDS Description of a technique*.
[46] Central Facility for Advanced Microscopy and Microanalysis*, Introduction to Energy Dispersive X-ray Spectrometry (EDS)*, University of California, Riverside.
[47] G. F. Vander Voort, *Metallography, Principles and Practice*, ASM International, 1999.
[48] R. Nave, *Bragg's Law*, Department of Physics and Astronomy George State University (2000).
[49]R. Hanna, *Infrared Absorption Spectrum of Silicon Dioxide,* J. of the American Ceramic Society, 48 (1965) 11, 595-599.
[50] Northern Illinois University, *Introduction to Fourier Transform Infrared Spectrometry*, (2001).
[51] P. Atkins, J. De Paula, *Elements of Physical Chemistry*, 2009, p.458-460.
[52] K. Scott, *Raman spectroscopy,* University of Saint-Andrews
[53] AZoM, *Oxygen Analysis – Determination of Oxygen Content by Inert Gas Fusion by LSM Analytical Services*, AZO Materials (2008).

[54] G. L. Hofman, *A short note on high density dispersion fuel*, RERTR Argonne National Laboratory (1996).
[55] W. D. Wilkinson, *Uranium metallurgy*, Interscience Publishers, Vol. 2 (1962) 1109-1120.
[56] P. Villars, *U_3Si_2 Crystal Structure*, Pauling file in: Inorganic Solid Phases, SpringerMaterials (online database), Springer, Heidelberg (2016).
[57] Portland State University, *X-ray Diffraction (XRD)*, Powerpoint presentation (2004).
[58] P. K. Lu, W. Li, J. J. Lannutti, *Density gradients and the expansion–shrinkage transition during sintering*, Acta Materialia 52 (2004) 2057-2066.
[59] T. Sata, *Expansion during sinering of NaCl powders*, Ceramics International 20 (1994) 39-47.
[60] Data provided by Simon Middleburgh, working at Westinghouse, Sweden.
[61] G. L. Hofman and M. K. Meyer, *Design of high density gamma-phase uranium alloys for LEU dispersion fuel applications*, Argonne National Laboratory, 1998.
[62] D. Adorno Lopes, T. Augusto Guisard Restivo, A. Fernando Padilha, *Mechanical and thermal behaviour of U-Mo and U-Nb-Zr alloys*, J. of Nucl. Mat. 440 (2013) 304-309.
[63] O. Kubaschewski, C. Alcock, P. Spencer, Materials Thermochemistry, 6th ed., Oxford, Pergamom Press, 1993.
[64] B.L. Henke, E.M. Gullikson, and J.C. Davis. *X-ray interactions: photoabsorption, scattering, transmission, and reflection at E=50-30000 eV, Z=1-92*, Atomic Data and Nuclear Data Tables Vol. 54 (no.2), 181-342 (July 1993).
[65] G.C. Allen, I. S. Butler, N. Anh Tuan, *Characterization of uranium oxides by micro-raman spectroscopy*, J. of Nucl. Mat. 144 (1987) 17-19.
[66] L. A. Silva, F. S. Lameiras, A.M. Matildes dos Santos, W. B. Ferraz, *Determination of U_3O_8 in UO_2 by infrared spectroscopy,* Int. Eng. J., Ouro Preto, 70(1) (2017) 59-62.
[67] S. Wetzel, M. Klevenz, H.-P. Gail, A. Pucci, M. Trieloff, *Laboratory measurement of optical constants of solid SiO and application to circumstellar dust*, A&A 553, A92 (2013) 1-13.
[68] E. R. Lippincott, A. Van Valkenburg, C. E. Weir, E. N. Bunting, *Infrared Studies on polymorphs of silicon dioxide and Germanium dioxide*, J. of Research of the National Bureau of Standards, 61, 1 (1958) 61-70.
[69] K. Schulmeister, W. Mader, *TEM investigation on the structure of amorphous silicon monoxide*, J. of Non-Crystalline Solids 320 (2003) 143-150.
[70] A. Jain*, S.P. Ong*, G. Hautier, W. Chen, W.D. Richards, S. Dacek, S. Cholia, D. Gunter, D. Skinner, G. Ceder, K.A. Persson (*=equal contributions), The Materials Project: A materials genome approach to accelerating materials innovation APL Materials, 2013, 1(1), 011002. doi:10.1063/1.4812323
[71] Dr. D. Hobart, *Uranium: Properties*, Los Alamos National Laboratory, 2013.
[72] O. Roth, *Redox Chemistry in Radiation Induced Dissolution of Spent Nuclear Fuel – from elementary reactions to predictive modelling*, Doctoral Thesis in Chemistry, KTH, 2008.
[73] O. Roth, T. Bönnemark, M. Jonsson, *The influence of particle size on the kinetics of UO2 oxidation in aqueous powder suspensions*, J. of Nucl. Mat. 353 (2006) 75-79.